SPECKLE PATTERN INTERFEROMETRY: VIBRATION MEASUREMENT BASED ON A NOVEL CMOS CAMERA

Daniele Santonocito

Submitted for the degree of Master of Philosofy

Heriot-Watt University

School of Engineering and Physical Sciences

June 2013

Abstract

A digital speckle pattern interferometer based on a novel custom complementary metal-oxide-semiconductor (CMOS) array detector is described. The temporal evolution of the dynamic deformation of a test object is measured using inter-frame phase stepping. The flexibility of the CMOS detector is used to identify regions of interest with full-field time averaged measurements and then to interrogate those regions with time-resolved measurements sampled at up to 7 kHz.

The maximum surface velocity that can be measured and the number of measurement points are limited by the frame rate and the data transfer rate of the detector. The custom sensor used in this work is a modulated light camera (MLC), whose pixel design is still based on the standard four transistor active pixel sensor (APS), but each pixel has four large independently shuttered capacitors that drastically boost the well capacity from that of the diode alone. Each capacitor represents a channel which has its own shutter switch and can either be operated independently or in tandem with others. The particular APS of this camera enables a novel approach in how the data are acquired and then processed.

In this Thesis we demonstrate how, at a given frame rate and at a given number of measurement points, the data transfer rate of our system is increased if compared to the data transfer rate of a system using a standard approach. Moreover, under some assumptions, the gain in system bandwidth doesn’t entail any reduction in the maximum surface velocity that can be reliably measured with inter-frame phase stepping.

Table of contents

Chapter One

Introduction

1.1 Background to the project

Established vibration measurement techniques based on conventional sensors require instrumentation using contacting transducers, with concomitantly long measurement times, poor spatial resolution and perturbation of the structure under investigation by the transducer loading. Optical techniques for noncontact measurements had been developed during the last thirty years; in particular, full field methods such as holography, speckle interferometry and coherent fringe projection cover an extended sensitivity domain and permit the measurement of shape, deformation, vibration modes or the detection of faults on almost every type of structure or material. The capability to work with materials having a surface roughness larger than the wavelength of visible light is a fundamental property of these tools, as well as the lack of contact with the test object that is especially important for dynamic measurements. Conventional sensors inevitably load a test object and therefore perturb the dynamic response.

This project is focussed on the speckle interferometry since it is considered to be one of the best established optical techniques for noncontact vibration measurements.

It is now widely acknowledged that speckle interferometry (SI) offers powerful techniques to characterize rough surfaces with a submicron accuracy in static or quasi-static regime, when small displacements are involved (typically several microns or tens of microns). The issue of dynamic regimes, with possibly large deformations (typically hundreds of microns or more), is still topical and prevents an even more widespread use of speckle techniques. This is essentially due to the lack of efficient processing schemes able to cope with non-stationary AM-FM interferometric signals[1]. In addition, decorrelation induced phase errors represent a hindrance to accurate measurement when such large displacements and classical fringe analysis techniques are considered.

Depending on the application requirement, vibration can be measured at a single point (e.g., laser vibrometers) or simultaneously at several points (e.g., multipoint or full-field speckle pattern interferometry). Laser vibrometers enable the vibration amplitude and phase to be determined with a practical bandwidth from static to MHz[2,3]. However, laser vibrometers are generally intended to make measurements of out-of-plane and in-plane displacement at a single point on the surface of the test object[4,5]. Consequently, in order to determine the vibration modal properties of a test object, it is necessary to scan the object beam over its surface, so adding complexity to the optical arrangement and demanding that the vibration is stationary over the time in order to take a complete scan. Hence there are situations where a full field measuring instrument is required.

Full- field interferometric measurement of dynamic displacement is well established thanks to holography and speckle pattern interferometry (SPI)[6,7]. The main difference is between their operating principles. In electronic speckle pattern interferometry (ESPI), two states of an object are compared by recording a speckle interferogram corresponding to each of the two states, and then carrying out a digital correlation between them[8]. On the other hand in holography, the wave front scattered from the test object in its first state is recorded holographically and then, by mixing the reconstructed wave front from the test object in its first state with a real wave front from the object in its second state, it is possible to produce the so called live fringes[9]. The fringe quality obtained with Holography is higher than the quality obtained with speckle correlograms, but the operational practical advantages of ESPI are usually an important factor in the choice of the technique.

From the perspective of the instrumentation development, there are two distinct classes of experiment, namely periodic or harmonic deformation and transient or non- periodic motion. For periodic motion, “standard” SPI enables the vibration amplitude to be measured at a number of points simultaneously; data are captured in the form of video frames with exposure times which are long in comparison with the period of the motion. Conversely for transient deformation, the instrumentation must be developed to permit shorter exposure times since the low-bandwidth video frame-rate of the detectors normally used (typically 25 Hz), imposes a temporal averaging that “loses” the phase of self-excited or transient vibrations[10].

So “traditional” full-field interferometers cannot provide time-resolved measurements due to their relatively low sampling rate compared to the vibration period, and their use is limited to applications in which deformations are quasi static or harmonic.

In 2006 the Optics Group at Heriot-Watt University demonstrated a multipoint vibrometer based on a CMOS camera and inter-frame phase step. This high speed SPI system is able to measure the temporal evolution of dynamic deformation; the maximum surface velocity that can be reliably measured corresponds to ± 0.3 times the surface velocity at which the interferogram is sampled at the Nyquist limit.
Using the experience of this high-speed system, we developed the experimental system on which the work of this research is based. The main changes over the previous system are related to the detector used and to a different data processing strategy. These modifications enable an increase in the detector data transfer rate with respect to a system using a standard high speed detector, at the same frame rate and at the same number of measurement points. In other words, the data transfer rate increase is related neither to frame rate or to the number of pixels considered, but to how the data are acquired by the detector and how they are processed.

1.2 Organization of thesis

Chapter 2 reviews the existing optical techniques for vibration measurement, which are especially based on SPI and carrier based methods, for either low-speed and high-speed detection. Alternative high-speed detectors based on correlation schemes and on lock-in of modulated light that were relevant for the development of the actual Modulated Light Camera (MLC), are also described.

Chapter 3 introduces our novel approach for vibration measurement, based on the characteristic of the novel CMOS detector developed at Nottingham University Electronic Group. Simulations, showing how the theoretical model works, are also presented.

The characterization of the camera response is discussed in Chapter 4. A calibration of the response is also described.

The experimental work is described in Chapter 5. The new SPI setup for the inter-frame phase stepping is shown. Experimental results obtained by time-averaged SPI, single

point laser vibrometer and high-speed inter-frame phase stepping measurements are discussed.

Chapter 6 concludes the thesis illustrating the final conclusions achieved and the future work aiming to improve the experimental system performance.

Chapter Two

Literature review

2.1 Optical techniques for vibration measurement

One way to classify optical techniques based on interferometry could be on the basis of their sensitivities and consequently their aims. The two main domains of application are shape measurement and deformation measurement.

Fringe projection and Moire'[10, 12] are the "standard" whole field methods for shape measurement of large and deep objects. Sensitivities can range from the decimetre to a fraction of millimetre. Such low sensitivities make these techniques insensitive to most environmental perturbations, hence their application is not limited to the laboratory. The fringe projection method, which entails projecting a fringe pattern or grating on an object and viewing it from different directions, is gaining grounds in many engineering applications and in particular in the automotive field. Fringe projection is based on the triangulation principle, and it can be considered a geometric optical method. Many techniques have been proposed to measure the surface shape of an object in fringe projection profilometry (FFP)[13], such as Fourier transform profilometry (FTP), continuous wavelet transform (CWT), windowed Fourier transform (WFT) and Gabor transform. Contouring with holography or speckle interferometry[14, 15] is used for smaller objects and higher resolutions.

On the other hand, holographic or speckle interferometry are ideal tools when it is of interest to detect in-plane or out-of-plane deformation thanks to their high sensitivities to both components. These techniques can also play a role in defect detection; shearing speckle interferometry is often used to detect delamination in composite panels or in the study of concrete damages caused by frost. If fringe projection can provide accuracy on the order of a fraction of millimetre or sometimes better, holographic and speckle interferometry provide accuracy down to tens of nanometre for out-of-plane displacements. In-plane deformations can be measured with resolutions ranging from hundreds of nanometres to tens of micron, depending on the sensitivity chosen. A rule of

thumb for all these methods is to consider that the fringe analysis techniques used for processing the interferograms can bring a resolution that ranges from a tenth to hundredth of the interferometer's sensitivity. On the other hand this high sensitivity means that even small perturbations in the experimental environment will translate in a perturbation of the fringe pattern making it hard to use them out of well the laboratory controlled enviroment.

The analysis techniques for use with speckle interferometry for vibration measurement are presented in the next sections.

2.2 Speckle Pattern Interferometry

2.2.1 Interference: the 2-beam equation

When two beams are separated with appropriate apparatus and subsequently recombined, geometrical optics is not able to explain the phenomenon that occurs. The light distribution in the region of superposition can have maxima, that exceed the sum of the intensities of the beams, and minima, which can be zero. This is the interference phenomenon, demonstrated by Thomas Young and his famous double-slit experiment at the very beginning of the XIXth century. In this section, we will limit ourselves to the case of interferences with strictly monochromatic waves.
Let us consider two scalar waves of complex amplitude[16]:

$$A_m(x,y) = E_m(x,y)\exp(i\phi_m) = E_m(x,y)\exp(ikz_m) \quad (2\text{-}1)$$

with $k = \frac{2\pi}{\lambda}$ and where E_m (m=1,2) is the real value amplitude of the field, $\boldsymbol{\lambda}$ the light wavelength , z_m the coordinate along the propagation direction, x and y the coordinates in the transversal plane. The time dependence of the field has been skipped, and we assume that the fields are monochromatic, stem from the same source and propagate co-linearly in air. In the overlapping region, the total complex field is (the spatial coordinates have been skipped for simplicity):

$$A_{tot} = A_1 + A_2 = E_1\exp(i\phi_1) + E_2\exp(i\phi_2) \quad (2\text{-}2)$$

And the resulting intensity is:

$$I_{tot} = A_{tot} \cdot A_{tot}^{*} = I_1 + I_2 + I_{12} \quad (2\text{-}3)$$

where * denotes complex conjugate, and I_{12} is the interference term and equals to:

$$I_{12} = 2\sqrt{I_1 I_2}cos\Delta\phi \quad \text{, with } \Delta\phi = \phi_1 - \phi_2 = \frac{2\pi}{\lambda}OPD \quad (2\text{-}4)$$

OPD is the optical path difference between the reference arm and the measurement arm, i.e. the quantity of interest in interferometry. This is the well-known 2-beam equation generally written as[17]:

$$I_{tot} = I_o + I_m cos\Delta\phi \quad (2\text{-}5)$$

where I_o is the background intensity and I_m is the modulation intensity. The ratio I_m/I_o is the fringe visibility or fringe contrast ranging from 0 to 1. Optical sensors are sensitive to intensity and this fringe contrast becomes thus of primary importance as it is the determining factor of the measurement quality of the phase $\Delta\phi$.

2.2.2 Origin of speckle

Laser speckle patterns arise whenever light from a coherent source illuminates an optically rough surface. A surface is optically rough if the local surface height deviations are greater than the wavelength of the light. When light illuminates an optically rough surface, each point in the illuminated region scatters light. If the light is coherent, the light scattered from different points in the illuminated region will combine and produce an interference pattern. The speckle pattern is therefore the sum of the interference from all points in the region. Fig. 2.1 shows examples of interference where beams are not co-propating.

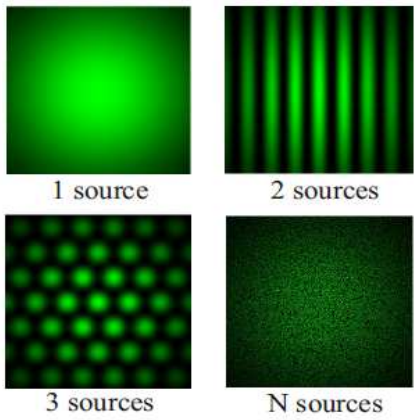

Fig. 2.1. Interference with several sources. [18]

A speckle pattern exists in all of the surrounding space and can be observed on a viewing screen placed some distance from the illuminated region. The speckle pattern seen on the screen is known as an objective speckle pattern. The average size of an objective speckle, generated from a region with the diameter of D, is given by [18]:

$$\Delta x = \frac{L\lambda}{D} \tag{2-6}$$

where L is the distance between the viewing screen and object and λ is the wavelength of the light. The speckle is termed "objective", because for a given illumination, the scale of the speckle depends only on the position of the plane where it is viewed. If such a speckle pattern is imaged onto the screen by a lens, a "subjective" speckle pattern is formed. The spatial distribution of this speckle is determined by the diffraction limit of the imaging system. Subjective speckle size is taken as the separation between the first two minima of the diffraction Bessel function and thus is dependent on the focal length f and lens aperture D_a. The average size of an individual subjective speckle observed at the imaging plane may be expressed as [18]:

$$\sigma \approx \frac{\lambda f}{D_a} \tag{2-7}$$

Speckles were initially considered as an addition and unwanted effect of the laser. Most of the early research into laser speckle was aimed at its reduction, because the speckle noise deteriorates the quality of holographic reconstruction. Later work to use the information

carried in laser speckle became known as speckle metrology. Speckle pattern interferometry (SPI) was developed in the early 1970s. The technique has progressed from photographic recording, through analogue video recording on to its current implementation with digital Charged-Coupled Devices (CCDs). The electronic processing of video and CCD camera signals eliminated the wet processing that had been somewhat problematic in conventional holographic interferometry, whilst the optical setup and subsequent processing are somewhat more straightforward than for digital holographic interferometry.

2.2.3 The interferometer sensitivity

In SPI setups, in contrast with classical interferometry, the link between the change of the physical quantity and the optical phase depends on both the illumination direction and the observation direction. We usually define the observation direction as the line joining any point M on the object surface to the pupil centre of the recording device (CCD or CMOS camera). In a similar manner, we define the illumination direction as the propagation direction of the beam impinging the object at the same point M. We respectively associate the vectors $\overrightarrow{K_0}$ and $\overrightarrow{K_i}$ to those directions. We can then define the so-called sensitivity vector $\vec{S} = \overrightarrow{K_0} - \overrightarrow{K_i}$ of the speckle interferometer (Fig. 2.2).

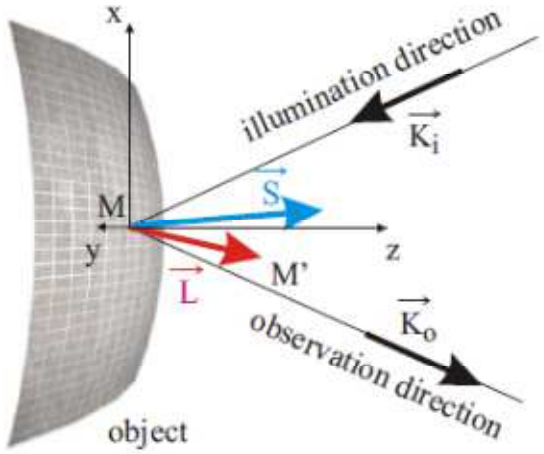

Fig. 2.2. Speckle interferometer sensitivity. [18]

This leads to the very general formula which gives, for a defined displacement $\vec{L} = \overrightarrow{MM'}$, the corresponding phase change [18]:

$$\Delta\phi = \frac{2\pi}{\lambda}\vec{S} \cdot \vec{L} \qquad (2\text{-}8)$$

A typical interferometer for out-of-plane displacement measurement (i.e. sensitive to displacements normal to the object surface) is shown in Figure 2.3:

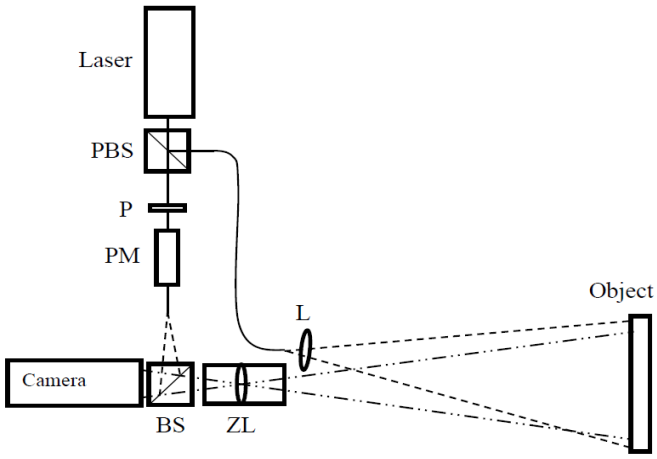

Fig. 2.3. Schematic of out-of-plane SPI setup. [27]

Light from the laser is collimated and divided by a beam splitter into two beams, which are the object beam and the reference beam. A polarising beam splitter (PBS) is shown in Figure 2.3, which enables the intensity ratio between the two beams to be varied. Also, highly birefringent (polarisation maintaining) fibre optic cable is used, enabling the polarisation state of the two beams emerging from the two fibres to be matched. A linear polarizer (P) is used to eliminate possible unwanted components in the reference beam before it is modulated by a phase modulator (PM) to generate phase steps between the two interfering beams. The object beam is expanded by a lens (L) to illuminate the object. The scattered light is collected by zoom lens (ZL) and forms an image of the object that contains a laser speckle pattern. Light from the reference beam interferes with the speckle image and an interferogram is produced on the sensor. For out-of-plane SPI, the intensity of the reference beam recorded at the detector should generally be approximately 3-4

times the mean intensity of the object beam in order to obtain high contrast fringes. Light is scattered from the object and therefore only a small amount of the object beam is returned to the sensor. For this reason typically 90% of the light from the laser goes into the object beam and 10% goes into the reference beam.

The intensity of the interferogram recorded by the sensor can be represented by equation (2-9) [27]:

$$I_1(x,y,t) = I_0 + I_r + 2\sqrt{I_0 I_r}\cos\left[\psi(x,y) + \phi(x,y,t)\right] \quad (2\text{-}9)$$

where $I_o(x, y)$ and $I_r(x, y)$ are the intensities of the object and reference beams measured by the detector, and the coordinates x and y describe the pixel position in the plane of the detector. It is assumed that the beams are mutually coherent and have equivalent states of polarization. The phase $\psi(x, y)$ describes the random optical path difference between the object and reference beams due to laser speckle and $\varphi(x, y, t)$ is a phase due to the difference in optical path length between the object and reference beams. For the out-of-plane SPI system of Figure 2.3, the object illumination is approximately collinear with the optic axis of the imaging lens and camera, which is defined as the z axis. The component of object deformation or displacement resolved in the z-direction produces a change in the optical path length of the object beam, producing a change in the interferogram phase $\phi(x, y, t)$ and hence interferogram intensity. The phase change for a wave front that has travelled an extra distance l in the z-direction is given by [27]:

$$\Delta\phi = \frac{2\pi}{\lambda}\int_0^l n_z dz \quad (2\text{-}10)$$

where λ is the wavelength of the laser and n_z is the refractive index of the object beam medium along the z-direction. For a medium having unity refractive index, the previous equation simplifies to:

$$\Delta\phi = \frac{2\pi}{\lambda} l \quad (2\text{-}11)$$

After the target is deformed, the new interferogram intensity can be expressed by the equation:

$$I_2(x,y,t) = I_0 + I_r + 2\sqrt{I_0 I_r}\cos[\psi(x,y) + \phi(x,y,t) + \Delta\phi(x,y,t)] \quad (2\text{-}12)$$

Where $\Delta\phi$ is the phase change due to the displacement of the target. Due to the random speckle phase, displacement information contained in the change in intensity is not easily discerned without further processing. Therefore the two interferograms I_1 and I_2 are compared, usually by addition or subtraction, as described in the following section.

2.2.4 Fringe formation

One of the properties of SPI is its capability to display a fringe pattern in real time. Because the surface of the test object is rough on the scale of the wavelength of light, the interferograms denoted by equations (2-9) and (2-12) take the form of speckle patterns. The two interferograms are recorded digitally to form two different frames. The deformation which produces the phase change in (2-11) can be revealed by correlating the two frames, for example by subtracting one from the other:

$$\begin{aligned} I_s(x,y,t) = I_2 - I_1 &= 2\sqrt{I_o I_r}(\cos[\psi + \phi] - \cos[\psi + \phi + \Delta\phi]) \\ &= 4\sqrt{I_o I_r}\sin\left(\psi + \phi + \frac{\Delta\phi}{2}\right)\sin\left(\frac{\Delta\phi}{2}\right) \end{aligned} \quad (2\text{-}13)$$

The subtraction fringe pattern denoted by equation (2-13) is usually produced with continuous wave illumination and it is used for static or harmonic vibration deformation measurements. The negative intensity values are usually removed by assigning the absolute value of the intensity difference. The term $\sin\left(\psi + \phi + \frac{\Delta\phi}{2}\right)$ represents the high spatial frequency random speckle phase in the image and $\sin(\frac{\Delta\phi}{2})$ is a lower spatial frequency modulation, that is the fringe pattern.

For points in the object that don't move between frames, their brightness remains constant (full correlation); points that move such that the corresponding optical path length changes by an integral number of laser wavelengths, M, also have a constant brightness, because of the fundamental periodicities of interferograms; points moving by M+1/2 wavelengths would change from bright to dark, or vice versa, and hence they show an

anti-correlation. Differences between the two speckle interferograms are therefore revealed by alternating bright and dark fringes that contour regions of equal displacement between frames. For the system shown in Figure 2.3, the phase difference related to the optical path difference due to displacement of the object is:

$$\Delta\phi = \frac{2\pi}{\lambda}\eta w \tag{2-14}$$

where η is the interferometer's sensitivity to object displacement w, resolved in the observation direction. For collinear illumination and observation directions $\eta=2$. For observation normal to a plane surface, w is the out-of-plane displacement of the object. Then the difference in out-of-plane deformation between adjacent fringes is w=$\boldsymbol{\lambda}$/2.

2.3 Traditional SPI for vibration measurement: low speed detection

2.3.1 Time average SPI

Butters and Leendertz[19] first employed SPI for measurement of out-of-plane vibration.
Let us assume we are making measurements on a test object whose surface is undergoing harmonic vibration, so that the out-of-plane displacement is described by:

$$w_n = w_o cos\,(\Omega t + \Phi) \tag{2-15}$$

where w_o is the amplitude, Ω the frequency and Φ is the phase of the vibration. Recalling Equation (2-14) is easy to calculate the change in optical path length between the object and the reference beams due to the out of plane deformation, w_n. Using normal illumination and detection:

$$\phi = \frac{4\pi}{\lambda} w_0 \cos\,(\Omega t + \Phi) \tag{2-16}$$

Provided that the vibration period is significantly shorter than the detector exposure period so that we can assume a complete number of cycles of the harmonic motion occur

during an exposure, the instantaneous optical intensity measured in the plane of the detector can be written as[20]:

$$I_1(x,y,t) = I_o + I_r + 2\sqrt{I_o I_r}\cos[\psi(x,y) + \phi(x,y,t)] \quad (2\text{-}17)$$

Equation (2-17) can be further evaluated to give:

$$I_1(x,y) = I[1 + V\cos(\psi)J_o\left(\frac{2\pi w_o}{\lambda}\right)] \quad (2\text{-}18)$$

where $I(x,y) = I_o(x,y) + I_r(x,y)$. $V = \frac{2\sqrt{I_o I_r}}{I}$ is the visibility of the interference and achieves its maximum value, that is unity, only if the two combining beams are of equal intensity and state of polarization and are mutually coherent. The time averaged interference pattern consists therefore of a speckle pattern in which the contrast is modulated by the Bessel function J_o. In equation (2-18) we can find information about the vibration amplitude w_o , but information about vibration frequency and phase have been lost.

Background intensity I degrades the SNR. In order to obtain good fringe quality, a common method is to record two time-averaged speckle images with a π phase step between recordings. The second image when the object is still vibrating shall be:

$$I_2(x,y) = I[1 + V\cos(\psi + \pi)J_o\left(\frac{2\pi w_o}{\lambda}\right)] \quad (2\text{-}19)$$

With sequential subtraction analysis, each frame acts as the reference frame for the next so that the reference frame is always refreshed. Subtraction of the two frames yields:

$$I_1 - I_2 = 2IV\cos(\psi)J_o\left(\frac{2\pi w_o}{\lambda}\right) \quad (2\text{-}20)$$

The brightest fringes correspond to vibration nodes and the fringe intensity decreases with increasing vibration amplitude. Subsequent high fringe orders are of low contrast and so it is difficult to calculate higher vibration amplitude from the Bessel fringes.

Lokberg and Hogmoen [21, 22] described how phase modulation combined with time-averaged ESPI can be used to plot contours of constant phase and how it can extend the

amplitude measuring range of “classical” time averaged ESPI. Their method consists of modulating the mirror that reflects the reference beam, at the same frequency as the object vibration but with amplitude and phase slightly different. So the information about the amplitude and phase of the object is coded against the amplitude and phase of the reference mirror. The position of the zero order fringes no longer represent the nodal regions of the object, but regions vibrating at the same amplitude and phase as the reference mirror. Furthermore, by regulating the amplitude and the phase of the reference mirror, it is possible to obtain fringes in regions where the fringe information would be lost by the ordinary time-averaged recording.

Nakadate [23] used a level-slicing technique to increase the contrast of a fringe pattern.

2.3.2 Pulsed SPI

Time-averaged techniques are restricted to harmonic motion, and even the information that we can recover is restricted. More information can be gained by reducing the exposure time in comparison with the period of the highest frequencies present in the motion since the basic principle is that shorter exposures will “freeze” the motion. This means that the phase due to object deformation can be considered constant during the exposure. Although a reduced TV camera exposure may be used in this sense, it is more common to use pulsed illumination.

Pulsed SPI was first reported in 1978 [24] with a double-pulsed laser and a low speed camera was used to record addition and subtraction fringes. The classification of pulsed techniques depends on how many pulses occur per TV frame, and whether the motion studied is harmonic, or transient.

When we measure a harmonic vibration, it is possible to synchronize the laser pulses to particular vibration phases. One laser pulse is fired to record a reference speckle pattern when the object is at some initial position.

$$I_1(x,y) = I\left\{1 + Vcos\left[\psi + \frac{4\pi w_o}{\lambda}\cos\left(\phi_1 + \Phi\right)\right]\right\} \qquad (2\text{-}21)$$

Then another laser pulse is fired to record another speckle pattern when the object has deformed.

$$I_2(x,y) = I\left\{1 + Vcos\left[\psi + \frac{4\pi w_o}{\lambda}\cos\left(\phi_2 + \Phi\right)\right]\right\} \quad (2\text{-}22)$$

The two speckles can be correlated to form fringes denoting object deformation between the two pulse positions. For example we subtract the two equations (2-21) and (2-22) and without loss of generality we can assume $\phi_1 = 0$ and $\phi_2 = \pi$:

$$I_2 - I_1 \approx IVsin(\psi')\sin\left(\frac{1}{2}\phi\right) \quad (2\text{-}23)$$

In contrast to time average measurements previously discussed, pulsed measurements retain information regarding the phase of the object deformation.

Dual-pulse techniques are commonly used and it is assumed that the vibration frequency is higher than the camera frame rate so that two pulses occur during an exposure. As well as in the previous section, two interferograms corresponding to different vibration phases are correlated. Since the laser pulses are short compared to the vibration period, the motion is effectively frozen and even transient (but repeatable) surface vibration can be analyzed.

There are three typical modes of operation, namely addition [24,25], subtracted-addition[26, 27] and subtraction. In the addition method, a double pulsed laser fires double pulses with a very short pulse separation within a single frame. The resultant addition fringes contain stationary optical noise that reduces fringe visibility.

Moore and Perez-Lopez[28] reported the calculation of the optical interference phase directly from double-pulsed ESPI addition fringes using phase stepping techniques, for an object undergoing harmonic vibration. The laser pulses are shifted with respect to the object vibration phases and then two techniques are analyzed to improve fringe visibility: subtraction of a reference interferogram recorded when the object is stationary form an addition fringe pattern, and subtraction of addition patterns.

For subtraction pulsed SPI, interline-transfer CCD cameras have proved to be very effective. Interline transfer sensors have alternating columns of photosensitive columns for recording light and masked columns that prevent light from striking the CCD. To start an exposure, charge from the CCD is cleared with a single pulse. At the end of the exposure, another pulse is sent to the CCD that causes each of the photosensitive columns to simultaneously be shifted into the adjacent masked column. The image is then read

from just the masked columns just like a full-frame CCD. This simultaneous shifting into the masked columns creates the "electronic shutter" mechanism of an interline transfer sensor. Because the entire image is shifted under the masked columns in a single operation, it can then be read from the CCD even while light is still striking the photosensitive columns, so a mechanical shutter isn't needed.

Spooren [29] first demonstrated the improvement in fringe visibility compared to addition SPI, whilst maintaining a very short (microsecond) pulse separation.

For measurement of repeatable transient events[30], a series of tests under identical loading conditions can be conducted, incrementing the delay between the event start and the laser pulses until a complete composite history of the transient event is synthesized. The reported system uses single pulse subtraction and double pulsed addition TV holography with both in plane and out-of-plane optical configurations. The authors use an original synchronization system to obtain the subtraction and the addition correlation fringes that are shown in Figure 2.4:

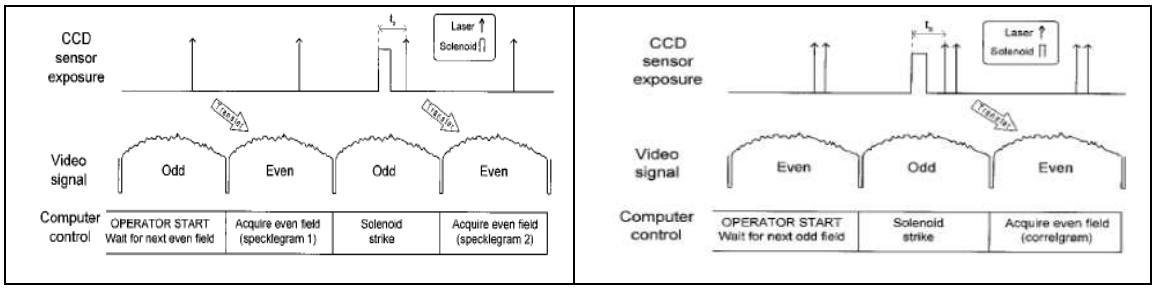

Fig. 2.4. Single-pulsed subtraction (left) and double-pulsed addition modes of operation. [30]

The setup was applied to measurement of the propagation of mechanical shock waves in a cantilever specimen and their subsequent diffraction by a crack in the specimen. Experimental results showed that double-pulsed-addition SPI was more attractive because it allowed the deformation in larger areas without exceeding the resolvable fringe density and it was more insensitive to environmental disturbances. However, single pulse subtraction was also of interest due to the improved fringe visibility.

Shellabear [31] developed a three-dimensional pulsed subtraction SPI system to measure the vibration of a turbocharger blade, a thick annular cylinder, and a centre-pinned free square plate. It was shown that the orthogonal displacement components could be measured independently and sequentially by SPI. A dual-beam illumination arrangement was used for in-plane vibration components. Vibration amplitude information was extracted using a

single phase step technique for the horizontal and vertical components of in-plane vibration. The results were then combined to yield the total in-plane vibration mode.
Concluding this section, we can say that even with pulsed illumination it is not possible to follow a transient deformation that is too fast in comparison with the frame rate. However measurement remains feasible provided that the motion is repeatable.

2.3 High speed detection and carrier based methods

2.3.1 High speed temporal phase stepping methods

When measuring transient deformations that are not harmonic is of interest, if pulsed laser illumination is the chosen technique, it will require high pulse energy, sufficient to give good exposure with either one or two pulses per camera frame, where the standard frame rates are usually 50 Hz. The two pulses technique, when the motion is reproducible, can give with some shrewdness a complete composite history of the transient event. On the other hand using a high-speed camera, with short exposure time and high framing rate combined with a continuous wave laser source, represents a simple solution to enable the measurement of NON-reproducible transient deformations[32]. The temporal resolution that is achievable is restricted only by the camera framing rate and the laser power available; furthermore the camera frame rate determines the maximum surface velocity that is reliably measurable.
A schematic of the experiment reported is in Figure 2.5:

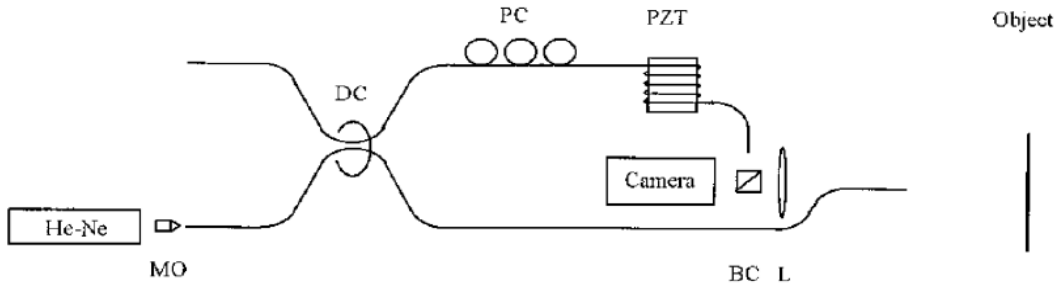

Fig. 2.5. Schematic of fibre optic ESPI arrangement. [32]

For this setup, a 10-mW He-Ne laser (633nm) and single mode fibre illumination was used jointly with a 40,000 fps CCD camera (64x64 pixels). The reference arm contains a polarization controller (PC) in order to maximize the visibility and a PZT (its bandwidth

is however insufficient for dynamic inter-frame phase shifting) to permit phase stepping by straining the fibre. For this arrangement, when the test object is harmonically vibrating, the intensity recorded by the camera at pixel (x,y) during an exposure of duration t_s, centred at time t_n, can be approximated by [32]:

$$I_n(x,y,t_n) = I\left(1 + V\frac{1}{t_e}\int_{t_n-\frac{t_e}{2}}^{t_n+\frac{t_e}{2}} cos\left[\psi + \frac{2\pi\eta w_o}{\lambda}\cos\left(\Omega t_n + \Phi\right)\right]dt\right) \qquad (2\text{-}24)$$

If the exposure periods are short with respect to the vibration period, it is possible to approximate the deformation by a linear expansion, that is the surface velocity is assumed to be constant and sinc function arises because the integration time is long compared to that of pulsed illumination:

$$I_n(x,y,t_n) = I\left(1 + Vsinc\left[\frac{2\pi\eta}{\lambda}w_n'\frac{t_e}{2}\right]cos\left[\psi + \frac{2\pi\eta w_o}{\lambda}\cos\left(\Omega t_n + \Phi\right)\right]\right) \qquad (2\text{-}25)$$

The sinc function represents the instantaneous visibility of the recorded speckle and to be maximum it requires a low surface velocity and a short exposure time.
Figure 2.6 shows a sequence of images recorded at 4,500 fps for a centrally pinned circular aluminium plate vibrating harmonically at 198 Hz.

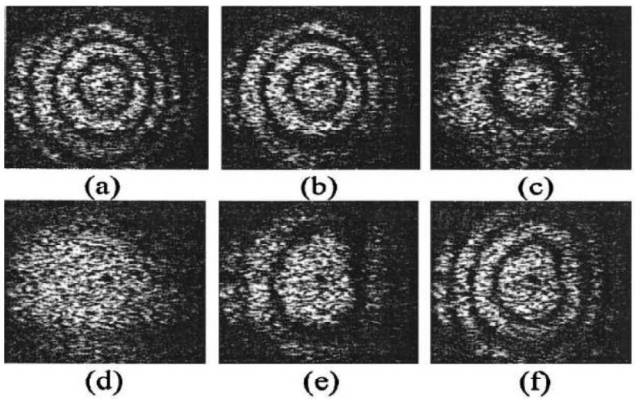

Fig. 2.6. Vibration fringes with camera not synchronized with object vibration. [32]

When the camera exposure is then synchronized to the object vibration in order to acquire single frames at exact points of the object vibration, and when the PZT in the reference

arm is controlled so that it introduces phase steps by $\pi/2$ rads between exposures, four optically phase stepped fringe patters are recorded as shown in Figure 2.7:

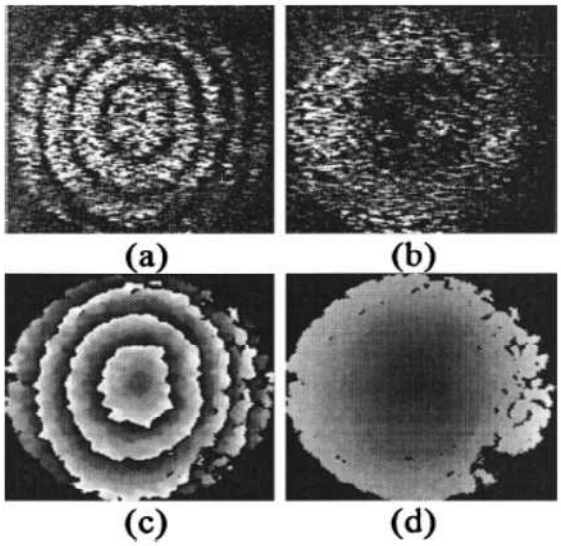

Fig. 2.7. Vibration fringes (a) and (b) and phase (c) and (d) with camera exposure Synchronized. [32]

Figure 2.7 (a) shows the first of four phase stepped images and (b) shows the object vibrating at the same frequency and amplitude as in (a) but with the camera trigger shifted by 90°. Figures (c) and (d) shows respectively the phase in range $\pm\pi$ obtained with the four bucket algorithm and the continuous phase without phase discontinuities.

J.M. Kilpatrick et al.[33] described a high speed digital speckle pattern interferometer which uses a line scan camera and a wave guide phase modulator for the measurement of complex deformation at audio-acoustic frequencies. Reducing the spatial resolution allows an increase in the temporal resolution, so by getting a good compromise between these two factors it is possible to see the system reported and shown in Figure 2.8 as a multipoint vibrometer:

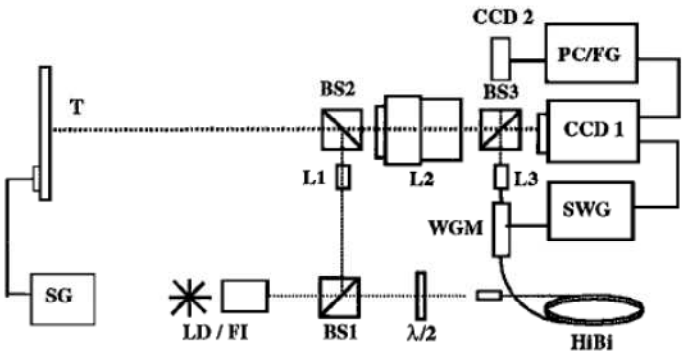

Fig. 2.8. Multichannel interferometer for out-of-plane vibration measurement. [33]

An 80 mW laser diode with a wavelength equal to 830 nm was used. The detector used (CCD1) is a high speed line-scan camera (256x1 pixels) operating at 100 kHz. A secondary array detector (CCD2) working at 25 fps is used to identify regions of interest (ROI). WGM is the waveguide phase modulator introduced in the reference arm to create phase steps in the reference beam and it is driven by the staircase waveform generator (SWG). The system uses highly birefringent optical fibres. A time-averaged subtraction interferogram is recorded by CCD2 with the target vibrating at 250Hz as shown in Figure 2.9.

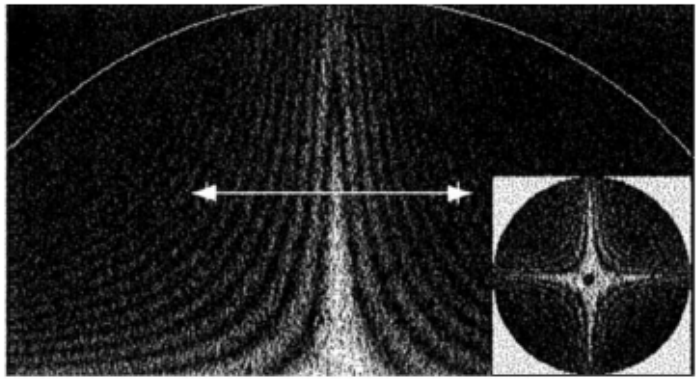

Fig. 2.9. Time average subtraction interferogram recorded by CCD2 with the target vibrating at 250 Hz. [33]

The line indicates the ROI, i.e. the data acquisition line of the high speed interferometer. The intensity recorded by CCD1 integrated over a single frame is:

$$I_n(x,t_n) = I\left(1 + Vsinc\left[\frac{2\pi\eta}{\lambda} w_n' \frac{t_e}{2}\right] cos[\Phi_o(x,t_n) - \Phi_r(x,t_n)]\right) \quad (2\text{-}26)$$

The object phase $\Phi_o(x,t_n)$ includes the random speckle phase ψ and the phase due to the out-of-plane deformation of the object $\frac{2\pi\eta w_n}{\lambda}$. The reference phase $\Phi_r(x,t_n)$ includes a phase shifted increment 2πn/N, where N is the number of steps per period. When the number of steps used is N=4, we can recover the argument of the cosine term in equation (2-26) by the Carre´ algorithm[33]:

$$\Phi_o(x,t_n) - \Phi_r(x,t_n) = tan^{-1}\left(\frac{\{[3(I_{n+1} - I_{n+2}) - (I_n - I_{n+3})][(I_n - I_{n+3}) + (I_{n+1} - I_{n+2})]\}^{1/2}}{(I_{n+1} + I_{n+2}) - (I_n + I_{n+3})}\right) \quad (2\text{-}27)$$

The argument of the cosine term is recovered correctly only if the frame rate is sufficiently high to assume that the surface velocity is linear during any four consecutive frames. Hence the phase at a given pixel can be calculated from I_n to I_{n+3}.

It is worth mentioning that the phase step between frames introduced by the phase modulator is slightly modified by the surface motion that has taken place between frames. To a first approximation this phase change is similar to a linear miscalibration of the phase modulator, an error to which the Equation (2-27) is insensitive.

The out of plane deformation obtained at t_n=T relative to deformation at t=0, is obtained by summation of the incremental phase differences at the corresponding pixels between adjacent frames[33]:

$$w(x,T) = \frac{\lambda}{2\pi\eta}\sum_{0}^{T-1}[\Phi_o(x,t_{n+1}) - \Phi_o(x,t_n)] \qquad (2\text{-}28)$$

Processing each pixel separately avoids the difficulties related to the spatial unwrapping that arise when adjacent pixels are vibrating out of phase each other.

The Nyquist condition, that the cumulative phase change associated with the argument of the cosine term in Equation (2-26) be sampled at least twice per fringe [34], leads to a maximum working surface velocity:

$$v_{Nq} = \pm\frac{\lambda}{2\pi t_s}[1 \mp (2/N)] \qquad (2\text{-}29)$$

In the experiment described, for a time exposure t_s=10μs, N=4, the maximum surface velocity measurable is 3.2 mm s^{-1}. The π/2 phase steps are added to the reference beam during the blanking period between frames and data are transferred to PC at a frame rate of 100 kHz. After data processing a spatiotemporal speckle pattern images composed of 256 (horizontal) x 512 (vertical) pixels is obtained, with each row corresponding to a single frame exposure (Figure 2.10). The data are finally processed with the Carre´ algorithm to recover the phase, and, after removing 2π discontinuities and summing phase differences, it is possible to recover the object deformation.

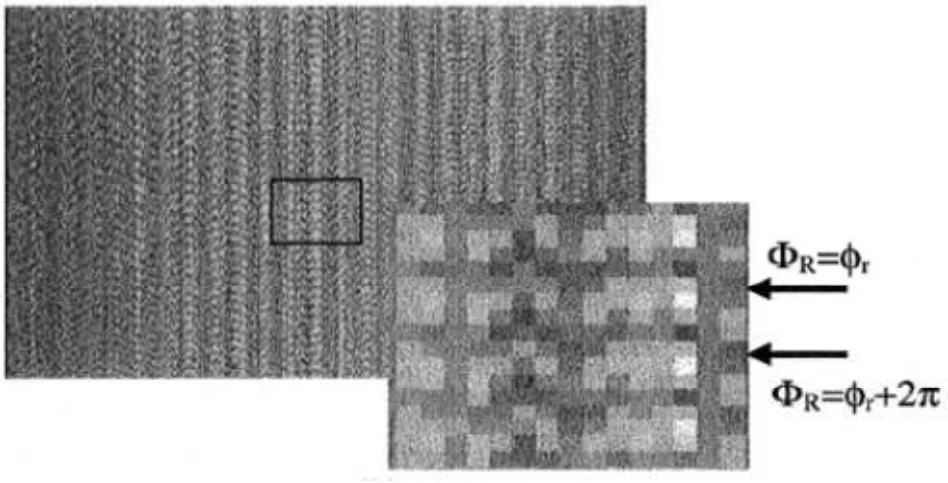

Fig. 2.10. Gray scale spatiotemporal speckle pattern. [33]

Using the experience of the two high speed systems so far reported, Tao Wu [35, 36] proposed an inter-frame phase stepped SPI system based on a CMOS camera, reporting a numerical and analytical error analysis in order to determine the maximum surface velocity that could be reliably measured with inter-frame phase stepping. Improvements over the previous systems had been incorporated:

- A CMOS camera permitting random pixel access and therefore any region of interest on the object to be selected (instead of two different CCD linear arrays).
- Experimental implementations regarding the laser power, compact interferometer design and electro-optic phase modulator.

A schematic of the system is shown in Figure 2.3. A 5 W laser diode-pumped (single frequency CW) with a wavelength equal to 532 nm was used, limiting the output power to 500mW in order not to damage the proximal fibre ends. The beam splitter (PBS) is adjusted so that about 60% of laser output is launched in the object beam fibre. The object is imaged by a photographic zoom lens (ZL) onto the 1024x1024 element array of a CMOS camera which permits random pixel access. The phase modulator (PM) generates phase steps of $\pi/2$ radians in the reference beam and it has a bandwidth up to 20 GHz. In order to introduce an inter-frame step, a camera frame synchronization signal was passed from the PC controlling the CMOS camera to a staircase wave form generator (SWG). In this way the SWG produces a staircase voltage with N equal steps, in which every step is synchronized to the camera frame rate. When the CMOS camera starts to record, a pulse

at the beginning of each frame is sent to the SWG; this converts these pulses into a staircase voltage and its gain is adjusted to produce phase steps of $\pi/2$ radians in the blanking period between frames. The SWG's output is sent to the PM to produce inter-frame phase steps in the reference beam. A linear polarizer (P) was inserted in the collimated output from the fibre before the phase modulator, in order to delete the leaked component of the reference beam that was revealed to be responsible of considerable fluctuation of the intensity in the reference beam when different voltages were applied to the PM. Afterword the position of the phase steps with respect to the camera frame signal was validated to reduce the effects of the delay introduced by the electronics of the SWG and the phase modulator amplifier; due to this delay the applied phase steps could not be exactly during the periods between frames. Figure 2.11 shows the variation in mean phase step size with the test object stationary.

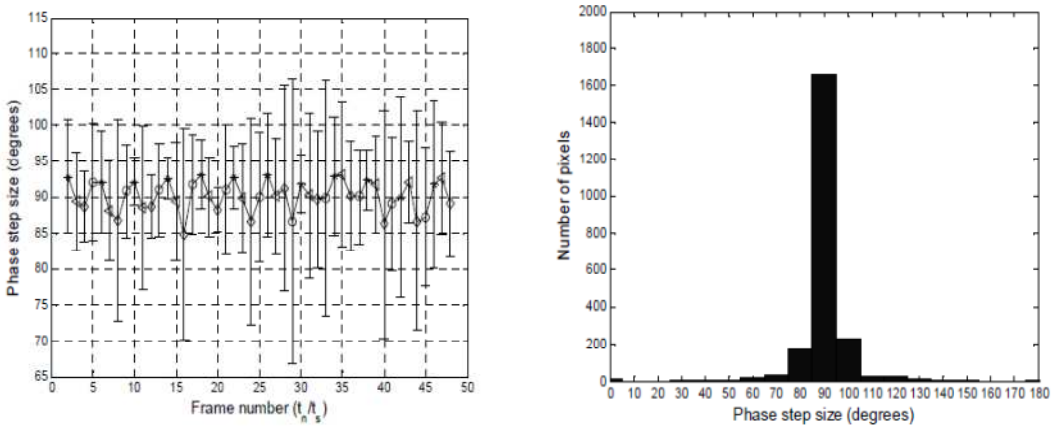

Fig. 2.11. Inter-frame step size plotted against frame number (left) and phase step size distribution for all frames recorded for a stationary object with a frame rate of 33kHz. [35, 36]

Before proceeding with vibration measurement is necessary to obtain a time averaged pattern and identify, from that, the region of interest (ROI) for time resolved measurements with the same CMOS detector. Figure 2.12 shows the time averaged pattern recorded with the CMOS camera working at only 70 fps (1024x1024 pixels) for a circular test object vibrating at 250 Hz.

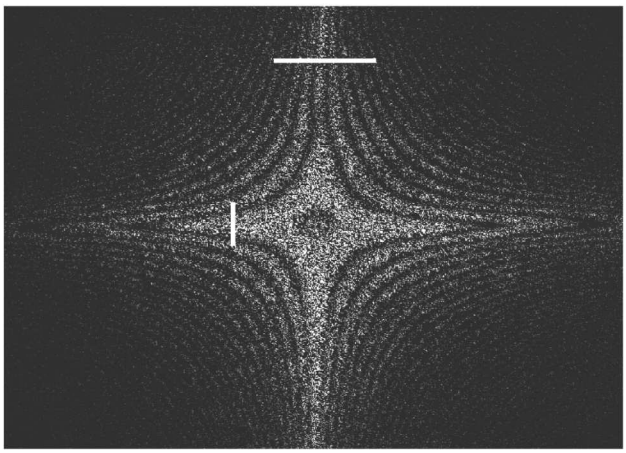

Fig. 2.12. Time averaged subtraction fringe pattern recorded at 70 fps for a target vibrating at 250 Hz. [35, 36]

The relative vibration phase between points on the line is not measured directly from the time averaged measurement, although it can be recovered for this simple case. The maximum vibration amplitude was estimated from the Bessel fringes to be 0.7μm, which corresponds to a maximum velocity surface of 1.1 mm/s. The horizontal ROI is interrogated at 33 kHz frame rate and a composite spatio-temporal phase stepped speckle interferogram (Figure 2.13) is created, in which each row corresponds to a single frame of 128x1 pixels.

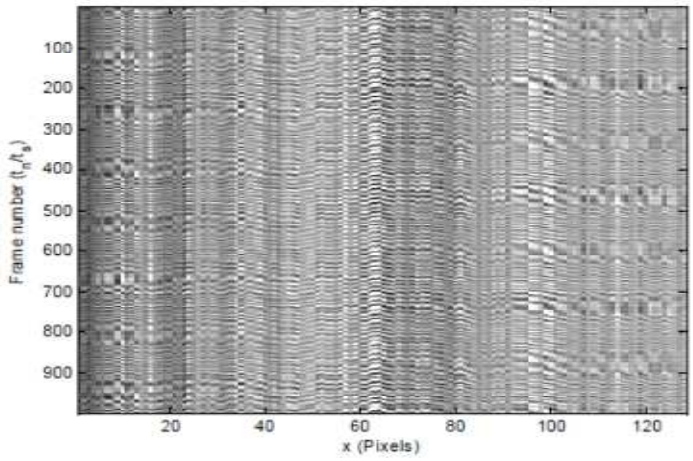

Fig. 2.13. Spatio-temporal speckle pattern recorded at 33 kHz. Variations for the horizontal ROI in Figure 2.3.8 are showed. [35, 36]

Assuming that the interferogram at each pixel is sampled within the Nyquist limit, it is possible to calculate the phase at each pixel from the recorded intensity from four adjacent

frames using Equation (2-27). The normalized surface velocity and surface acceleration are recovered from the two relations:

$$\frac{w'(x,y,t_n)}{|v_{Nq}|} = \frac{\Delta\Phi_o(x,y,t_n)}{\pi} \tag{2-30}$$

and,

$$\frac{w''(x,y,t_n)}{2\pi f|v_{Nq}|} = \frac{1}{2\pi^2 f t_s}\Delta^2\Phi_o(x,y,t_n) \tag{2-31}$$

where, $\Delta\Phi_o(t_n)$ is the phase difference between adjacent rows wrapped into the range $\pm\pi$ radians, and $\Delta^2\Phi_o(t_n)$ represents the rate of change in phase difference between frames. Normalized velocity and acceleration are showed in Figure 2.14:

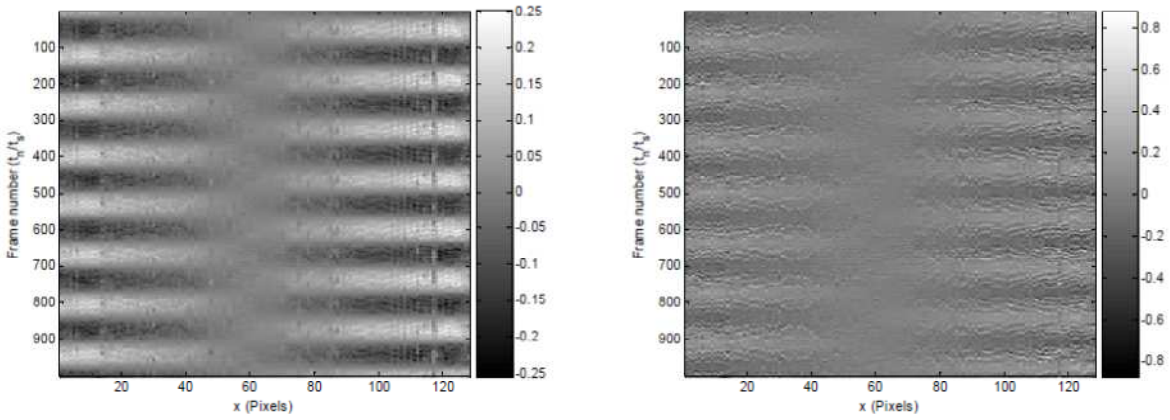

Fig. 2.14. Normalized velocity (left) and acceleration (right) for the horizontal ROI. [35, 36]

Considering Equation (2-29):

$$v_{Nq} = \pm\frac{\lambda}{2\pi t_s}[1 \mp (2/N)]$$

it is evident that the introduction of an inter-frame phase step reduces the measurement range because the total phase change related to the argument of the cosine term in Equation (2-26) must be sampled at least twice per fringe to meet the Nyquist condition. So the corresponding minimum and maximum surface velocities are different from that

we can recover from Equation (2-27). Furthermore inter-frame phase stepping assumes that the surface velocity could be considered linear during the N sequential measurements. Hence measurements errors, depending on surface velocity and acceleration, that is the frequency and amplitude of vibration, and camera frame rate arise and cannot be determined without a priori knowledge of the vibration measured. A numerical and analytical error analysis is reported by T. Wu in order to determine the maximum surface velocity that could be reliably measured with inter-frame phase stepping. The normalized velocity error ploted against surface velocity and frames number is shown in Figure 2.15 (a), while Figure 2.15 (b) shows the error analysis for high speed SPI acting as a multipoint vibrometer.

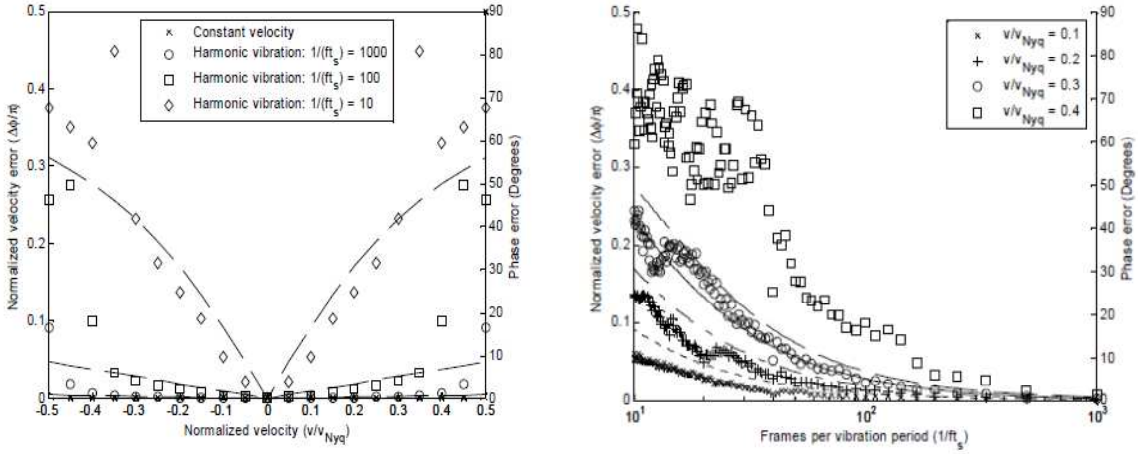

(a) (b)

Fig. 2.15. Maximum normalized velocity error plotted against surface velocity for Carre' algorithm (a) and maximum normalized velocity error plotted against number of frames per vibration period for Carre´ algorithm (b). [35, 36]

The maximum surface velocity that is reliably measurable is found to be

$v_{max} \leq 0.3|v_{Nq}|$ using the Carre´ algorithm.

Other implementations of moderately high-speed SPI included the measurement of unidirectional deformation with a moderately high-speed camera [37] (360 frames per second). Relatively low-speed (25 μms^{-1}) deformations were recorded using dynamic phase stepping at 1 kHz [38] and analysed by the temporal phase step method. Neither of

these two systems was intended for dynamic vibration measurements, which would require a substantial increase in bandwidth and change in data processing strategy.

In the temporal phase stepping approach for measuring surface deformation, the optimum algorithm to be used in order to correctly evaluate the phase from recorded intensity patterns, was investigated by Xavier Colonna De Lega [39, 40]. The 5 image algorithm, based on a preliminary estimation of the phase increment $\Delta\varphi$ that is added between adjacent frames, seems to offer a good compromise. This solution generates smaller error when the phase change between 2 recorded frames is in the range [45°, 135°]. Furthermore it generates a quite uniform error that is a function of the phase; its drawback is that when the phase change between any two adjacent frames is close to 0 or π, the method to estimate the phase increment, on which the 5 images algorithm is based, becomes unreliable. The case of non-linear phase evolution and the behaviour of the different algorithms analyzed had been also reported. The behaviour of the different algorithms, namely Carre´ algorithm, 5-images algorithm and 3-images algorithm, don't show important differences with respect to the type of non linearity introduced. This means that non linearity will introduce systematic errors that will be higher for pixel where the total phase increment is quite large. The errors will become more important in interferograms in which few fringes are shown.

Huntley et al. [41] investigated experimentally the optimal rate at which a reference speckle pattern should be updated when speckle interferometry is used to measure transient in-plane deformations. It has been reported that combining temporal phase unwrapping with periodic updating of the speckle reference pattern enables large in-plane deformations to be measured, well beyond the point at which speckle decorrelation would otherwise occur.

An important contribute, about decorrelation in speckle pattern, has been given by Mathias Lehmann [42, 43], who investigated decorrelation induced phase errors in speckle interferometry. Decorrelation in SPI introduces errors in the random phase and hence in the measurements, and the quantification of these errors is important since all speckle interferometers are subject to decorrelation. It was demonstrated that an important parameter that is responsible for decorrelation induced phase errors is the pixel modulation. Pixels with a high modulation have a low standard deviation of the phase errors, while on the other hand low modulation pixels yields large phase errors.

Ruiz and Huntley [44] raised the point that the camera framing rate and the carrier frequency of the system, which is equal to the ratio of the camera framing rate and the number of

phase steps per cycle of the carrier, impose restrictions on the maximum surface velocity that can be measured. The conclusion was that, for relatively low vibration amplitude (for example $\lambda/10$), vibration frequencies up to 30% of the carrier frequency can be measured with an rms phase change error less than 10% of the vibration amplitude.
Huntley et al. [45, 46] proposed an algorithm for temporally unwrapping noisy phase maps without any previous filtering.

2.4.2 Spatial phase step SPI

Spatial phase stepping represents an alternative to solve the problems related to temporal phase stepping that were discussed in the previous section. Spatial phase stepping records two or more phase stepped images simultaneously and is hence immune to time-related drawbacks even if it is more sensitive to image alignment errors due to its higher spatial resolution. The images are acquired and spatially separated onto one or multiple detectors and a fixed phase step is introduced between them. So this method avoids the errors due to phase changes between two different and adjacent frames, because the assumption made for inter-frame phase stepping that the velocity is linear during the acquisition of any four frames is no longer required. Furthermore, other time-dependent perturbations such as air fluctuations, temperature changes and random vibrations are equally avoided. The spatial phase step is usually introduced by polarizing elements, gratings or pixelated phase-mask.
For example, Haasteren and Frankena [47] have developed a speckle interferometer that is able to generate three phase stepped interference patterns simultaneously. The system includes three CCD cameras to record the images between which phase steps of $\pi/2$ are created without any mechanical motion. The system uses two Glan-Thompson prisms to direct the combined beams onto the three cameras and to introduce phase shifts between them. Filtering techniques are used to improve the quality of the measurements; the reported system is able to perform up to 25 phase measurements per second. The advantage of this system is that the displacement caused by dynamic processes can be monitored in real time. Moreover, since the recording time of the phase-stepped images is less than 40 ms, the system's accuracy is practically insensitive for time-dependent external perturbations such as air flow, temperature changes, and slow vibrations.

Using diffraction gratings to introduce the spatial phase steps, Upton and Watt [48] have reported a calibrated multichannel electronic interferometer to perform measurements of transient phenomena. The basic layout of the system is that of a Mach-Zehnder interferometer; two diffraction gratings are located in both beams to produce three-phase shifted interferograms. These beams are then combined and imaged directly onto the camera. The critical alignments in this system are the orientation of the diffraction gratings, the cubic beam splitter, the camera and the orientations of the object and the reference beams. The alignments are achieved by using cross correlation between the diffracted orders, and then the system was calibrated using a PZT phase shifting. The experiment reported by the authors consists of a study of the transient behaviour of a two-dimensional buoyant thermal plume at a maximum frame rate of 82 Hz.

An interferometer constructed with a pixelated phase mask aligned to a detector array is instead reported by James Wyant et al. [49, 50]. In spatial and temporal carrier phase shifting interferometry, the main source of phase calculation errors results from an error in the relative phase shift between sample points; in spatial carrier phase shifting interferometry these errors are caused directly by the wave front under test and are unavoidable. In order to reduce this error, this new type of spatial phase-shifting has been developed by 4D-Technology. The heart of the system lies in a pixelated phase mask where each pixel has a unique phase shift, so a small number of discrete steps can be arranged into a “unit cell” and this scheme is then repeated contiguously over the entire array. Figure 2.16 shows a unit cell in which four phase steps are comprised:

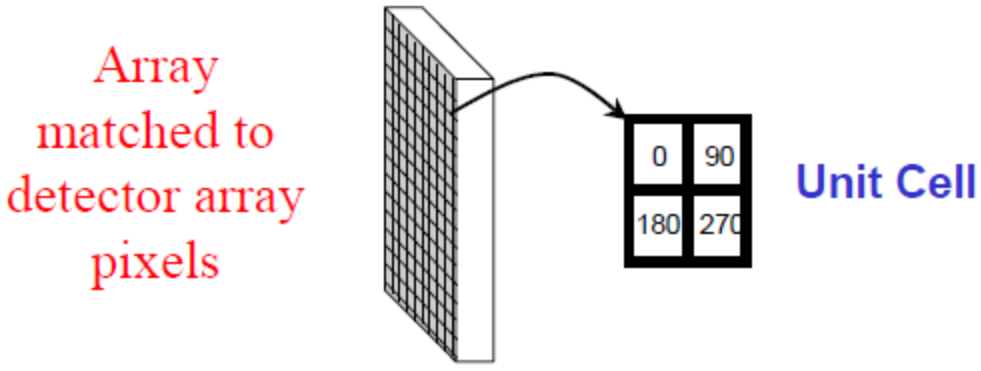

Fig. 2.16. Pixelated mask to align to detector array and single unit cell of the mask. [49]

The interferometer reported generates a reference wave front and a test wave front having orthogonal polarization states with respect to each other; the pixelated phase-mask

introduces a phase delay between the reference and test wave front at each pixel and subsequently interferes the transmitted light. The phase difference between the two beams is recovered using the N-bucket algorithm or by spatial convolution. The reported experiment uses this mask in a Twyman-Green interferometer and it has shown excellent repeatability and precision.

Millerd. [51] developed a polarization sensitive Twyman-Green interferometer, which used the above mentioned pixelated phase mask, to introduce spatial phase stepping.

Tao Wu et al. [35] have developed a high speed Sub-Nyquist spatial phase stepped SPI.

It is worth of mentioning what "Sub-Nyquist" means before their results are shown. The term Sub-Nyquist comes directly from the Sub-Nyquist theory of which Grievenkamp [34] gave the first concepts. He stated that, by using a priori information about the wavefront being measured, the aliased fringe pattern can be recovered within certain hypothesises. For example when we measure the phase of a wavefront, we calculate it as the arctangent whose argument is a function of the intensity at those points. The result of the arctangent is wrapped between 0 and 2π, so the wavefront then needs to be unwrapped adding the right multiple of 2π to recover it. The unwrapping is successful if the sensor is sampling the fringe pattern at a spatial frequency that is at least twice the highest spatial frequency in the pattern. This means that the maximum phase change that can be tolerated between any two adjacent pixels cannot overcome π, because otherwise the pattern will result under-sampled. This obviously limits the measurable wavefront slope to half a wave per pixel. The Grievenkamp's assumption to overcome these limitations is that, starting as usual from the aspheric surface continuity, also the surface derivatives were continuous. This supplementary assumption yields dramatic increases in the measurement range of the interferometer. Beyond this assumption, what is of greater interest in Grievenkamp's theory, is that the physical limitations of the Nyquist limit are merely due to the reconstruction algorithm and that there is no fundamental reason that prevents fringe frequencies greater than the Nyquist frequency of the sensor from being properly measured. Following this main concept but with a different technique, Servin[52] for example exceeded the Nyquist limit calculating the temporal phase variation by calculating the spatial phase gradient across the test surface.

Now refer to Tao Wu's system. The spatial phase stepped SPI system reported is based on a high speed CMOS camera and it uses a pair of binary gratings in order to obtain double channel sensing and a fixed phase step between the two channels (i.e the two diffracted images). A numerical and theoretical error analysis for the system was then

performed to demonstrate the increased dynamic range with respect to the temporal phase stepped system. The inter-frame phase stepped SPI model used for this analysis, calculates a 256x1 pixel fringe pattern using Equation 2.32

$$I_n(x, y, t_n) = I\left(1 + Vsinc\left[\frac{\Delta}{2}\right]cos[\Phi_o - \Phi_R]\right) \tag{2.32}$$

A composite spatio-temporal image is constructed by using the number of frames necessary to show two periods of the deformation, using a maximum surface velocity of $\frac{v_{max}}{|v_{Nq}|} = 0.2$ and applying a uniform phase step of $\Phi_R(t_n) = \frac{t_n}{t_s}\frac{\pi}{2}$. For this calibration a frame rate of 100 kHz is also used and an object vibration frequency of 1 kHz. The wrapped phase is calculated using the Carre´ algorithm. An equivalent simulation for spatial phase stepping is then undertaken; the intensity of N images, equally sampled on N separate regions of a single detectors or N separate detector, is calculated using the relation:

$$I_{n,N}(x, y, t_n) = I\left(1 + Vsinc\left[\frac{\Delta}{2}\right]cos[\Phi_o - \Phi_R]\right) \tag{2.33}$$

In this case, a constant phase step of $\Phi_R(t_n) = (1 - N)\frac{\pi}{2}$ is introduced between each image. Depending on the number, N, of images spatially recorded and shifted, different algorithms are used to obtain the argument of the cosine term in Equation (2.33). Figure 2.17 shows a simulation of the quoted spatial phase stepped SPI.

Simulations demonstrated that when a vibration frequency f=1 kHz and a time exposure t_s=10μs were used, unwrapping the velocity was successful for velocities up to ±15.9 V_{Nq} if the assumption of continuous surface velocity was considered. Higher velocities could be recovered if it was assumed that also the surface acceleration was continuous, leading to successful unwrapping of acceleration for velocities up to ±253 V_{Nq}.

The experimental system is shown in Figure 2.18. The binary gratings are designed with a phase modulation depth chosen to eliminate the even diffracted orders for the wavelength of the laser in order to obtain only the +1 and -1 orders and to suppress the 0 order. This enables the spatial resolution to be maximized for high speed detectors, since only two diffracted orders are imaged onto the sensor.

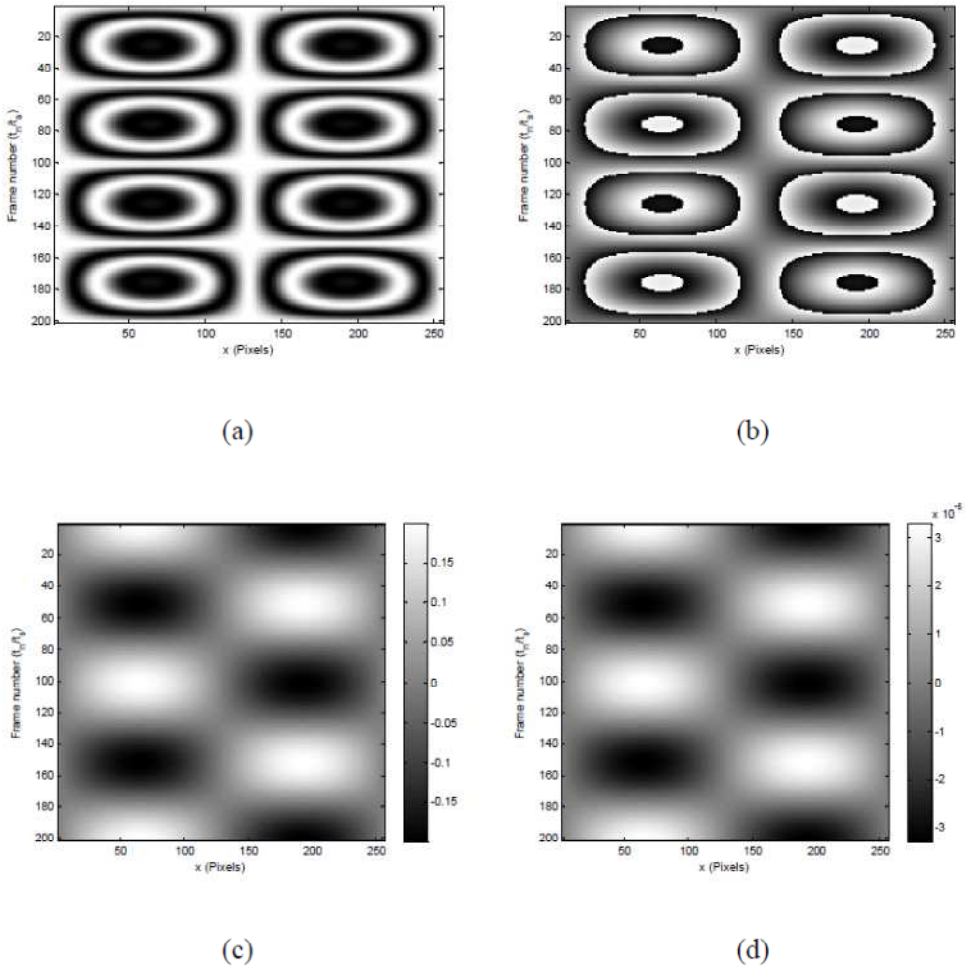

Fig. 2.17. N=4, vibration amplitude 0.2 V_{Nq}. (a) Intensity pattern, (b) Wrapped phase, (c) Normalized velocity, (d) error in normalized velocity. [35]

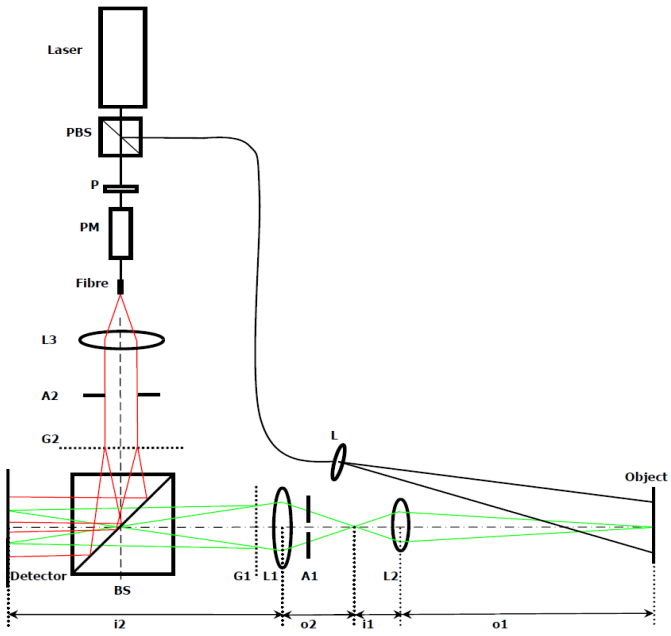

Fig. 2.18. Schematic of spatial phase stepped SPI setup. [35]

Time averaged fringes are previously recorded, from which a ROI, covering the two diffracted orders for spatial phase stepping, is indentified and then interrogated at 20,000 fps. The performance of this system is first compared to inter-frame phase stepping for low surface velocities, namely 0.5 V_{Nq}, and a difference of 0.1 V_{Nq} is observed mainly due to misalignment of the diffracted images. In order to reduce these errors a new single step algorithm is used enabling compensation. The inter-frame phase step fails at 0.3 V_{Nq} while the spatial phase stepping continues to work up to the Nyquist limit. The system has been tested successfully up to a surface velocity of 3.0 V_{Nq}; beyond this limit, that represents an order of magnitude improvement compared to the inter-frame phase stepped system, even the spatial phase stepping fails due to exposure that becomes the most important factor.

2.4.3 Fourier Transform based analysis

Usually, a sequence of speckle patterns is recorded to get the entire deformation history of the object as a function of time, and then each pixel is analyzed as a function of time. The intensity fluctuation that is due to deformation is first transformed, and one side of the spectrum is filtered with a band-pass filter. The filtered spectrum is then inverse transformed to yield the wrapped phase map. Finally the phase values are unwrapped along the time axis at each pixel independently of other pixels in the image. The fringe pattern is primed with carrier fringes in order to remove phase ambiguities. A frequency domain analysis for fringe patterns without carrier fringes has been proposed [53], although certain fringe forms lead to ambiguities in the recovered phase. A. Moore et al. [54, 55] proposed a method of phase calculation based on spatial (i.e. spatial domain version of the Fourier transform method) synchronous detection without the need for carrier fringes in the interferograms, but the technique was revealed to be analogous to the Fourier transform method (i.e. frequency domain of the Fourier transform method) without the use of fringe carrier. Loss of the sign of interference phase and phase reversal for non-monotonic phase distributions were the major drawbacks. Others authors [56] reported an interesting comparison of Fourier transform, windowed Fourier transform, and wavelet transform methods for phase extraction from a single fringe pattern in fringe projection profilometry, concluding that the main drawback of all transform-based algorithms is that they perform poorly around phase discontinuities. Pablo Ruiz et al. [57] proposed an

adaptive phase shifting algorithm for temporal phase evaluation that searches for the peak of the windowed Fourier transform (WFT) of the intensity signal and then evaluates the phase at that frequency instead of at carrier frequency.

2.4.4 Wavelet analysis

If we look carefully at the temporal intensity variation, described for example by Equation 2.32, of each pixel on the images recorded by a high speed CCD camera, it is possible to observe a frequency modulation introduced directly from the displacement itself; in fact the instantaneous phase change introduces a frequency shift of the intensity pixel signal. The main idea that is behind the wavelet analysis is to measure accurately this frequency shift so that transient velocity and displacement of each point can be retrieved without the necessity of the temporal or spatial phase unwrapping process. Xavier Colonna de Lega [40] has reported a detailed study about wavelet-based phase analysis. The need to measure the frequency shift that is possible to observe in the intensity pattern is the starting point; to catch this target the major interest is to analyze the signal as locally in the time as possible, that is the same to say that we should prefer to have an "instantaneous" spectrum. The standard tools should be the Windowed Fourier Transform and the Gabor Transform (Gaussian window) in which to the time localization corresponds frequency localization. So a large time window is used to explore the low frequency components of the signal and a narrow time window is used to explore the high frequency components of the signal; the drawback is that once the window dimension is chosen it remains the same for all the frequencies.

The wavelet analysis solves these problems by providing a bigger flexibility in the choice of window dimension. A wavelet decomposition of a given signal s(t) is performed through the use of a dilated and translated basic window function g(t), called the mother wavelet. The wavelet transform, in Equation (2.34), is then calculated for different values of the dilation parameter a, and the time translation b:

$$S(a,b) = \frac{1}{a}\int_{-\infty}^{+\infty} s(t)\,\bar{g}\left(\frac{t-b}{a}\right)dt \qquad (2.34)$$

Wavelet transform performs better in the low frequency domain at the expense of time localization, and vice versa. An example is given in Figure 2.19:

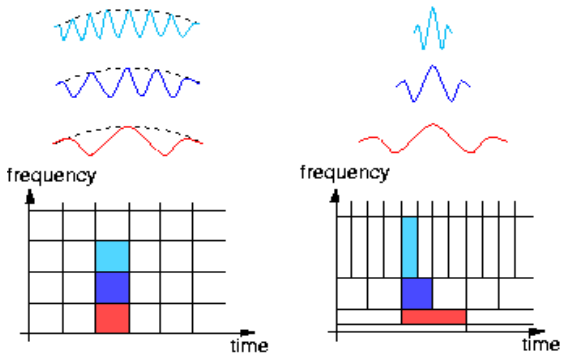

Fig. 2.19. Gabor transform time-frequency localization (left) and wavelet localization (right). [40]

As the wavelet is function of two variables, scale and time, it is usually presented as spectrogram like that shown in Figure 2.20:

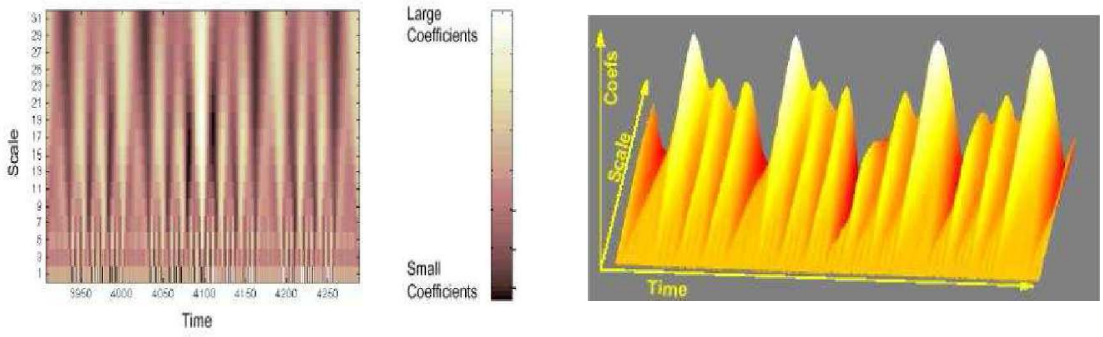

Fig. 2.20. Spectrogram (left) and corresponding 3-D image (right). [40]

Looking at the 3-D image, and considering that here the scale is the frequency, we obtain whole information about the behaviour of the signal in time –frequency domain. If now we suppose we dispose of a real signal s(t) of constant frequency and amplitude over the analysis window, then this corresponds to the linear phase evolution hypothesis in the case of phase shifting algorithm[40]:

$$s(t) = A + 2Bcos\Phi_s(t) = A + 2Bcos(\omega_s t) = A + Be^{i\omega_s t} + Be^{-i\omega_s t} \qquad (2.35)$$

The correspondent wavelet transform will be [40]:

$$S(a,b) = \frac{1}{\sqrt{2\pi}} A exp\left(-\frac{\omega_o^2}{2}\right) + \sqrt{2\pi} B exp(i\omega_s b) exp\left(-\frac{a^2}{2}\left(\omega_s - \frac{\omega_0}{a}\right)^2\right) + \sqrt{2\pi} B exp(-i\omega_s b) exp\left(-\frac{a^2}{2}\left(\omega_s + \frac{\omega_0}{a}\right)^2\right) \quad (2.36)$$

Now developing the expression of S(a,b) in the case in which only the positive frequency component of the signal is present in the analysis window and assuming the case of a constant amplitude monochromatic signal, Equation (2.36) becomes:

$$\mathrm{S(a,b)} = \sqrt{2\pi}\mathrm{B exp(i\omega_s b) exp}\left(-\frac{\mathrm{a}^2}{2}\left(\omega_\mathrm{s} - \frac{\omega_0}{\mathrm{a}}\right)^2\right) \quad (2.37)$$

In this situation the transform is exactly proportional to the signal contribution $\mathrm{B exp(i\omega_s b)}$. In the case of non-constant amplitude monochromatic signal the Equation (2.37) becomes more complicated so, in order to reduce the complexity of that form, we look its behaviour along the so called ridge of the transform, defined as the set of couples (a,b) in the time-frequency domain for which the analysis frequency is equal to the instantaneous frequency of the signal :

$$\omega = \frac{\omega_o}{a(b)} = \varphi_s'(b) \quad (2.38)$$

The resulting modulus and phase of the transform are slightly distorted version of the signal. Finally we can conclude that finding the ridge is equivalent to finding ωs and we don't need to integrate it to go back to the signal phase, since the transform implicitly yields φs. One attempt in extraction of the ridge of the transform could be to look for the maximum of S(a,b) modulus at each point b. But this could be time consuming. Another solution is the following: for constant frequency signals there is a band of analyzing frequencies centred on ωs for which the phase of the transform φs is equal to the phase of the signal. The width of this band depends on the width of the Gaussian window in the frequency domain.

Hence, when the analysis frequency $\omega = \frac{\omega_o}{\mathrm{a}}$ is close to ω_s, the rate of variation of the phase of the transform $\frac{\mathrm{d}\varphi_s}{\mathrm{db}}$, is actually equal to ω. Finding this frequency yields ω_s. In Figure 2.21 an example of ridge extraction and phase recovery is shown:

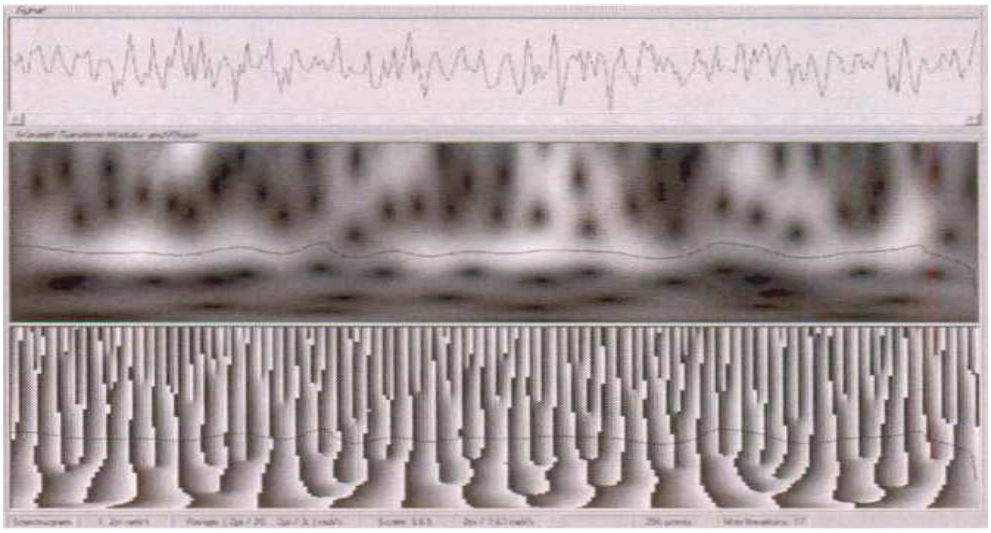

Fig. 2.21. Ridge extraction on the signal showed in the first line of the plot. Analysis performed at $\omega_o=2\pi$. [40]

The three limitations of the method are the following:

1. Difficulty in following very fast frequency variations;
2. Systematic phase errors appear when the phase evolution is not a linear function of time over the support of the temporal analysis window;
3. The ridge extraction becomes difficult when the signal gets close to the Nyquist limit.

Yu Fu et al. [58, 59] have reported other studies about the use of wavelet based method applied to SPI. Unlike Colonna de Lega's work, the phase is retrieved by integration and phase unwrapping in time, so the knowledge of its spatial domain is not required. After removing the temporal carrier an absolute displacement of the vibration is obtained. From these studies it is clear that wavelet analysis shows better results in displacement measurement of vibrating objects, since it calculates the optimized frequency at each instant performing like an adaptive band-pass filter of the signal and limiting the influence of random noise that is the main problem in Fourier methods. However, like in other temporal phase analysis methods, the temporal wavelet transform is limited by the Nyquist sampling theorem. Moreover it also requires the use of a carrier frequency that is not easy to introduce, and this carrier frequency should be high enough to ensure that the phase change in each point on the object is in one direction, but not too high in order to

prevent reducing the range of phase change that is possible to measure remaining within the Nyquist limits.

2.4.5 Empirical Mode Decomposition (EMD)

Sebastian Equis [60, 61, 62] proposed EMD to put the SI signal in an appropriate form for accurate phase computation. EMD's aim is to decompose any non stationary signal into its intrinsic oscillation mode, acting like a filtering process from higher to lower frequencies, but with self adaptive band filters. The signal is considered to be constituted by a detail part (high frequency) and a residue part (low frequency). The detail part is sifted out from the signal by removing the mean envelope, whose computation is based on a cubic fit between the signal extremes. The residue will then be split again into a detail and residue part, following a recursive process. The modes, namely the intrinsic mode functions (IMF), that could be non stationary too, have to satisfy two conditions:

1. In the whole date set the number of extremes and of the zeros has to be different at most by one.
2. The mean envelope is zero.

Considering a signal s(t) that represents the usual intensity pattern:

$$s(x,y,t) = \alpha(x,y,t) + \beta(x,y,t) \cdot cos\big(\psi_s(x,y,t) + \psi_{opd}(x,y,t)\big) \tag{2.39}$$

Its final decomposition at the rank K will be:

$$s(t) = \sum_{k=1}^{K} d_k(t) + m_k(t) \tag{2.40}$$

Where d_k and m_k are namely the IMFs and the final residue. The main two assets are that the signal decomposition has fewer components than with Fourier or wavelet analysis and that by design the algorithm ensures a lossless decomposition. The main drawback is the non uniqueness of the final decomposition. EMD outcomes depend strongly on sampling considerations and on the sifting process. With regard to the sampling considerations, it was demonstrated that a slight misalignment of the extremes with the sampling points

results in a wrong estimation of the amplitude and then in an over decomposition and mode leakage. The error is maximum when an extreme is equally spaced from two samples. On the other hand, the sifting process can influence EMD since bad choices of different parameters, like the sifting ending criterion, the boundaries ending technique andthe interpolation method, could lead to over decomposition or mixed modes. When a pixel signal has enough modulation, the relevant information is carried by the high frequency part of the signal (the cosine term). This information is thus contained in the first IMF and it is useless to proceed further in the modes, since the EMD is effective after one single iteration of the sifting process and the signal contains two well separated instantaneous frequencies. An analytic method is used for phase computation.

In order to extract the phase of a real valued signal, a complex signal can be built whose projection on real axis is the original signal. The Hilbert transform (HT) is the chosen operator to build the quadrature signal:

$$\varphi(t) = \arctan\left(\frac{-\mathrm{HT}[u(t)]}{u(t)}\right) \tag{2.41}$$

The phase is obtained by substituting for u(t) the first single iteration IMF of the signal and by computing the HT in the Fourier domain. “3D piecewise processing” [60] is then used to discard the areas where the pixel signal has a modulation lower than a certain threshold because, when the modulation drops to zero, the phase extraction becomes very inaccurate.

2.5 Alternative high-speed detectors

2.5.1 Smart detector array and Correlation Image Sensor

As we have already seen, when a high-speed phase stepping method is used to recover the deformation and the surface velocity of an object that is harmonically vibrating, the intensity recorded by the camera at pixel (x,y) during an exposure of duration t_s, centred at time t_n, can be approximated by:

$$I_n(x,y,t_n) = I\left(1 + Vsinc\left[\frac{2\pi\eta}{\lambda} w_n' \frac{t_e}{2}\right] cos\left[\psi + \frac{2\pi\eta w_o}{\lambda}\cos\left(\Omega t_n + \Phi\right)\right]\right) \qquad (2\text{-}42)$$

It is possible to see that the optical measurement is subject to a DC level of background intensity (i.e. I) which is higher than the level of the AC signal that we want to detect in order to calculate the parameters that are of interest. Here the background intensity is considered like a degrading term of the signal to noise ratio; on the other hand reducing the intensity of the two beams in order to reduce the background intensity is not a good idea since the visibility, V, is related to the beam intensities. Another topical problem arises when we try to improve the fringe visibility (i.e. $Vsinc\left(\frac{2\pi\eta}{\lambda} w_n' \frac{t_e}{2}\right)$) using a short time exposure, since by reducing the exposure time the number of photons incident on the camera is reduced; in this case the limits are imposed by the pixel sensitivity of the camera used.

Moreover, off-chip electrical or software processing is necessary to extract the information that is of interest from the FM modulated intensity pattern that is described by Equation (2-42). It is considered quite common in conventional speckle interferometry to have a trade-off among measurement time and spatial resolution, and demodulation accuracy and to find a good compromise among these factors is always a great issue.

In order to partially solve these problems, that don't belong only to SPI but even to other optical fields, great efforts were made in the development of cameras, with on- chip processing able to recover the different parameters that are of interest, directly at the pixel level.

Bourquin, Salathe´ et al. [63] developed a novel silicon detector chip that allows parallel heterodyne detection, suitable for Optical Low Coherence Reflectometry (OLCR) applications; OLCR is an interferometric technique based on broadband light source and coherent cross correlation detection of light. The standard method is based on Michaelson interferometers and sequential scanning of a single measurement point in transverse direction and in depth; since only one pixel per unit time is acquired the acquisition speed is strictly limited to 3-4 Hz. The arrangement, jointly to parallel detection of a transverse image with the customize array detector proposed by authors, is instead able to create cross-sectional images of 64x256 pixels acquired at video rate. The same authors [64], one year later, reported another CMOS detector for on-chip amplitude demodulation on all pixels in parallel. The CMOS detector has 58x58 pixels and it performs amplitude demodulation without signal sampling; the modulation amplitude was directly read out of

the sensor, one pixel after the other with no additional signal processing. The detector was able to detect optical signals at Doppler frequencies of 1 kHz up to 1 MHz, with a read-out up to 3 MHz enabling a full picture record rate of 890 Hz.

Since 2001, Shigeru Ando and Akira Kimachi [65], developed a correlation image sensor (CIS) which generated temporal correlation between incident light and an external reference signal at each pixel. These correlation image sensors were then used for the arrangement of a light-stripe range finding system. During the following years the same authors proposed applications method of this sensor to amplitude modulation-phase modulation demodulation imagers [66], correlation matching imagers[67] and real-time heterodyne imaging interferometry using a three phase correlation image sensor version (3PCIS) [68]. The last (i.e. in time order) arrangement that the authors proposed is a real time phase stamp range finder [69]. The system makes use of the 3PCIS, a scanning sheet of light (SOL) and the three phase reference signals supplied to the correlation image sensor. The system is shown in Figure 2.22:

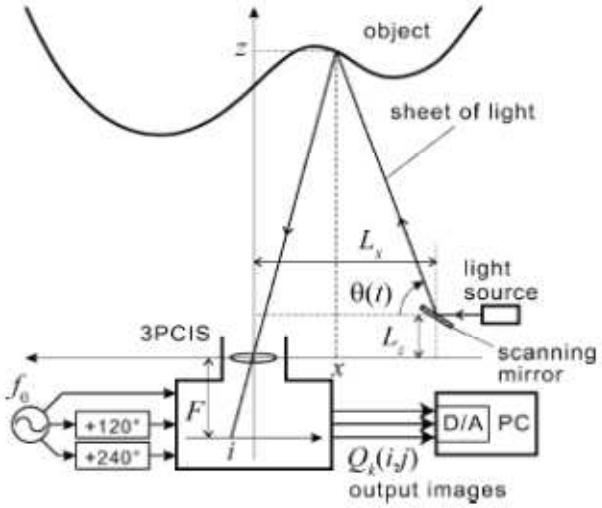

Fig. 2.22. Phase stamp range finder. [69]

The system employs the same imaging geometry as in the previous range finder [65]. However, here the sheet of light is not modulated, and the CIS records the "phase stamp" of the reference signals, which are equally phase shifted of $2\pi/3$, in the same instant in which the SOL reflected from the object is detected. So, the SOL is scanned over the object during the frame period, the CIS records the phase stamp of the reference signals only when the reflected SOL from the object is detected at each pixel, and finally the range image is reconstructed at the frame rate converting the phase stamp from CIS pixel

wise to the projection angle of the SOL. Triangulation is then applied. We can see from Figure 2.22 that the CIS has three inputs, that are the reference signals, and it produces three outputs that are the correlation images. So after a frame period T we obtain [69]:

$$\begin{bmatrix} Q_1(i,j) \\ Q_2(i,j) \\ Q_3(i,j) \end{bmatrix} = \begin{bmatrix} \Delta Q_1(i,j) \\ \Delta Q_2(i,j) \\ \Delta Q_3(i,j) \end{bmatrix} + \begin{bmatrix} \langle f_{i,j}(t)/3 \rangle \\ \langle f_{i,j}(t)/3 \rangle \\ \langle f_{i,j}(t)/3 \rangle \end{bmatrix} \tag{2.43}$$

$$\Delta Q_k(i,j) = \langle f_{i,j}(t) g_k(t) \rangle, \qquad k = 1,2,3$$

Where $\langle \cdot \rangle$ means time integral over the frame period T. The first term of the right hand side represents the temporal correlation between the incident light f and the reference signal g. So assuming that the reference signals are described by:

$$g_k(t) = \cos\left[2\pi f_o t + \frac{2}{3}\pi(k-1)\right] \tag{2.44}$$

and the light intensity by:

$$f_{ij}(t) = R_{ij}\left[A_{ij}\delta(t - t_{ij}) + B_{ij}(t)\right] \tag{2.45}$$

Equation (2.43) becomes

$$\begin{bmatrix} \Delta Q_1(i,j) \\ \Delta Q_2(i,j) \\ \Delta Q_3(i,j) \end{bmatrix} = R_{ij}A_{ij} \begin{bmatrix} \cos\psi_{ij} \\ \cos(\psi_{ij} + \frac{2}{3}\pi) \\ \cos(\psi_{ij} + \frac{4}{3}\pi) \end{bmatrix} + \begin{bmatrix} \varepsilon_1(i,j) \\ \varepsilon_2(i,j) \\ \varepsilon_3(i,j) \end{bmatrix} \tag{2.45}$$

Where $\psi_{ij} = 2\pi f_o t_{ij}$ is the phase of reference signal $g_1(t)$ at time t_{ij} and $\varepsilon_k(i,j)$ is a noise term. ψ_{ij} is the previously so called "phase stamp" at the time in which the SOL is detected at the (x,y) camera pixel. It is obtained from Equation (2.45) by least-squares estimation as:

$$\psi_{ij} = \tan^{-1}\frac{\sqrt{3}(\Delta Q_2 - \Delta Q_3)}{2\Delta Q_1 - \Delta Q_2 - \Delta Q_3} \tag{2.46}$$

A time chart of the system is showed in Figure 2.23:

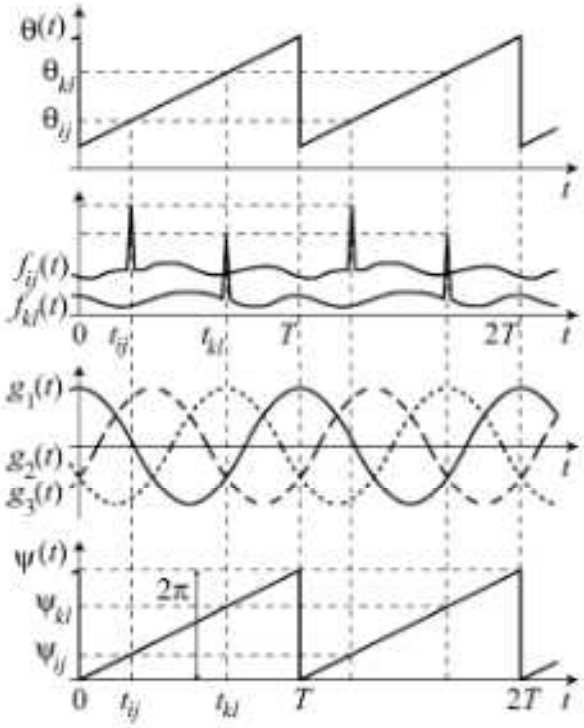

Fig. 2.23. Time chart of the system. [69]

The CIS used for the experimental setup has 200x200 pixels and its frame rate is equal to 12.5 frame/s; it can be increased by improving the digital scanning circuit on the CIS circuit board. The three phase shifted signals have a frequency of 50 Hz and their waveforms had been reversed in time in every period, in order to ensure that each pixel always accumulates the same temporal correlation value $\Delta Q_k(i,j)$ of phase stamp ψ_{ij} for the same projection angle θ of the SOL, four times in a single frame regardless of the scanning direction of the SOL. The timing relation between the projection angle, reference phase signals and phase stamp is shown in Figure 2.24:

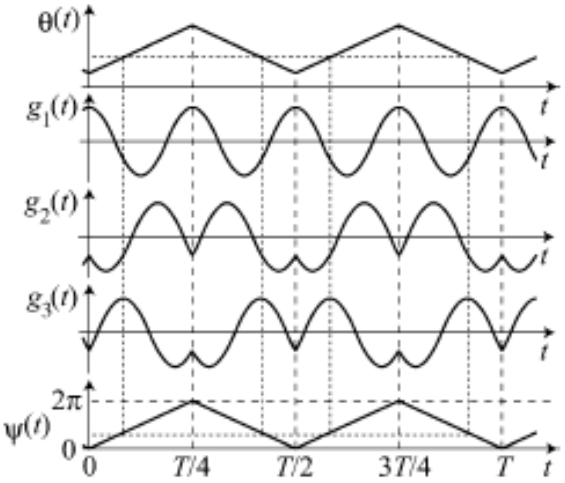

Fig. 2.24. Timing relation between the different parameters of the system. [69]

The experimental results reported demonstrate real-time imaging at 12.5 frame/s and measurement accuracy of less than 1mm in standard deviation for an imaging distance of 300-500 mm. The system is useful for 3-D imaging.

2.5.2 Detectors developed in Nottingham University

2.5.2.1 IQ demodulation scheme

Depending on the application requirement, the School of Electrical and Electronic Engineering, jointly with Applied Optics Group in Nottingham University, have developed different versions of Modulated Light Cameras (MLC) in recent years. The first work, reported in 2003 [70], describes a CMOS pixel with logarithmic response, designed to detect low modulated light depth (less than 0.5%) at a theoretical frequency of 25 MHz and tested at 1 MHz. The MLC pixel presented can be used to measure both amplitude and phase components in systems like heterodyne microscope scanning, by simply introducing a 90° phase shift in the reference generator. The behaviour of this pixel is that of a lock-in pixel, which is able to detect modulated light and to extract the phase and the amplitude. Basically, the output of the sensor is converted to a differential signal, amplified, and fed to a mixer where it is multiplied with a reference local oscillator

that enables a phase sensitive signal path. The unwanted components are removed from the signal spectrum by using a low pass filter.

Pitter et al. [71] fabricated later a modulated light camera for measuring thermo reflectance. This 4x4 pixel camera converts the incident light into a current and then a voltage in continuous time using a logarithmic front end. To perform the demodulation, the signal is amplified and band pass filtered and finally passed into two channels of a switched capacitor and integrating capacitor demodulator, where the different channels are for the I and Q phases. The circuitry for each pixel is shown in Figure 2.25, while in Figure 2.26 is shown the block diagram circuitry.

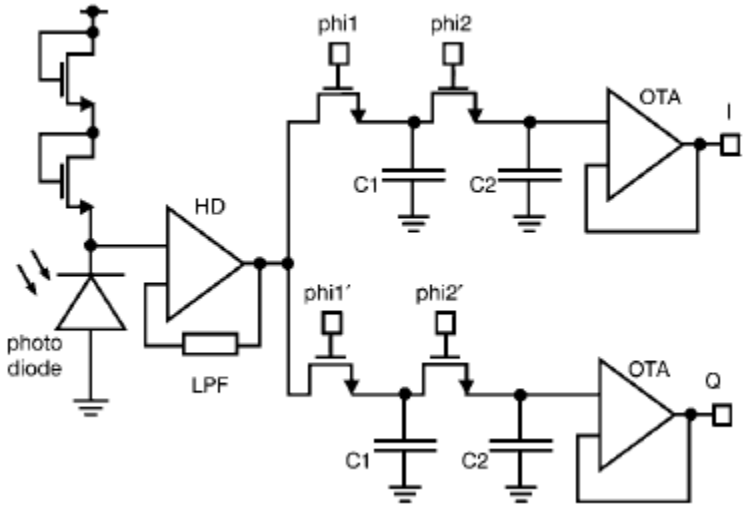

Fig. 2.25. Circuitry at pixel level. [71]

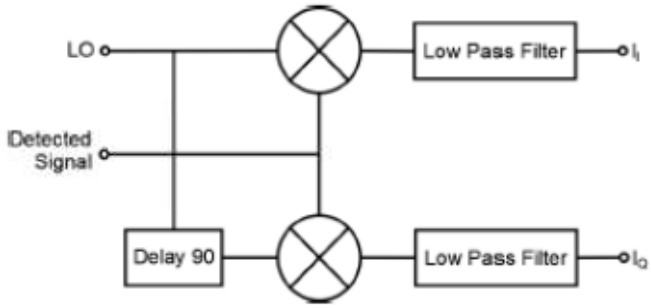

Fig. 2.26. Block diagram circuitry. [71]

Phase sensitive detection is performed by a simple IQ demodulator. The Q channel is identical to I channel except that the clock signals phi1' and phi2' are 90° out of phase with phi1 and phi2. The main disadvantage of the sensor is the low speed due to the mixer which doesn't use the whole signal waveform so that the integration is performed over all harmonics of the signal.

This prototype camera was, in 2004, followed up with a 64x64 pixel camera [72]. The design is much the same as the previous prototype except that the front end is slightly modified and the camera has a column based design rather than a pixel design. The dual-phase synchronous optical detection is performed in 64 independent channels and all the pixels in a single line may be processed in parallel. The camera has still a logarithmic response for large values of AC amplitude, which is responsible for distortion; this was dictated by the need for a continuous time output and a very large trans-impedance gain in a small area.

A differential ellipsometry technique with a waveguide mode and this kind of phase sensitive CMOS detector has been reported by Hooper et al. [73]. A UV induced refractive index change of a photo-resist wave guiding medium has been visualised, demonstrating that this CMOS detector is able to perform spatially resolved and differential measurements.

The last development of this modulated light camera performing demodulation with an IQ demodulator is reported [74]. This 64x64 pixel photodiode array differs from the previous modulated light camera described in that it measures not only the AC phase (logarithmically compressed) but also the DC level, and moreover it has a new quad-phase demodulation scheme which allows detection of signals hidden within even harmonics of large magnitude. The synchronous detection circuitry consists of 64 independent quad-phase processing channels that share clock and bias. The pixel response is still logarithmic. More details about the demodulation scheme are available in R.A. Light's PhD Thesis [75].

2.4.2.2 Phase stepping demodulation scheme

The sensor described here [76, 77, 78, 79] is a modulated light camera, which uses a different demodulation process with respect to the previous sensors reported. The technique used is the common phase stepping technique. The signal shown in Figure 2.27 is assumed to be

the signal recorded at the pixel detector when the input of the experiment is modulated, and the signal of interest is contained in either phase or amplitude depending on the experiment.

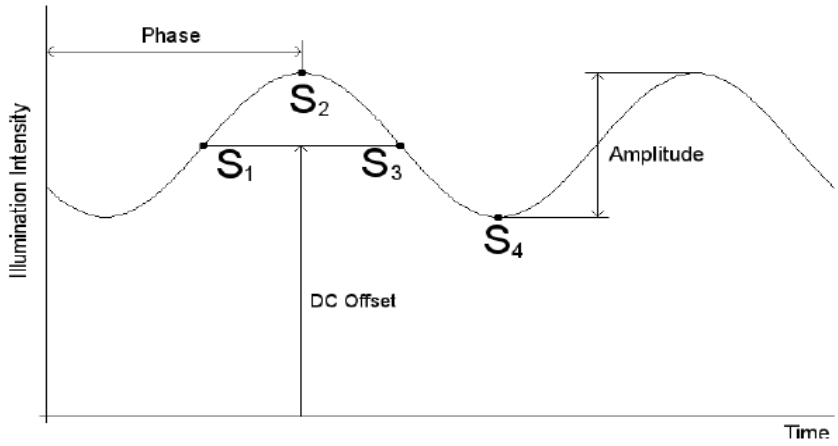

Fig. 2.27. Modulated intensity at pixel detector and sampling points taken by the system. [76]

The 4 samples are acquired at 90° intervals and they are sufficient to recover correctly the parameters of interest as follows [76]:

$$
\begin{aligned}
S_1 &= B + Asin(\phi + 0) = B + Asin(\phi) \\
S_2 &= B + Asin(\phi + 90) = B + Acos(\phi) \\
S_3 &= B + Asin(\phi + 180) = B - Asin(\phi) \\
S_4 &= B + Asin(\phi + 270) = B - Acos(\phi)
\end{aligned}
\tag{2.47}
$$

From these 4 samples is possible to recover the DC offset, amplitude and phase:

$$
\begin{aligned}
B &= \frac{S_1 + S_2 + S_3 + S_4}{4} \\
A &= \frac{\sqrt{(S_1 - S_3)^2 + (S_2 - 4)^2}}{2} \\
\phi &= tan^{-1}\left(\frac{S_3 - S_1}{S_2 - S_4}\right)
\end{aligned}
\tag{2.48}
$$

The lock-in behaviour is so simulated by acquiring four images evenly spaced in time throughout every modulation cycle. The sensor is a custom CMOS linear detector array with 1x256 pixels; it is provided with a field programmable gate array enabling logic

control and clocks and with an ADC under PC control. Each pixel has four capacitors and each capacitor can be considered as a channel having its own shutter switch that can either be operated independently or in tandem with others; the particular detector reported employs global shuttering, so all pixels are clocked in phase. This removes problems related to amplitude/phase cross talk that are typical in commercial arrays that normally use the simpler rolling shutter. Moreover, the particular active pixel design (APS) uses a linear response. So, thanks to this design the sensor is able to obtain four synchronous images before any data needs to be downloaded; this means that the sensor can lock-in frequencies well beyond the camera frame rate. The four channels in every pixel can be read in parallel since every channel has an own output amplifier operating at 10 MHz. This enables a maximum demodulated frame rate of just below 40 kHz. Each frame corresponds to one complete modulation cycle and it is related to the time necessary to acquire the data for all four phase steps for each of the 256 pixels. As the pixels are shuttered globally this is equal to four integration period (one per capacitor), that is 4 x 6.25μs. Another important advantage offered by this sensor is flexibility in its operation. When the camera is used like a modulated light camera there is a close relationship between the modulation frequency and the sampling frequency. If the system that we are using to sample is able to acquire 256 samples (i.e. number of pixels) within a quarter of the modulation period (since the first data are acquired and stored in the first channel after 90° from the starting point of the modulation period), then it is possible to simultaneously sample one channel whilst another channel is being exposed. Light it is not wasted in this way. However even assuming a low frequency of 10 kHz is used, this would require a sampling frequency of 10 MHz, which would be quite a stringent requirement for a commercial acquisition system. So if the acquisition speed is not enough to meet this demand then a different scheme may be used by taking the exposures for all four channels in order and only then carrying out the acquisition. This resolves the need of a too high sampling frequency but it waists more light, since the sampling is decoupled from exposure and we have to wait the download time for the four channels before restarting the sampling. The system described had been tested in the laser ultrasound imaging experiment shown in Figure 2.28; ultrasound detection is performed by using an ultra short probe beam pulse with a variable delay, in order to measure the slight change in the optical properties of the sample caused by reflected strain pulses as a function of time.

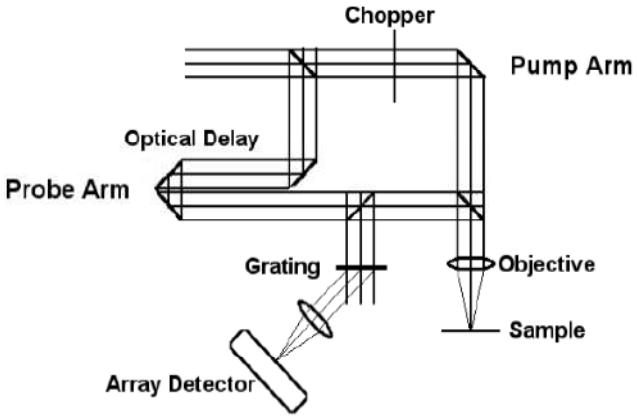

Fig. 2.28. Experimental arrangement for ultrasound detection. [76]

Different versions of this sensor have been employed in Doppler imaging experiments[80, 81], enabling full field laser Doppler blood flow imaging to be obtained at a frame rate in which effects due to motion artefacts are reduced. This represents a small step in Doppler imaging research field, in which, for example, the imaging of blood flow transient in inflammatory responses or of brain is still topical.

2.6 Summary

This chapter has reviewed the literature on full-field and multipoint optical techniques for vibration measurement. The time averaged method shows the typical advantage of optical techniques, namely non contact measurement, but it is restricted to measurement of harmonic deformations and it is not able to recover their phase. Pulsed techniques could theoretically be used even for transient deformation, but since it is necessary to synchronize the laser pulses to particular vibration phase they are more suited for harmonic deformation and for time average techniques. The advantage Pulsed techniques is that it is possible to recover also the phase of object deformation. High speed temporal phase stepping is the natural solution for measuring transient deformations, but the measurement range is restricted by Nyquist limit imposed on sampling the interference pattern. The spatial phase step overcomes this problem by introducing the phase stepping spatially rather than temporally and the range of surface velocity that can be measured is higher than with inter-frame phase step. Moreover, using it jointly with Sub-Nyquist interferometry enables dramatic increases of the range that is reliably measurable. The

other carrier based methods, as FT methods here reported, have the same limitations just discussed for inter-frame phase stepping, since the carrier reduces the measurable range. On the other hand not using the carrier means impossibility to recover the optical phase, due to object deformation, without ambiguity and loss of the sign of interference. Moreover it performs poorly around phase discontinuities as well as Wavelet analysis, which is also restricted to slow processes and it requires the use of a carrier frequency that is not easy to introduce. In EMD, when the modulation level is low, the phase extraction becomes very inaccurate and requirements about the position of the sampling points with respect to the maxima of the signal are stringent. The last part of the chapter described a new class of promising detectors; the capability to perform on-chip demodulation of the signal jointly with high phase sensitive detection represent a new chance to improve the temporal phase stepping technique results.

Chapter Three

Novel approach for vibration measurement

3.1 A custom CMOS detector

This chapter introduces the first new work reported in this thesis. The new CMOS detector is described and then its potential mode of operation in SPI is modelled and a numerical simulation is undertaken.

The detection system that we used in our project, consists of a custom CMOS detector array of 64x64 pixels (which works as a modulated light camera), a field programmable gate array, providing control of logic and clocks, and an analog-to-digital converter ADC, which has a depth of 12 bits and theoretical sampling rate equal to 25 MHz, under personal computer control. The pixel design is based on the standard four transistor active pixel sensor (APS), but each pixel has four large independently shuttered capacitors that drastically boost the well capacity from that of the diode alone. The novel pixel design is shown in Fig. 3.1.

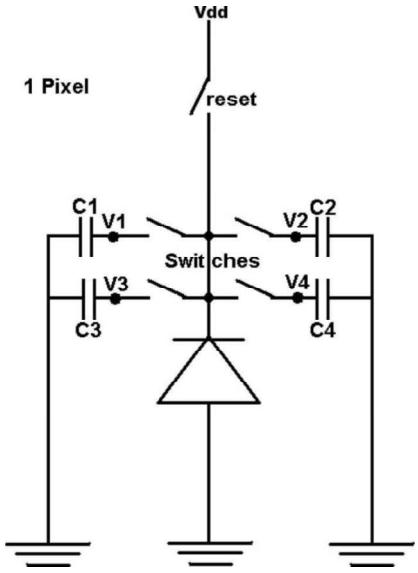

Fig. 3.1. Simplified pixel level schematic showing four independently switchable storage capacitors. [76]

Each capacitor represents a channel that has its own shutter switch and can either be operated independently or in tandem with others. In this project the detector employs global shuttering, since we need that all the pixels are clocked in phase to perform measurements of time-dependent deformations. Each channel also contains a reset switch. The pixels are randomly addressable, allowing the device to identify different ROIs.

The arrangement that makes the most efficient use of the available light should be to simultaneously sample one channel whilst another channel is being exposed; however, at the time when this partnership started, this solution was performed only for a linear array of 256x1 pixels [76]. For the model of detector we instead assume that the exposures for all of the four channels are taken in order and only then they are sampled at once. In other words, the channels are read in series rather than in parallel. The continual integration, reset, and readout all take place within one individual frame, which can be considered concluded only when the data for all four channels, for each of the 64x64 pixels, are acquired and sampled.

From this point on, we always refer to t_r as the reset time used to discharge every capacitor and to have it ready for a new exposure, t_e as the time exposure of every channel, t_s as the detector sampling period (i.e. the time that occurs between two adjacent array exposures), T_{Mod} as the time occurring to expose the four channels, T_{acq} as the detector frame period, and *Readout* as the time taken to acquire and sample all the channels. It is worthy of mention that a modulated light camera operates as a lock-in camera. Hence, the maximum detector sampling rate f_s is strictly related to the maximum frequency that the camera can lock-in. Once the frequency F_{Mod} to be locked-in is fixed, the detector generates four evenly spaced samples at a frequency $f_s = 4 * F_{Mod}$.The later readout takes the time necessary to acquire and sample all the channels for all the pixels; when this time is not an integer multiple of T_{Mod}, an extra time T_{ex} is waited in order to match this requirement, thus extending the readout time. Therefore the frame period is:

$$T_{acq} = T_{Mod} + readout = 4 * t_s + \frac{4 * X * Y}{F_c} + T_{ex} \quad (3.1)$$

where *X* and *Y* are the number of rows and columns of pixels respectively used, and F_c is the sampling frequency of the ADC board. An example of the frame structure is shown in Figure 3.1, where a frequency $F_{Mod} = 10\ kHz$ is locked-in by the detector. A sampling

frequency $f_s = 40\ kHz$, four time higher than the modulation frequency, is consequently generated, thus yielding an acquisition frame rate of 5,000 fps. The reset time is a fixed camera setting and it is equal to 500 ns.

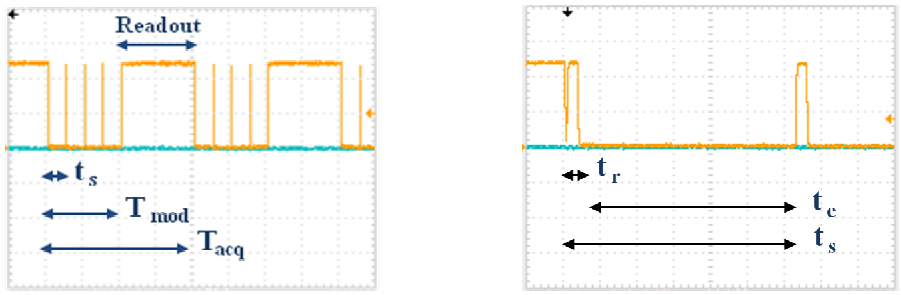

(a) (b)

Fig. 3.2 (a) Detector frame structure observed at oscilloscope and (b) zoom in.

As the camera has an effective sampling period equal to t_s, we can express the acquisition time of a single frame as:

$$T_{acq} = N_{acq} \cdot t_s \tag{3.2}$$

where N_{acq} is the integer multiple of t_s that is contained within one acquisition period. When the readout is negligible with respect to t_s, $N_{acq} = 4$; when the readout time is longer (e.g. in full field application) $N_{acq} > 4$.

A lower spatial resolution allows a higher temporal resolution as shown in Tab.3.1, where, although the camera could handle many different configurations, just the two of interest for this work are shown.

Region of interest size (Pixels)	Maximum F_{mod} camera can lock-in	Maximum Frame rate
64 x 64	200 kHz	1,000 fps
64x1	200 kHz	40,000 fps

Tab.3.1. Maximum camera frame rate and maximum frequency that the camera can lock-in for different sized regions of interest.

3.2 Theory of operation

For an interferometer using continuous-wave illumination, the interference intensity recorded by a detector at pixel (x, y) and at time t_n, integrated over the frame exposure t_s, can be written as [32]:

$$I_n(x, y, t_n) = I\left(1 + Vsinc\left[\frac{\Delta}{2}\right]\cos[\Phi_o - \Phi_R]\right) \tag{3.3}$$

where $I(x, y)$ is the bias intensity and $V(x, y)$ is the visibility of the interference, which depends on the relative intensity of the two beams, the state of polarization and their coherence, and the state of polarization. For a short $t_e$with respect to the vibration period, the object deformation resolved in the observation direction, $w_n(x, y, t_n)$, can be approximated by a linear expansion, i.e. the velocity $w_n^{'}$ is assumed to be constant. The instantaneous visibility, $Vsinc\left[\frac{\Delta}{2}\right]$, depends on the relative phase change between the object and reference beams during the exposure, $\Delta = (2\pi\eta/\lambda)\frac{w_n^{'}}{t_e}$. For maximum fringe visibility to be achieved, the argument of the *sinc* function should approach zero, thus requiring a low test surface velocity and a short exposure time. The object phase, $\Phi_o(x, y, t_n)$, comprises the phase due to the deformation of the target, $(2\pi\eta/\lambda)w_n^{'}$, and the random speckle phase in a speckle interferometer.

For temporal phase stepping, the reference phase, $\Phi_R(t_n)$, includes a phase-step increment with respect to the previous frame of $2\pi n/N$, where N is the number of steps per period. For *N=4*, the interference phase at each pixel (x, y) can be recovered from four consecutive images by Carré's algorithm [33]:

$$\Phi_o(t_n) - \Phi_R(t_n) = \tan^{-1}\frac{\sqrt{[3(I_n - I_{n+1}) - (I_{n-1} - I_{n+2})][(I_{n-1} - I_{n+1}) + (I_{n-1} - I_{n+2})]}}{(I_n + I_{n+1}) - (I_{n-1} + I_{n+2})} \tag{3.4}$$

It is assumed that the frame rate is sufficiently high that the velocity is approximately constant during four consecutive frames so that the phase at a given pixel can be calculated from I_{n-1} to I_{n+2}. As the camera takes sets of four samples evenly spaced by a long readout time, the hypothesis of constant velocity during four consecutive images is fulfilled if we use the Carré's algorithm to process groups of four images rather than

processing the images sequentially. With this processing strategy we recover one interference phase value from Equation 3.4 every set of four images; each set is recorded at a frequency, f_s, high enough to fulfil the requirement of approximately constant velocity during the period T_{Mod} required to take the four images.

When the data include some known or stationary reference, recovery of the absolute spatiotemporal profile from the phase $\Phi_o(t_n)$, is possible. For the general case of continuous motion with unknown initial deformation, the phase difference between adjacent frames is wrapped into the range –π to π radians and the surface velocity can be recovered from the relation:

$$w_n'(x,y,t_n) = \frac{\lambda}{2\pi\eta t_{acq}}\Delta\Phi_o(x,y,t_n)$$

$$or \qquad (3.5)$$

$$\frac{w_n'(x,y,t_n)}{V_{Nq}} = \frac{\Delta\Phi_o(x,y,t_n)}{\pi}$$

where at a given pixel $\Delta\Phi_o(t_n) = \Phi_o(t_n) - \Phi_o(t_{n-1})$ represents the change in phase due to the deformation between frames. The Nyquist condition imposes a maximum phase change of ±π in $\Phi_o$between any two frames, thus restricting the number of samples that can be skipped during the readout time between any two adjacent frames. Unwrapping the phase fails when the phase difference between adjacent measurements exceed π, meaning that the surface velocity limits N_{acq}:

$$w' = \frac{\lambda}{2\pi\eta}\frac{\Delta\Phi_o}{T_{acq}} \leq \pi \qquad (3.6)$$

Rearranging Equation 3.6 yields to:

$$N_{acq} \leq \frac{1}{w'/V_{Nq}} \qquad (3.7)$$

If the hypothesis of continuous surface velocity is assumed, a higher effective value of N_{acq} , than that described by Equation 3.7, can be used to unwrap the velocity.

Unwrapping velocity will fail when the normalized velocity difference between adjacent measurements exceeds π, meaning that the surface acceleration also limits N_{acq}:

$$w'' = \frac{\lambda}{2\pi\eta}\frac{\Delta^2\Phi_o}{T_{acq}^2} \leq \pi \tag{3.8}$$

, that yields to:

$$N_{acq}^2 \leq \frac{1}{w''/\left(V_{Nq}/t_s\right)} \tag{3.9}$$

For harmonic vibration Equation 3.9 can be rewritten as:

$$N_{acq}^2 \leq \frac{1}{2\pi f t_s/\left(w'/V_{Nq}\right)} \tag{3.10}$$

This approach doesn't lead to any increase in the maximum surface velocity limit that can be reliably measured, but it increases the system data transfer rate. In order to demonstrate it, let us assume a fixed data transfer rate (pixels/sec) for camera technology (typically 20 Mpixel/s). We can define an "equivalent frame rate" as the camera frame rate corresponding to V_{Nq}:

$$f_s = \frac{2\eta}{\lambda}V_{Nq} \tag{3.11}$$

The analysis of the performances of a standard system (i.e. using a standard detector and a standard data processing) and our system, both measuring a surface velocity $V = 0.3V_{Nq}$, with the same sampling frequency f_s and the same number of pixels, yields the results shown in Tab.2. When $N_{acq} = 4$, the two systems exhibit equal performances and no gain in data transfer rate is obtained; when $N_{acq} > 4$, depending on the effective number of samples that are skipped between any two frames, a gain in data transfer arises. Since N_{acq} is limited by the surface velocity, the lower is the maximum velocity we measure the higher the data transfer gain. For the case reported in Tab. 3.2, a sampling frequency $f_s = 100\,kHz$ and 4096 pixels are assumed; according to Equation 3.7, the phase unwrapping fails when $N_{acq} > 4$, not yielding any gain in data transfer rate. When

continuous surface velocity is assumed the measurement range is increased to $N_{acq} < 7.3$ (as described by Equation 3.10), thus enabling an increase in data transfer rate equal to 1.77 times the data transfer rate of a standard system.

	Velocity limit	Equivalent frame rate	Pixels	Data transfer rate	Data transfer rate / $f_s P$
Standard system	$0.3V_{Nq}$	$0.3f_s$	P	$0.3f_s P$	0.3
Our system	$0.3V_{Nq}$	$0.3f_s$	$P\frac{N_{acq}}{N}$	$0.3f_s P\frac{N_{acq}}{N}$	0.3
Continuous velocity	$0.3V_{Nq}$	$0.3f_s$	$P\frac{N_{acq}}{N}$	$0.3f_s P\frac{N_{acq}}{N}$	0.53

Tab. 3.2. Data transfer rate increase in our system compared to a standard system operating in identical experimental conditions. N_{acq} has increased because of the assumption of continuous surface velocity.

3.3 Simulation of the inter-frame phase stepped system

The data transfer increase achieved with our approach, is strictly related to the number of samples N_{acq} that can be skipped during the readout between any two adjacent frames; the higher the N_{acq}, the higher the increase in data transfer rate. On the other hand N_{acq} cannot be arbitrarily large, as it is limited by the surface velocity and surface acceleration accordingly to Equation 3.7 and Equation 3.10, which are repeated for simplicity:

$$N_{acq} \leq \frac{1}{w'/V_{Nq}} \tag{3.7}$$

$$N_{acq}^2 \leq \frac{1}{2\pi f t_s/\left(w'/V_{Nq}\right)} \tag{3.10}$$

In order to validate the theory of our approach, a simulation model was developed. A 64x64 pixels camera having a frame rate equal to 100,000 fps and a test object

harmonically vibrating at a natural frequency of 250 Hz are assumed. If a surface velocity $V = 0.1V_{Nq}$ is considered, Equation 3.7 restricts N_{acq} to:

$$N_{acq} \leq 10 \tag{3.11}$$

Figure 3.3 shows a composite spatio-temporal phase-stepped speckle interferogram, where each row corresponds to a single frame of 64x1 pixels interrogated at 100 kHz and $N_{acq} = 4$. The test object vibrates with a velocity $V = 0.1V_{Nq}$.

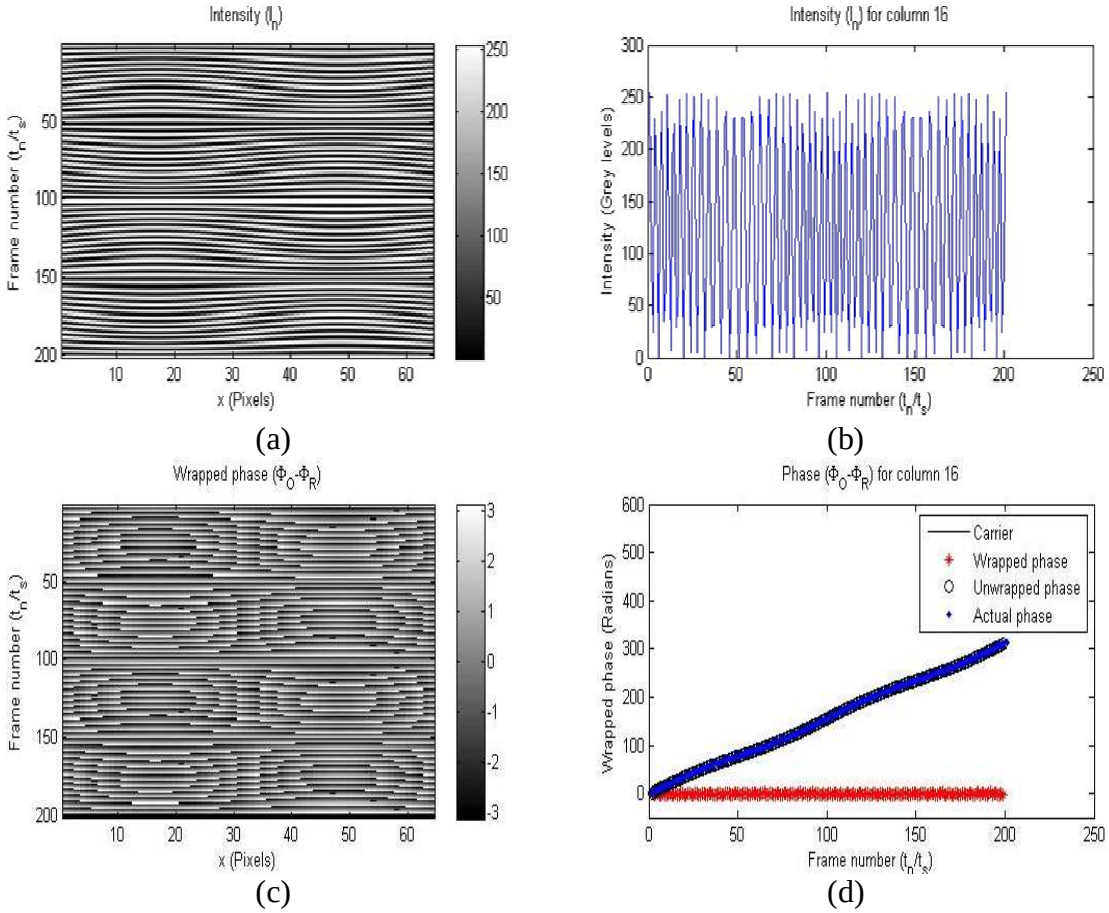

Fig. 3.3 (a) Simulation of a spatio-temporal speckle pattern showing the intensity variation for a horizontal ROI (64×1 pixels) recorded at 100 kHz and N_{acq}=4, for an object vibrating harmonically at 250 Hz and V=0.1V_{Nq} .(b) Intensity variation for column 16. (c) Wrapped phase for the ROI and (d) comparison between the carrier (i.e. phase step applied), wrapped phase and unwrapped phase for column 16.

The wrapped phase at each pixel is retrieved from the recorded intensity from four consecutive frames using Equation 3.4. The black intervals are due to the processing strategy, which marks as NaN the N_{acq} samples skipped in every frame.

The unwrapped phase is compared with the actual phase and, accordingly to Equation 3.8, unwrapping the phase is successful as shown in figure 3.3 (d). The phase values wrapped in the range of [-π, +π] and the carrier (i.e. the phase step applied at each frame) are also shown.

Unwrapping the phase is also successful when $N_{acq} = 10$ is assumed, as shown in Figure 3.4. In the continuation of this paragraph the number of pixels, camera frame rate and test object vibration frequency will be assumed constant.

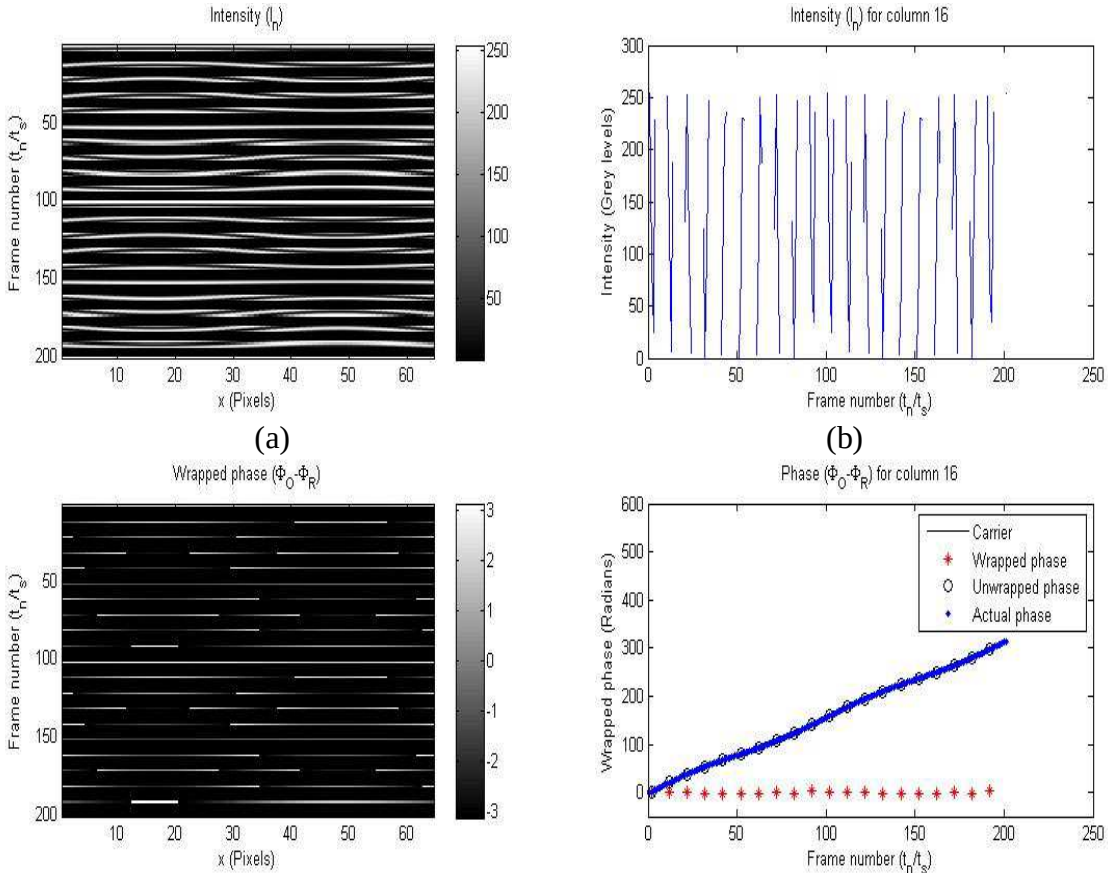

Fig. 3.4 (a) Simulation of a spatio-temporal speckle pattern showing the intensity variation for a horizontal ROI (64×1 pixels) recorded at 100 kHz and N_{acq}=10, for an object vibrating harmonically at 250 Hz and V=0.1V_{Nq} .(b) Intensity variation for column 16. (c) Wrapped phase for the ROI and (d) comparison between the carrier (i.e. phase step applied), wrapped phase and unwrapped phase for column 16.

Unwrapping the phase fails when $N_{acq} = 11$, as predicted by Equation 3.8, meaning that the phase difference between adjacent measurements exceed π. Figure 3.5 shows the simulation of case $N_{acq} = 11$, which perfectly agrees with restrictions imposed by Equation 3.7.

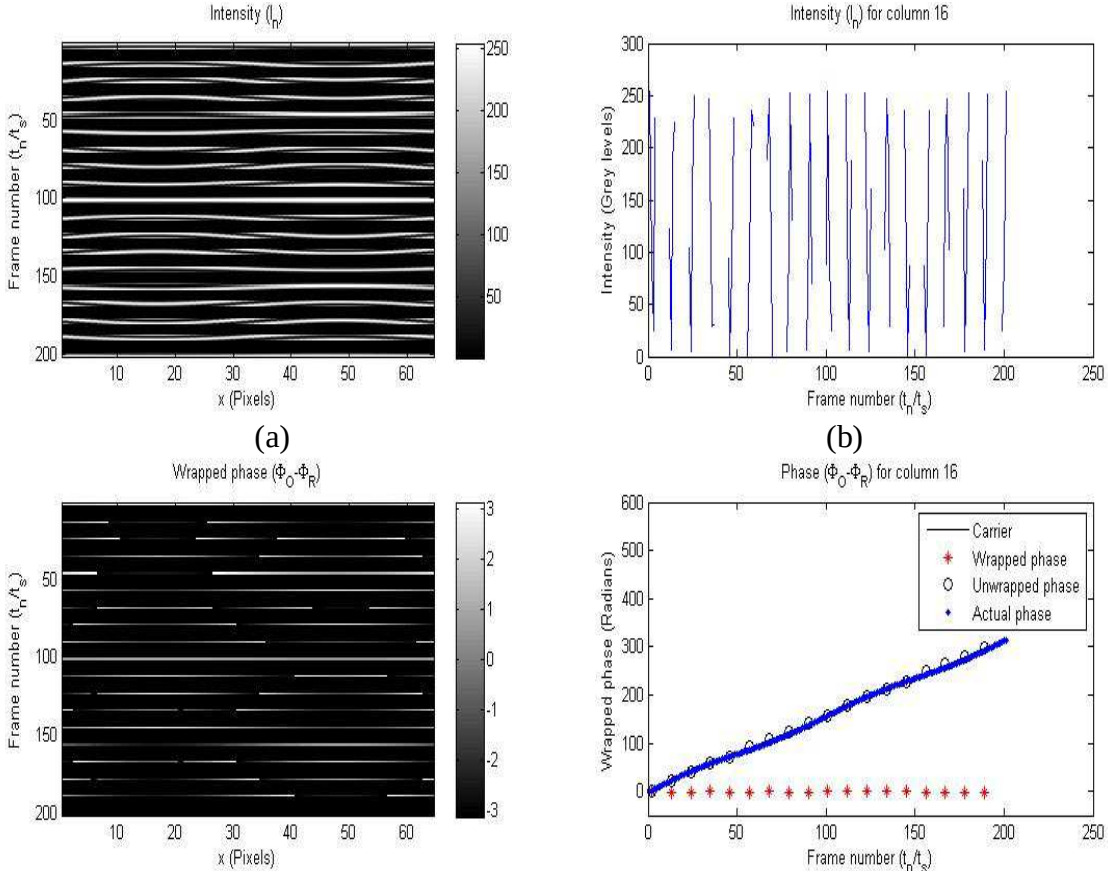

Fig. 3.5 (a) Simulation of a spatio-temporal speckle pattern showing the intensity variation for a horizontal ROI (64×1 pixels) recorded at 100 kHz and N_{acq}=11, for an object vibrating harmonically at 250 Hz and V=0.1V_{Nq} .(b) Intensity variation for column 16. (c) Wrapped phase for the ROI and (d) comparison between the carrier (i.e. phase step applied), wrapped phase and unwrapped phase for column 16.

Figure 3.6 shows an enlarged version of the different cases mentioned so far, thus enabling a clearer understanding. Figures 3.6 (a) and (b) show how the unwrapped phase retrieved by the Carré algorithm, matches perfectly the actual phase value, whereas Figure 3.6 (c) shows an error in unwrapping the phase, that is not a simple systemic offset which could otherwise be ignored.

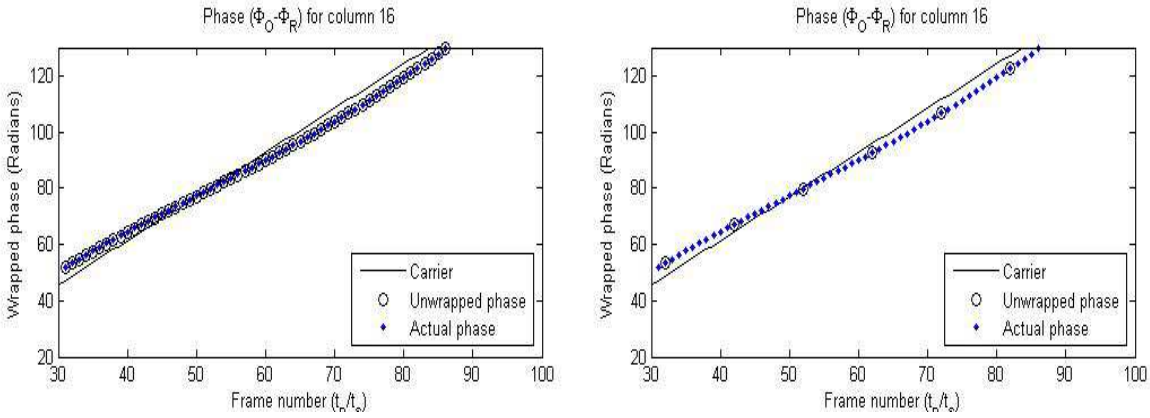

(a) (b)

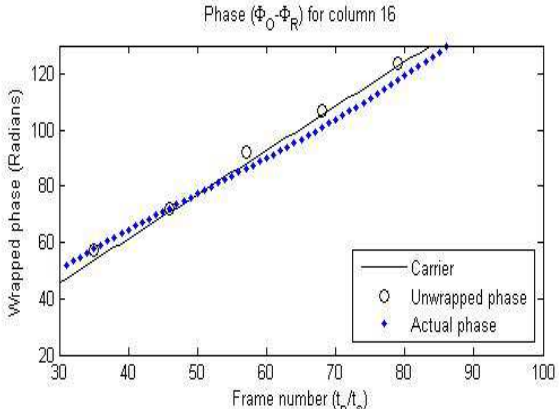

(c)

Fig. 3.6. (a) Unwrapping the phase is successful when N_{acq}=4 and (b) N_{acq}=10. It fails when N_{acq}=11 (c).

In order to test the system at different velocities, a vibration velocity $V = 0.2V_{Nq}$ is also considered. The higher velocity reduces the N_{acq} number of samples that might be skipped without errors in unwrapping the phase, and accordingly to Equation 3.7, it has to be:

$$N_{acq} \leq 5 \tag{3.12}$$

Hence if $N_{acq} = 5$ is assumed, unwrapping the phase is successful as shown in Figure 3.7 and 3.8 (an offset between the unwrapped phase and the actual phase arises, but since it is constant it can be considered acceptable), whereas if $N_{acq} = 6$, unwrapping the phase fails as shown in Figure 3.9 and 3.10.

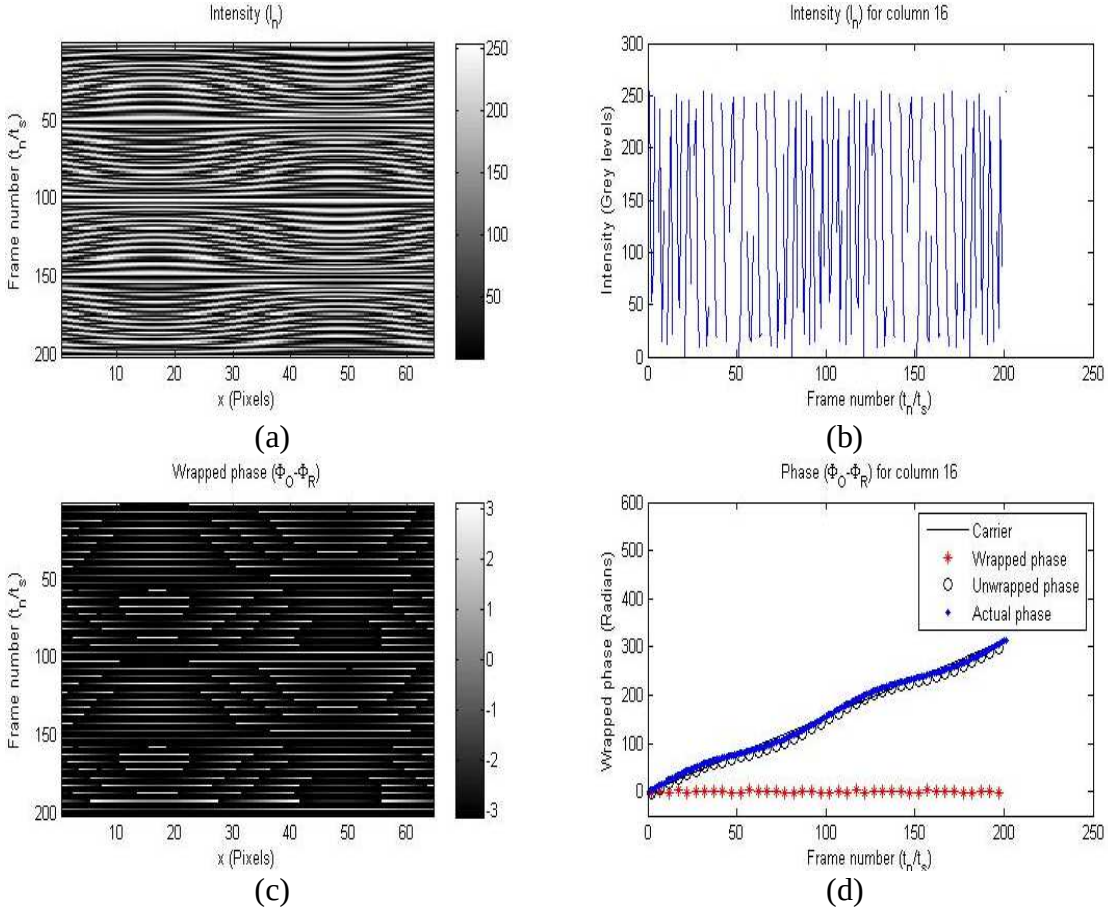

Fig. 3.7 (a) Simulation of a spatio-temporal speckle pattern showing the intensity variation for a horizontal ROI (64×1 pixels) recorded at 100 kHz and N_{acq}=5, for an object vibrating harmonically at 250 Hz and V=0.2V_{Nq} .(b) Intensity variation for column 16. (c) Wrapped phase for the ROI and (d) comparison between the carrier (i.e. phase step applied), wrapped phase, unwrapped phase and actual phase for column 16.

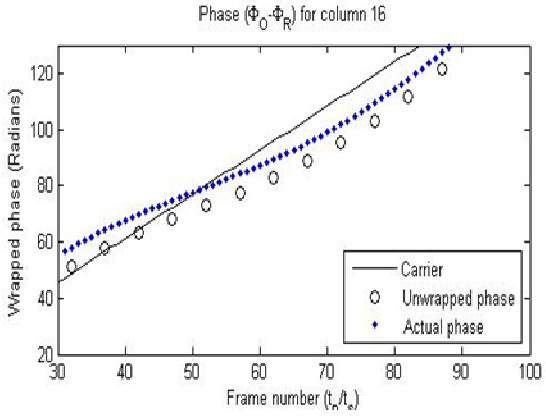

Fig. 3.8. Enlarged version of Figure 3.7 (d) showing the successful unwrapping of the phase compared with the actual phase.

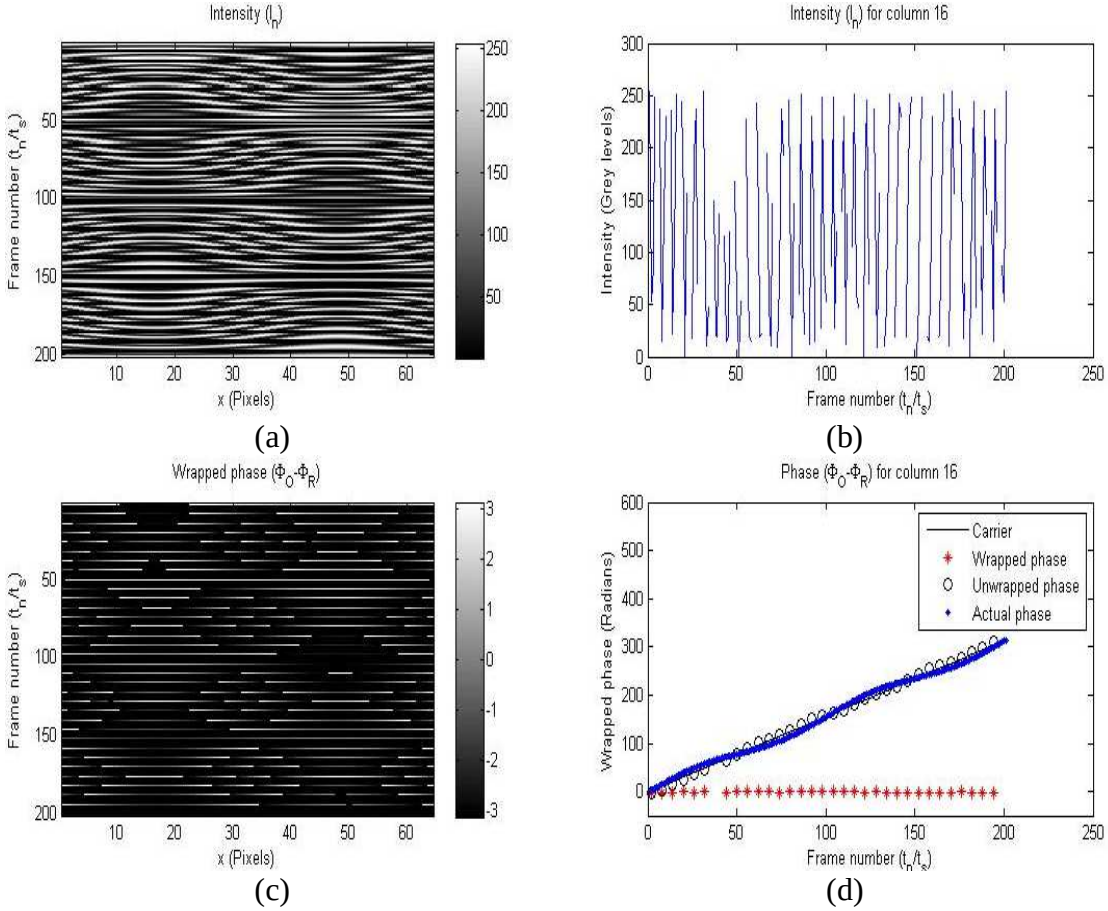

Fig. 3.9 (a) Simulation of a spatio-temporal speckle pattern showing the intensity variation for a horizontal ROI (64×1 pixels) recorded at 100 kHz and N_{acq}=6, for an object vibrating harmonically at 250 Hz and V=0.2V_{Nq} .(b) Intensity variation for column 16. (c) Wrapped phase for the ROI and (d) comparison between the carrier (i.e. phase step applied), wrapped phase, unwrapped phase and actual phase for column 16.

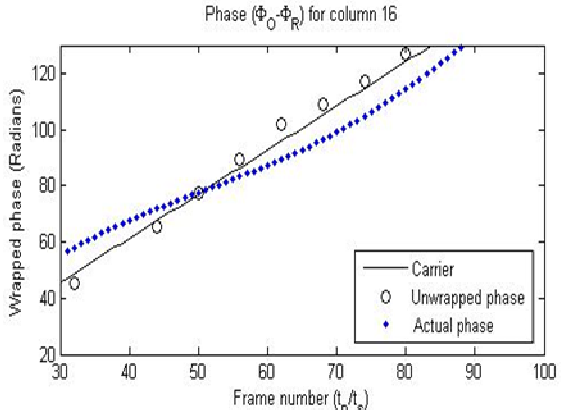

Fig. 3.10. Enlarged version of Figure 3.9 (d) showing the error in unwrapping the phase with respect to the actual phase.

Finally a velocity of vibration $V = 0.3V_{Nq}$ is considered. Equation 3.7 further reduces the N_{acq} number of samples that might be skipped without errors in unwrapping the phase, yielding to:

$$N_{acq} \leq 3.3 \tag{3.13}$$

Consequently, the assumption of $N_{acq} = 4$ causes errors in unwrapping the phase as shown in Figure 3.11 and 3.12.

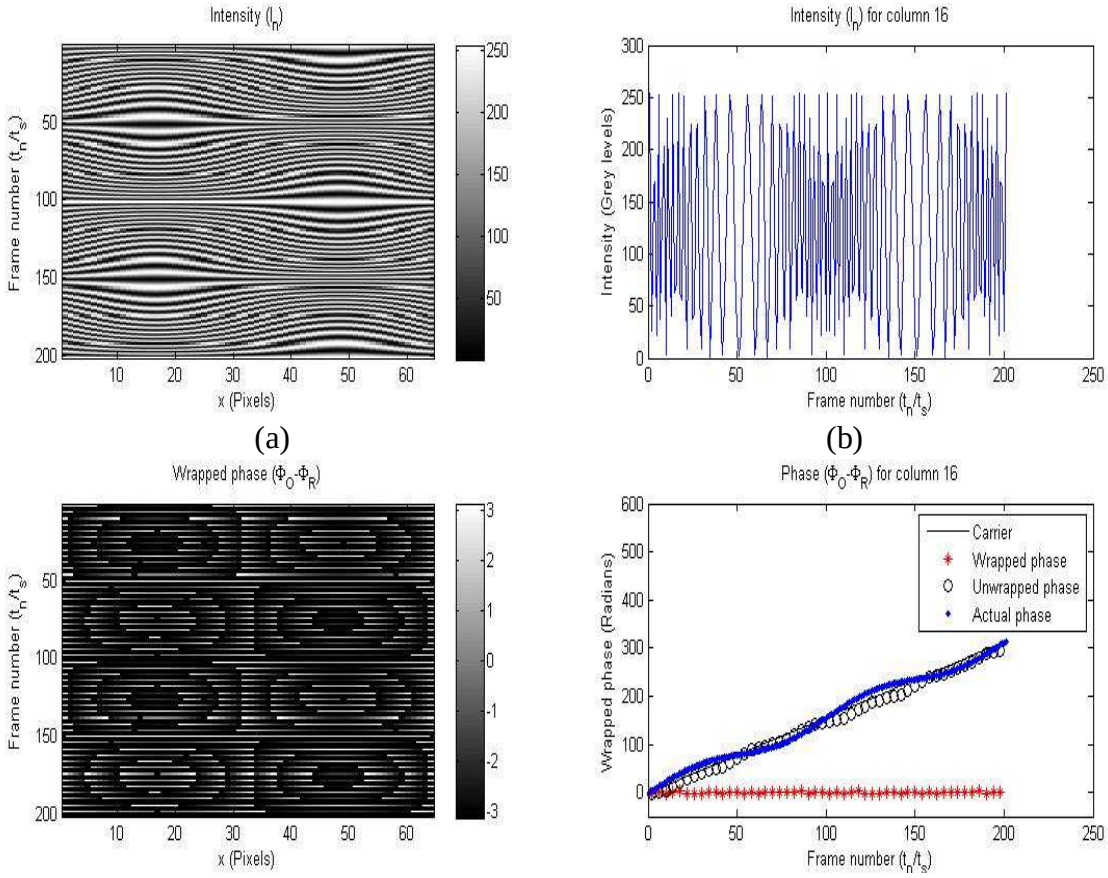

Fig. 3.11 (a) Simulation of a spatio-temporal speckle pattern showing the intensity variation for a horizontal ROI (64×1 pixels) recorded at 100 kHz and N_{acq}=4, for an object vibrating harmonically at 250 Hz and V=0.3V_{Nq} .(b) Intensity variation for column 16. (c) Wrapped phase for the ROI and (d) comparison between the carrier (i.e. phase step applied), wrapped phase, unwrapped phase and actual phase for column 16.

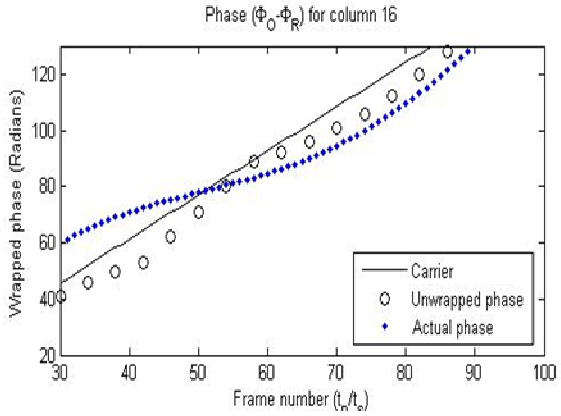

Fig. 3.12. Enlarged version of Figure 3.11 (d) showing the error in unwrapping the phase with respect to the actual phase.

These simulations validate the restrictions imposed to N_{acq} by the Nyquist condition, which limits the maximum phase change between any two frames to ±π, accordingly with Equation 3.7. Tab. 3.3 summarizes the simulation results so far shown.

Velocity	Theoretical Limit	Simulated Successful Unwrapping	Simulated Failed Unwrapping
$0.1V_{Nq}$	$N_{acq} \leq 10$	$N_{acq} = 10$	$N_{acq} = 11$
$0.2V_{Nq}$	$N_{acq} \leq 5$	$N_{acq} = 5$	$N_{acq} = 6$
$0.3V_{Nq}$	$N_{acq} \leq 3.3$	-	$N_{acq} = 4$

Tab. 3.3. Summary of the previous simulations. A comparison between the theoretical prediction of the maximum N_{acq} value and the maximum simulated N_{acq} value is shown.

A higher value of N_{acq} than that described by Equation 3.7 can be used to unwrap the velocity, if the hypothesis of continuous surface velocity is assumed. This additional hypothesis enables the correct reconstruction of the unwrapped surface velocity that would be otherwise sub-sampled.

When a vibration velocity of $V = 0.1V_{Nq}$ is assumed, the previous theoretical limit of $N_{acq} \leq 10$ stated by Equation 3.11, can be extended allowing for a correct unwrapping of the surface velocity.

Figure 3.13 shows a composite spatio-temporal graph of the retrieved normalized velocity compared to the theoretical normalized velocity, when $V = 0.1V_{Nq}$ and $N_{acq} = 13$ are assumed.

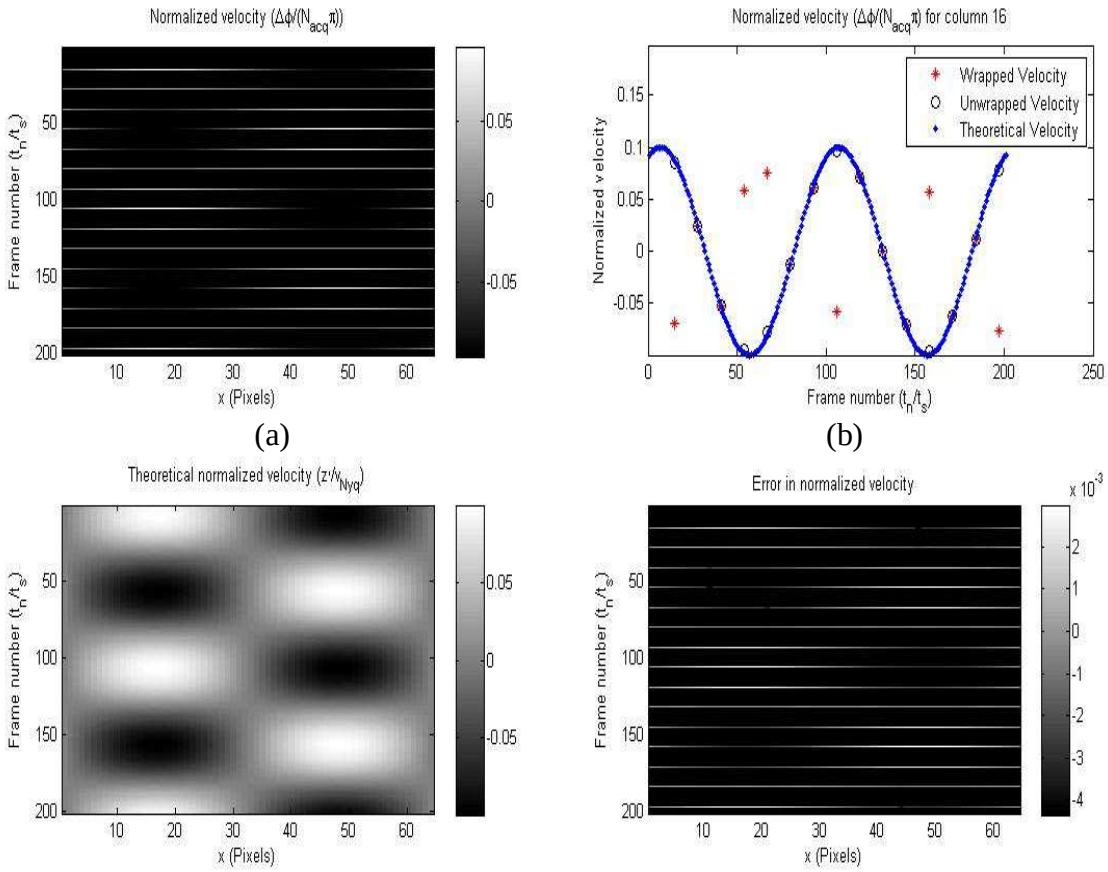

Fig. 3.13 (a) Normalized velocity $\Delta\Phi/(N_{acq}\pi)$ for a horizontal ROI (64×1 pixels) recorded at 100 kHz and N_{acq}=13, for an object vibrating harmonically at 250 Hz and V=0.1V_{Nq} .(b) Wrapped velocity, unwrapped velocity and theoretical velocity for column 16. (c) Theoretical normalized velocity for the horizontal ROI and (d) error in retrieved normalized velocity for the horizontal ROI.

Unwrapping the velocity fails when $N_{acq} = 14$ is assumed as shown in Figure 3.14. In fact the surface acceleration also restricts the number of samples that might be skipped and accordingly with Equation 3.10 this leads to:

$$N_{acq} \leq 13.6 \qquad (3.13)$$

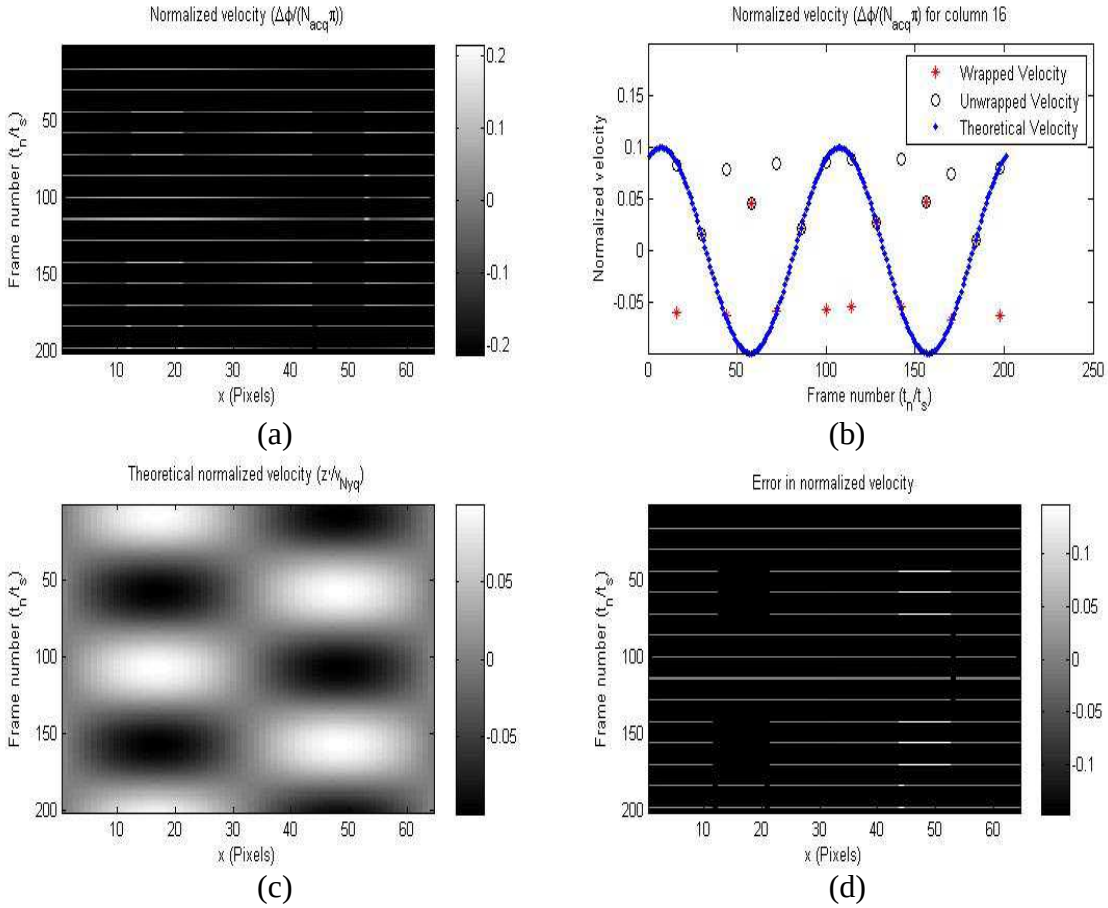

Fig. 3.14 (a) Normalized velocity $\Delta\Phi/(N_{acq}\pi)$ for a horizontal ROI (64×1 pixels) recorded at 100kHz and N_{acq}=14, for an object vibrating harmonically at 250 Hz and V=0.1V_{Nq} .(b) Wrapped velocity, unwrapped velocity and theoretical velocity for column 16. (c) Theoretical normalized velocity for the horizontal ROI and (d) error in retrieved normalized velocity for the horizontal ROI.

If $V = 0.2V_{Nq}$ is assumed, unwrapping the velocity is successful for $N_{acq} = 8$ as shown in Figure 3.15; it fails when $N_{acq} = 10$ is considered as shown in Figure 3.16. This agrees with Equation 3.10 that imposes:

$$N_{acq} \leq 8.9 \qquad (3.14)$$

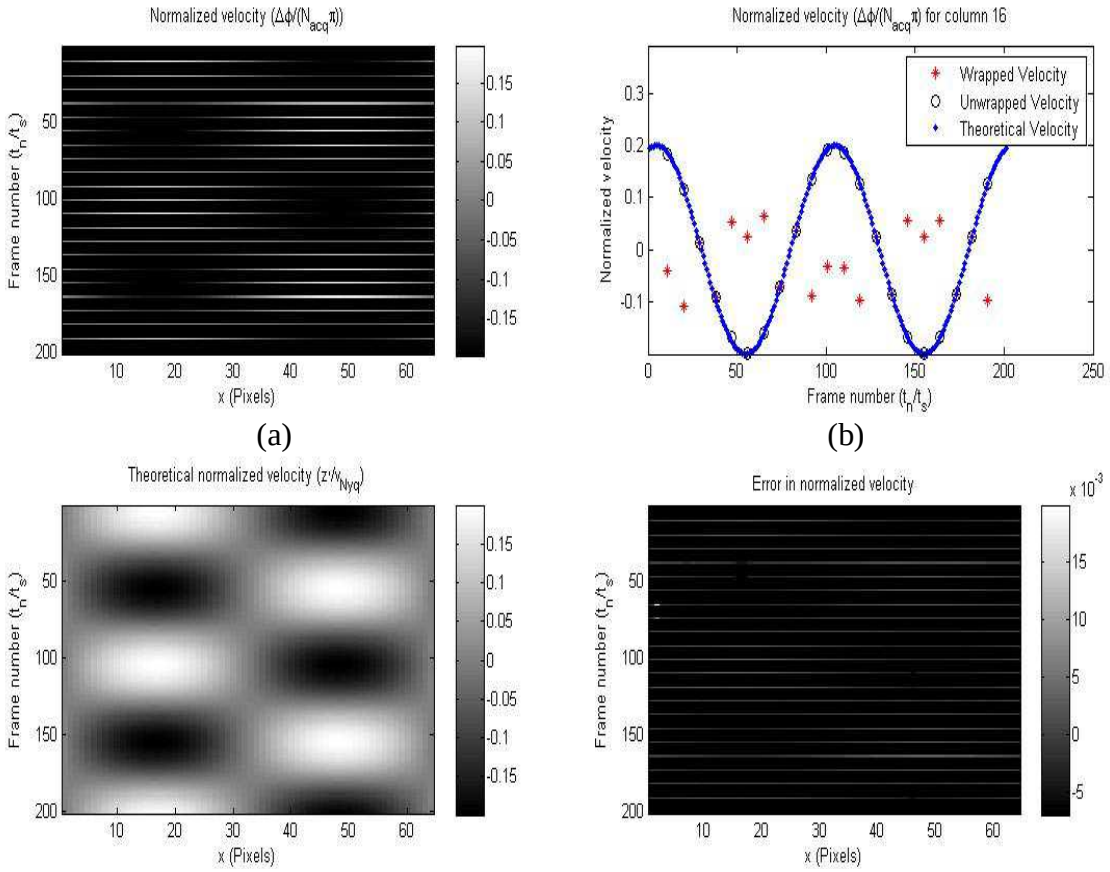

Fig. 3.15 (a) Normalized velocity $\Delta\Phi/(N_{acq}\pi)$ for a horizontal ROI (64×1 pixels) recorded at 100 kHz and N_{acq}=8, for an object vibrating harmonically at 250 Hz and V=0.2V_{Nq} .(b) Wrapped velocity, unwrapped velocity and theoretical velocity for column 16. (c) Theoretical normalized velocity for the horizontal ROI and (d) error in retrieved normalized velocity for the horizontal ROI.

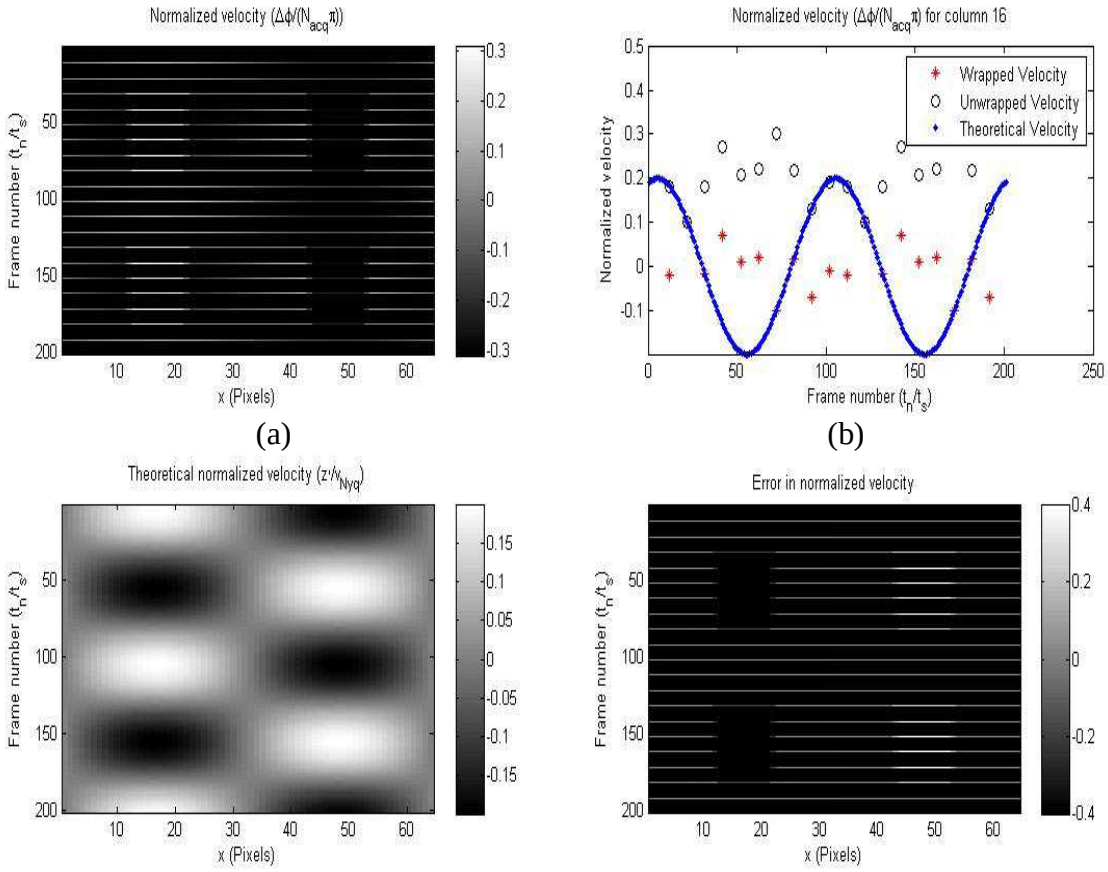

Fig. 3.16 (a) Normalized velocity $\Delta\Phi/(N_{acq}\pi)$ for a horizontal ROI (64×1 pixels) recorded at 100kHz and N_{acq}=10, for an object vibrating harmonically at 250 Hz and V=0.2V_{Nq} .(b) Wrapped velocity, unwrapped velocity and theoretical velocity for column 16. (c) Theoretical normalized velocity for the horizontal ROI and (d) error in retrieved normalized velocity for the horizontal ROI.

Finally $V = 0.3V_{Nq}$ is assumed. Unwrapping the velocity is successful if $N_{acq} = 7$ as shown in Figure 3.17; it fails if $N_{acq} = 8$ is considered as shown in Figure 3.18 and according to Equation 3.10, that imposes:

$$N_{acq} \leq 7.3 \qquad (3.15)$$

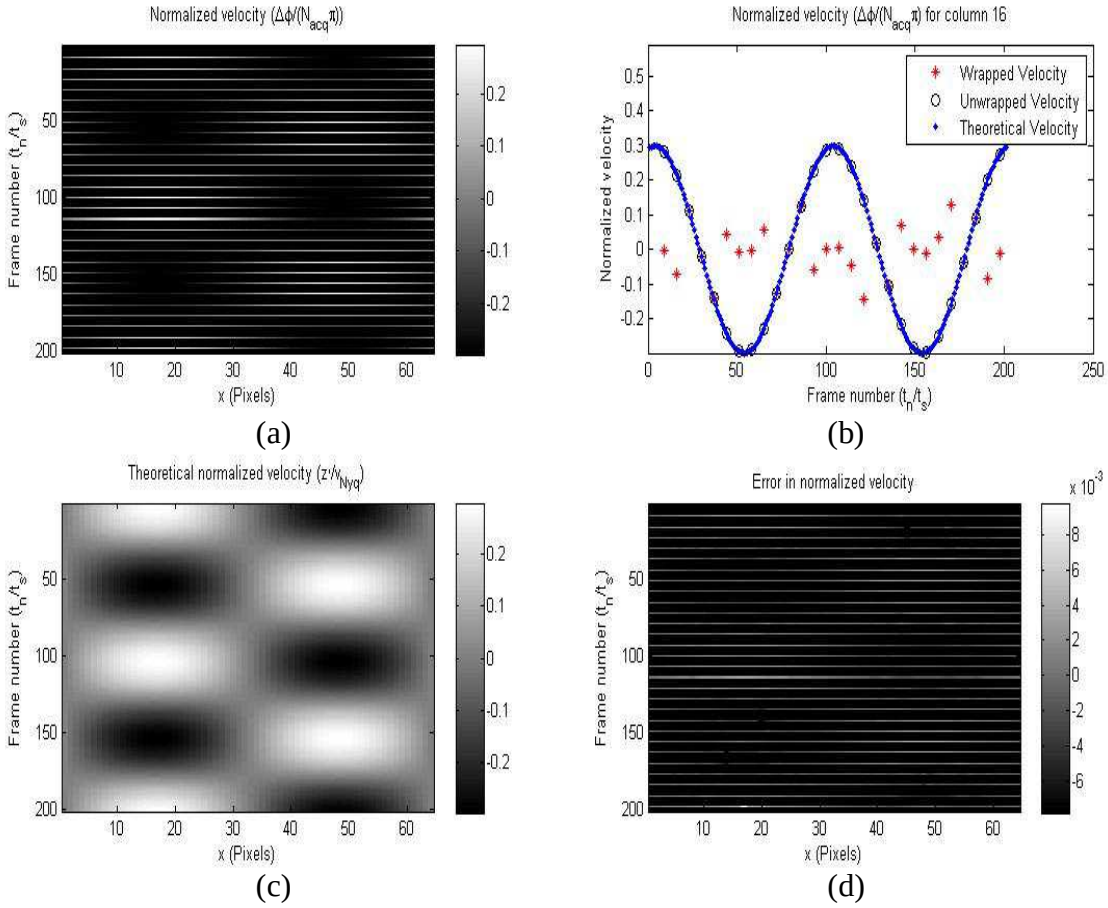

Fig. 3.17 (a) Normalized velocity $\Delta\Phi/(N_{acq}\pi)$ for a horizontal ROI (64×1 pixels) recorded at 100 kHz and N_{acq}=7, for an object vibrating harmonically at 250 Hz and V=0.3V_{Nq} .(b) Wrapped velocity, unwrapped velocity and theoretical velocity for column 16. (c) Theoretical normalized velocity for the horizontal ROI and (d) error in retrieved normalized velocity for the horizontal ROI.

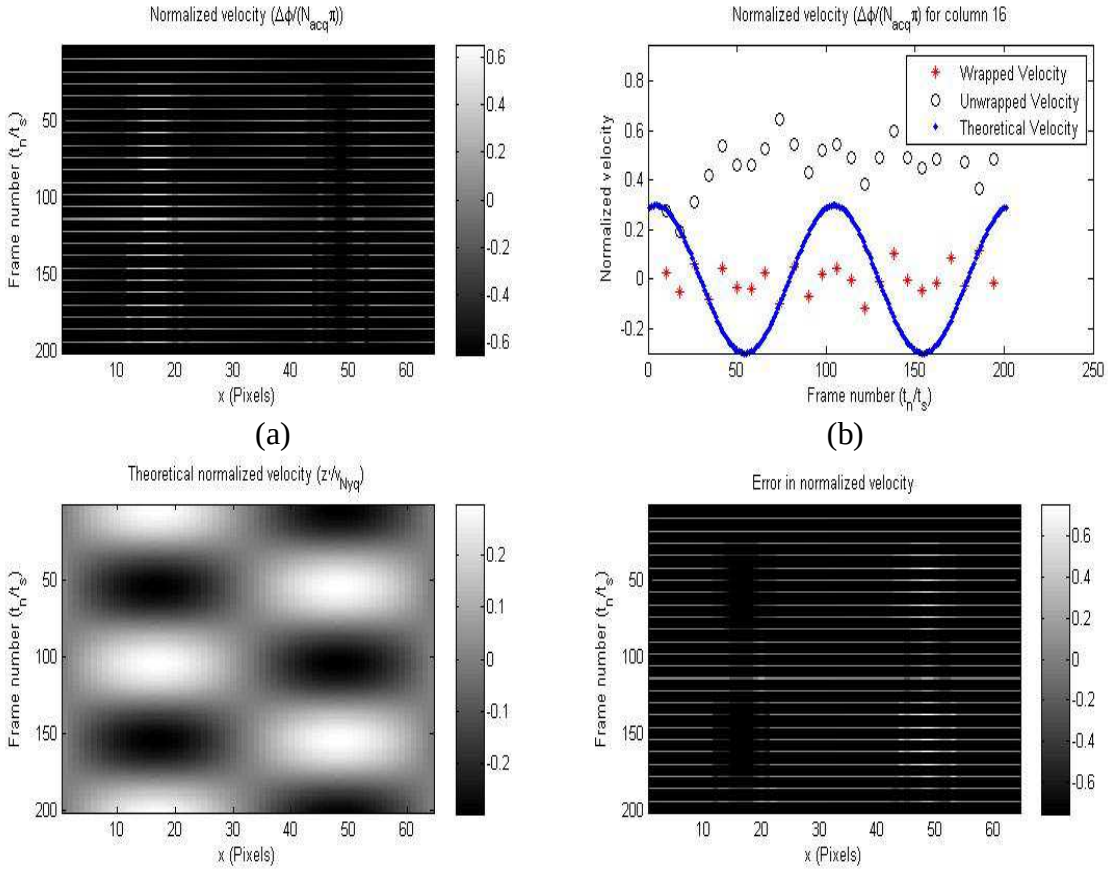

Fig. 3.18 (a) Normalized velocity $\Delta\Phi/(N_{acq}\pi)$ for a horizontal ROI (64×1 pixels) recorded at 100 kHz and N_{acq}=8, for an object vibrating harmonically at 250 Hz and V=0.3V_{Nq} .(b) Wrapped velocity, unwrapped velocity and theoretical velocity for column 16. (c) Theoretical normalized velocity for the horizontal ROI and (d) error in retrieved normalized velocity for the horizontal ROI.

These simulations also validate the restrictions imposed on N_{acq} by the surface acceleration according to Equation 3.10. Tab. 3.4 summarizes the last set of simulation results.

Velocity	Theoretical Limit	Simulated Successful Unwrapping	Simulated Failed Unwrapping
$0.1V_{Nq}$	$N_{acq} \leq 12.6$	$N_{acq} = 13$	$N_{acq} = 14$
$0.2V_{Nq}$	$N_{acq} \leq 8.9$	$N_{acq} = 8$	$N_{acq} = 10$
$0.3V_{Nq}$	$N_{acq} \leq 7.7$	$N_{acq} = 7$	$N_{acq} = 8$

Tab. 3.4. Summing up of simulations testing validity of Equation 3.10. A comparison between the theoretical prediction of the maximum N_{acq} value and the maximum simulated N_{acq} value, is shown.

3.4 Summary

This chapter has described the novel CMOS detector array and the detection system used in this project.

The data processing strategy to phase unwrapping via inter-frame phase stepping is also discussed. This novel approach doesn't lead to any increase in the maximum surface velocity limit that can be reliably measured, but it increases the system data transfer rate.

An analysis of the performances of this approach in terms of the maximum surface velocity that can be measured and of the increase in the system data transfer rate is reported. The increase in data transfer rate is strictly related to the number of samples that can be skipped during the readout between any two adjacent frames.

The system is tested using a simulation model whose output validates the theoretical limits.

Chapter Four

CMOS camera response

4.1 Characterization of camera response

The detection system consists of a custom CMOS detector array of 64x64 pixels, a field programmable gate array, providing control of logic and clocks, and an analog-to-digital converter ADC, which has a depth of 12 bits and theoretical sampling rate equal to 25 MHz, under personal computer control. The ADC board input voltage is in the range of [-5 V, +5 V], described by 2^12 elements, whereas the camera output voltage is in the range [0.6 V, 2V]. This enables an encoded light intensity output in the range [2270, 2870], corresponding to approximately 600 intensity levels.

A source of error in images acquired by the detector is the dark current, which is the current that flows in the circuitry, thermally generated by carriers or other forms of leakage not related to the illumination. Its effect can be reduced by taking a number of dark frames before the experiment, and then subtracting them from the frames acquired during the experiment.

The camera response to an incident laser beam of linearly increasing power was characterized by exposing all of the 64x64 pixels. An average camera response was plotted for each of the four camera channels, through 50 acquisition points corresponding to power levels ranging from 0 mW up to 500 mW and equally spaced by an increase of 10 mW. The optical setup initially used was optical fibre based; hence the laser beam was launched into the fast axis of a highly birefringent optical fibre and then focused on the camera pixels. The output power of the laser was usually restricted to 500 mW so as not to damage the proximal fibre end and hence limiting the amount of light illuminating the camera pixels. The maximum available light was also limited by the efficiency in coupling the optical fibre; the best coupling efficiency achieved was of 42%.

Figure 4.1 shows the camera average intensity response, with the camera locking-in a frequency $F_{Mod} = 875\,Hz$ and sampling at a frequency $f_s = 3.5\,kHz$. This value represents the lower framing rate the camera can use when the frames are sequentially acquired from each of the four channels available. This also enables time exposures to be the longest possible, so as to collect the most of the light available.

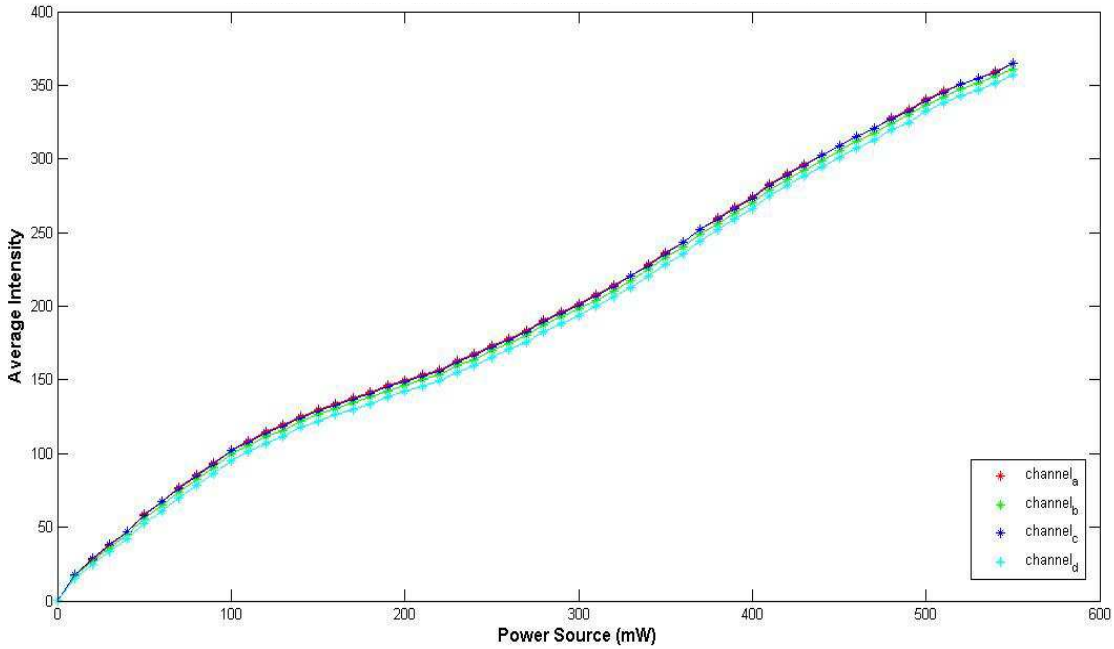

Fig. 4.1. Camera average intensity response plotted against linearly increasing of the laser beam power. The four channels average intensity response is shown when $F_{Mod} = 875$ Hz, $F_s = 3.5$ kHz and $N_{acq} = 12$.

The maximum average intensity detected doesn't exceed 370 intensity levels, hence meaning that approximately half of the camera dynamic range is not characterized. This was attributed to a not high enough amount of light illuminating the camera pixels array. For this particular case a maximum power of 550 mW was used in order to increase the maximum amount of light available. The camera average intensity response is not linear and shows different channel responses, meaning that every channel has a different gain with respect to equal amount of light. The difference in channel gain arises in the part of the characteristic ranging from 0 to 100 intensity levels; then it becomes constant likely a DC offset between the four channels.

By deliberately reducing the fibre coupling efficiency, we repeated the previous characterization in an attempt to increase the resolution of the camera response in the low intensity region of Figure 4.1. Figure 4.2 clearly shows a different gain for each of the

four channels, which then becomes approximately constant when higher intensities are detected.

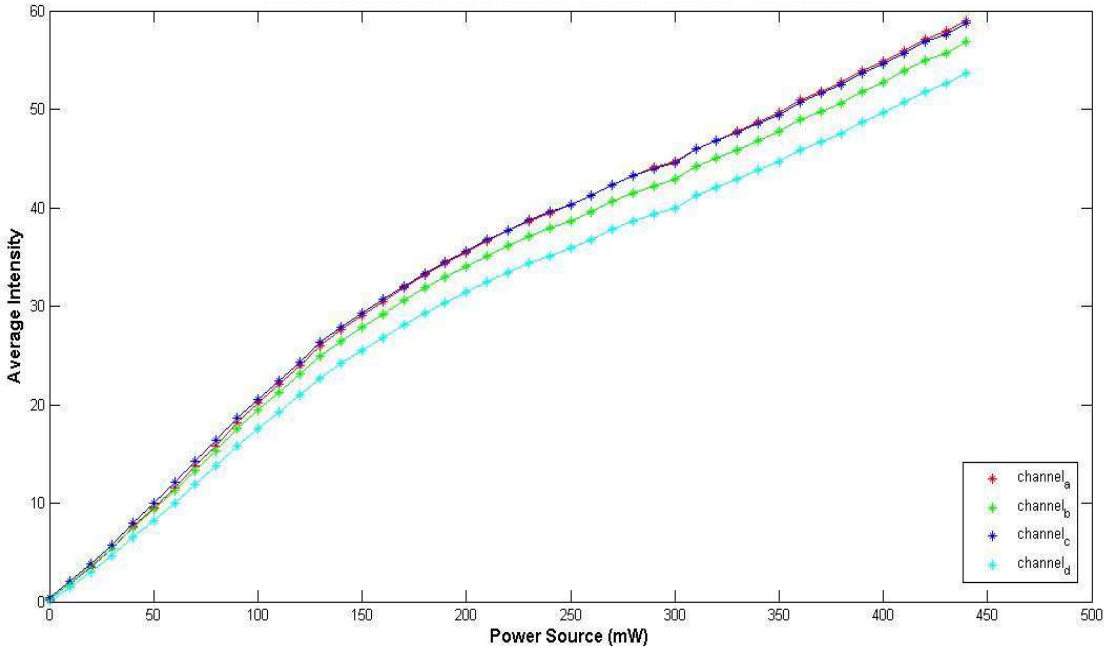

Fig. 4.2. Camera average intensity response plotted against linearly increasing of the laser beam power in the case of reduced fibre coupling efficiency. The four channels average intensity response is shown when $F_{Mod} = 875$ Hz, $F_s = 3.5$ kHz and $N_{acq} = 12$.

A new setup, increasing the total amount of available light, was then developed in order to characterize the full dynamic range of the camera. The laser beam illuminating the camera array was no longer sent down the fibre, thus eliminating any loss in the coupling procedure, and potentially enabling the exceeding of the restriction on the maximum laser power that could be used so as to not damage the proximal fibre end. Initially the total amount of available light was so high that it could saturate the camera at 200 mW. A neutral density filter was introduced between the laser and the camera array, in order to reduce the intensity of the beam up to a level that didn't saturate the camera average intensity response when a power of 500mW was used. This arrangement enabled the characterization of the response for a reasonable large number of points and in conformity with the previous analysis. Figure 4.3 shows the new camera average intensity response, with the camera locking-in a frequency $F_{Mod} = 875\ Hz$ and sampling at a frequency $f_s = 3.5\ kHz$.

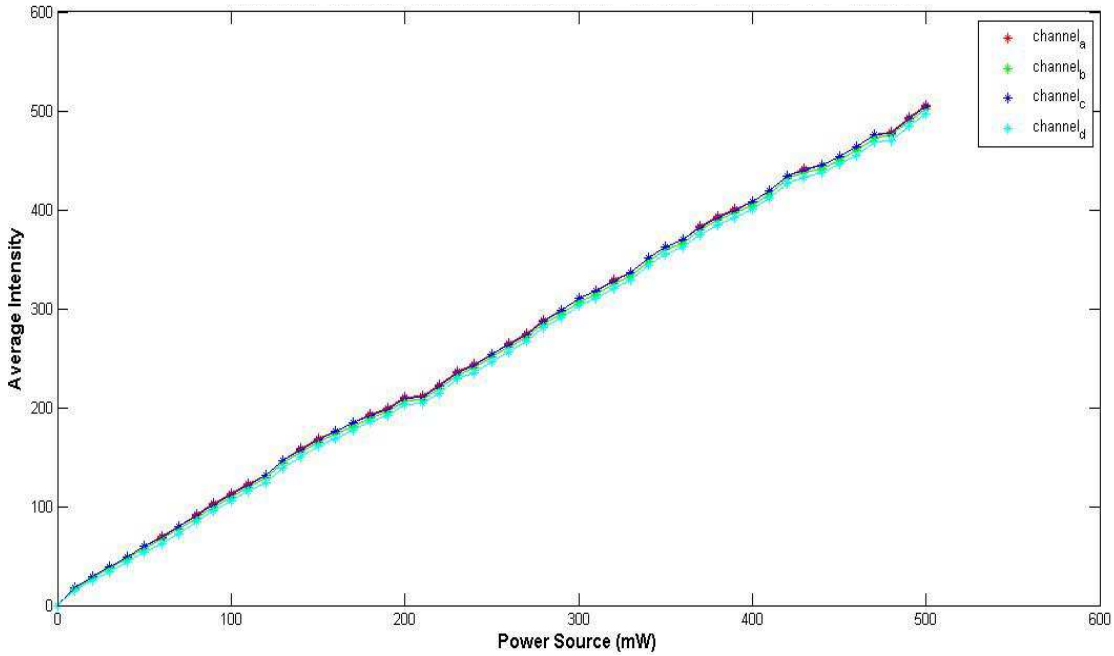

Fig. 4.3. New camera average intensity response plotted against linearly increasing of the laser beam power. The four channels average intensity response is shown when $\mathbf{F_{Mod}} = \mathbf{875\ Hz}$, $\mathbf{F_s} = \mathbf{3.5\ kHz}$ and $\mathbf{N_{acq}} = \mathbf{12}$.

The maximum intensity achievable on average is boosted up to 540 Intensity Levels. The camera saturation is usually reached when a light intensity corresponding approximately to 600 intensity levels is detected; however this can vary from pixel to pixel meaning that the dynamic range of each pixel response can be very different. This was attributed to a difference in each of the 4096 pixel gains with respect to the same amount of light. On this particular occasion an amount of light yielding a maximum average intensity not higher than 540 intensity levels was chosen in order to not include too many saturated pixels in the camera response characterization that would be otherwise distorted. The camera average intensity response is approximately linear but still shows different channel responses. The difference in the channel's gains arises in the part of the characteristic ranging from 0 to 100 intensity levels; then it becomes constant likely a DC offset between the four channels.

Finally the analysis was conducted for a different frame rate of interest, in order to characterize eventual differences in camera response depending on the frame rate used. Figure 4.4 shows the camera average intensity response, with the camera locking-in a frequency $F_{Mod} = 1750\ Hz$ and sampling at a frequency $f_s = 7\ kHz$.

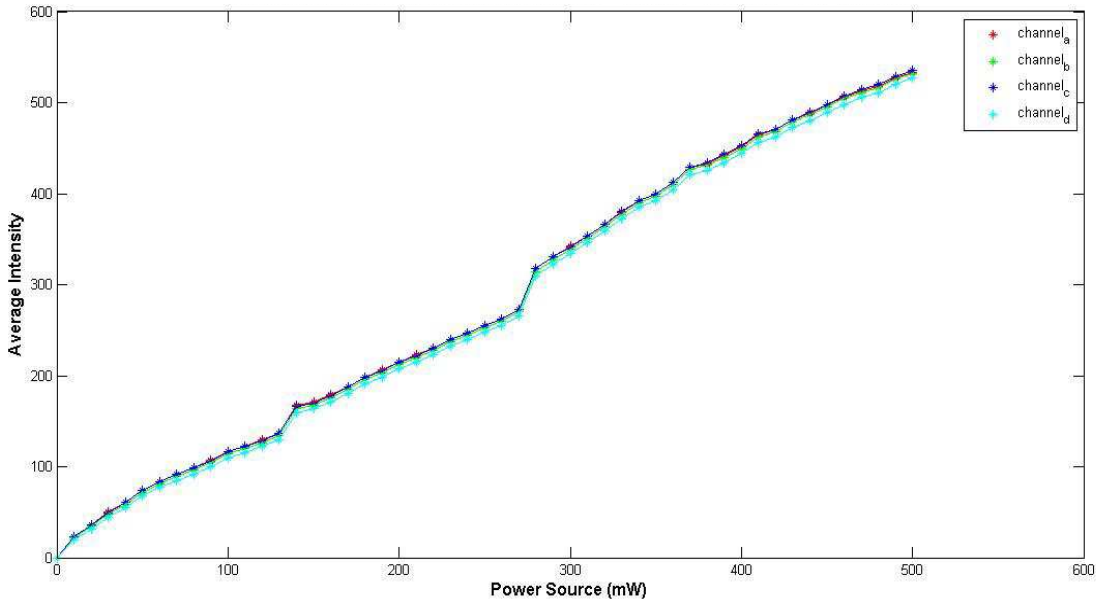

Fig. 4.4. Camera average intensity response plotted against linearly increasing of the laser beam power. The four channels average intensity response is shown when $F_{Mod} = 1750$ Hz, $F_s = 7$ kHz and $N_{acq} = 12$.

The shorter time exposure between any two adjacent frames reduces the total light detected, thus avoiding saturation intensity values to be reached. Hence no neutral density filter was used on this occasion. No appreciable difference is shown in the gain of the channels with respect to the previous characterizations, whereas a relevant difference is shown in the average intensity response. It now exhibits three distinct regions separated by discontinuities.

This analysis shows that the camera average intensity response depends strongly on the total amount of light available and the frame rate. The reduction of available light due to a higher frame rate can be compensated by increasing the total amount of incident light on the detector. However it also reduces the camera readout since T_{ex} becomes shorter accordingly to Equation 3.1, thus introducing differences in detection of the light. A difference in the average response of the four available channels also arises despite the frame rate used. This was attributed to the different gain of each channel with respect to equal amount of light when low intensities are detected, whereas it becomes a DC offset between the four channels when higher intensities illuminate the array.

4.2 Single pixel camera response

Each of the 64x64 camera pixels has a different dynamic range as previously stated. This means that the saturation intensity value might change for each pixel and hence each pixel shows a different gain with respect to a linear increase of light. A study of the single pixel response was conducted, to investigate how different the single pixel gains might be. The pixel response and its offset can be defined as shown in Figure 4.5 (a), and they can be used as a measure of the gain of every pixel.

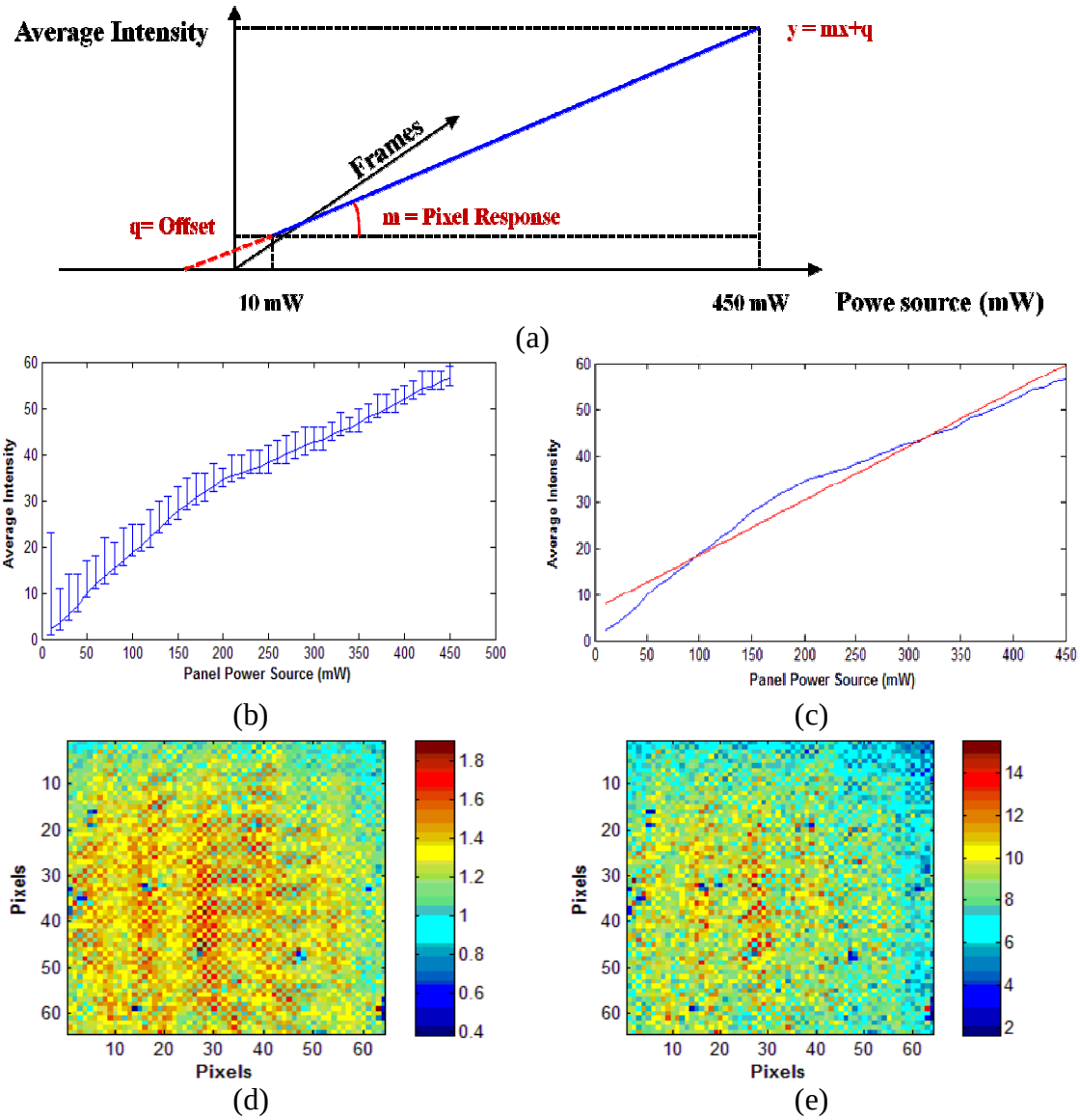

Fig. 4.5 (a) Definition of pixel response and offset. (b) Response of the pixel (32,32) and (c) Linearization of pixel (32,32) response by using the Least Square Fitting method. (d) Two dimensional map of pixel responses and (e) two dimensional map of pixel offsets.

Figure 4.5 (b) shows the response of pixel (32, 32) for a linear increase of the power. Each point of the response is the average of the intensities detected at each of the frames acquired; the error bar shows the maximum and minimum intensities detected from which the average is calculated. The response can be linearized by using the Least Square Fitting method as shown in Figure 4.5 (c) and thus enabling the computation of the *m* and *q* values for each pixel. Figure 4.5 (d) shows a 2D map indicating the *m* value for each of the 64x64 pixels, whereas Figure 4.5 (e) shows a 2D map indicating the *q* values.

It is worth mentioning that the Gaussian distribution of the laser beam illuminating the array of pixels might affect this analysis as the external pixels could receive less light than the most internal ones. However a considerable difference in response is shown also in adjacent pixels despite of their position in the array. This consideration allows for the conclusion that the gain and the offset of each pixel might considerably change throughout all the pixels in the array.

4.3 Calibration of the CMOS camera response

A calibration of camera response was found necessary in order to compensate the different gain of each channel response with respect to the light as shown in Figure 4.2. Depending on the frame rate used, the camera response was found to be not linear, and hence the compensation also aims to linearize it. Since the average camera response was found strongly dependent on the frame rate used and the amount of light available, a different calibration needed to be applied accordingly to each different case. We first took into consideration the average camera response obtained when a frequency $F_{Mod} = 875\,Hz$ was locked-in and a sampling frequency $f_s = 3.5\,kHz$ was set, as previously shown in Figure 4.1. Figure 4.6 shows the average intensity response of one channel and the different polynomial fits ranging from the first to the seventh order. The precision of each fit was evaluated by using the Root Mean Square Error and accordingly to:

$$RMSE = \sqrt{\frac{\sum_{i=1}^{n}\left(x_{1,i} - x_{2,i}\right)^2}{n}} \tag{4.1}$$

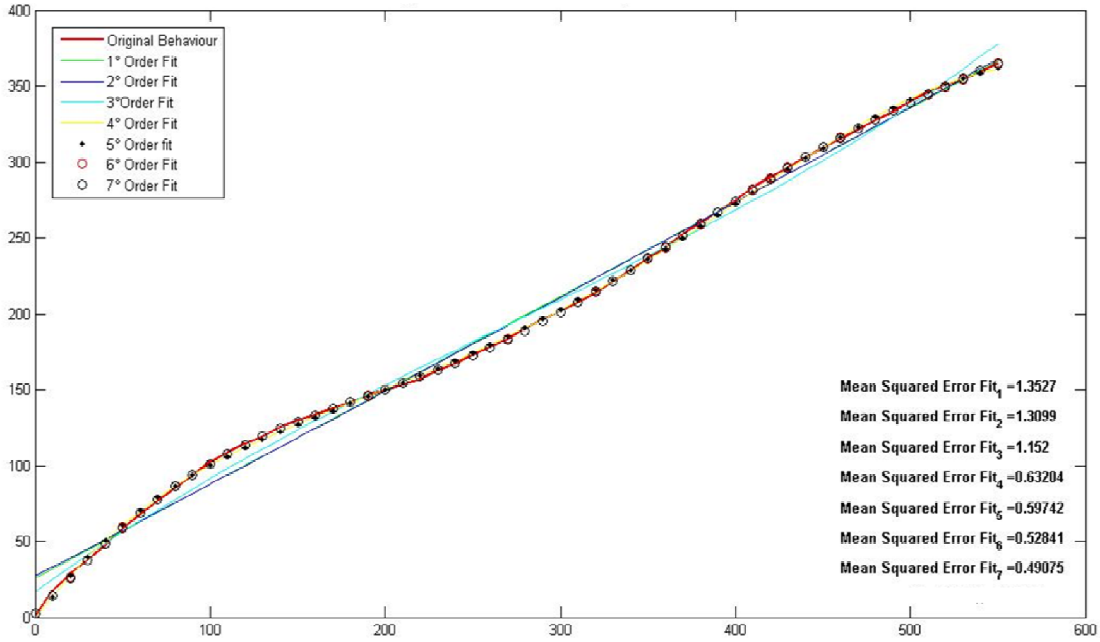

Fig. 4.6. Single channel average intensity response plotted against linearly increasing of the laser beam power when $F_{Mod} = 875$ Hz, $F_s = 3.5$ kHz and $N_{acq} = 12$. Different order of polynomial fits and relative RMSEs are shown.

The seventh order polynomial fit was chosen, since it showed the lowest RMSE in approximating the channel average intensity response. Once the best order of fit was determined, it was calculated for all of the four channels. Figure 4.7 (a) shows the polynomial fit of the channels, the desired channel response and the polynomial fits obtained by flipping the axis. Inverting the axis allows us to determine easily the correction we want to apply to the channel responses in order to linearize and compensate them accordingly to:

$$f^{-1}f(x) = x \tag{4.2}$$

Figure 4.7 (b) shows the inverse channel responses. The inverse equations were finally used to correct the original channel average intensity responses by evaluating each intensity with equation 4.2 as shown in Figure 4.7 (c). Results demonstrate that the channel average intensity responses are linearized and the difference in channel gains is compensated; the error introduced only depends on the fit approximation and it is negligible.

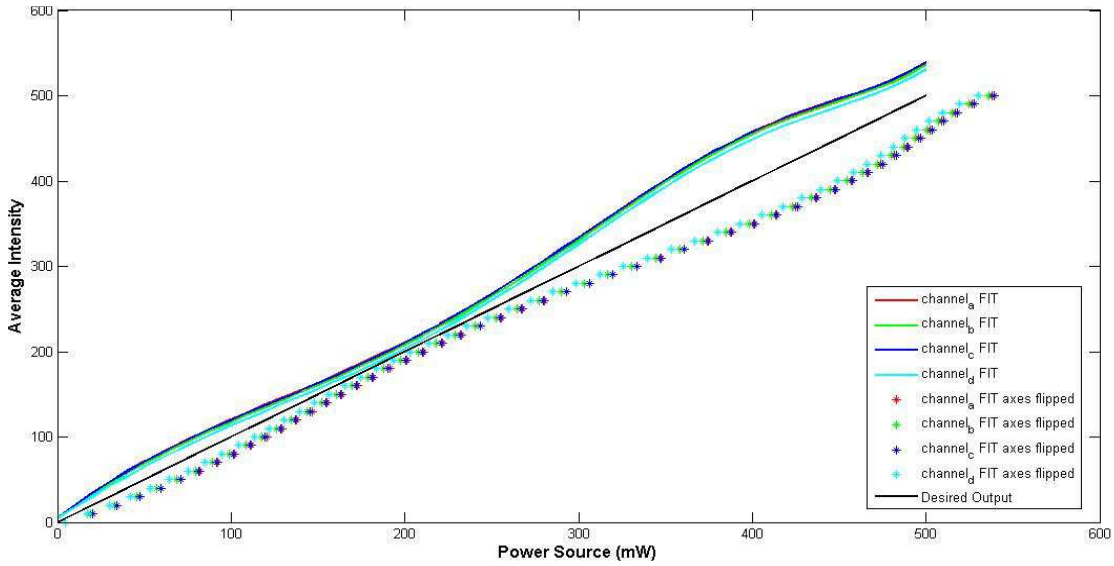

(a)

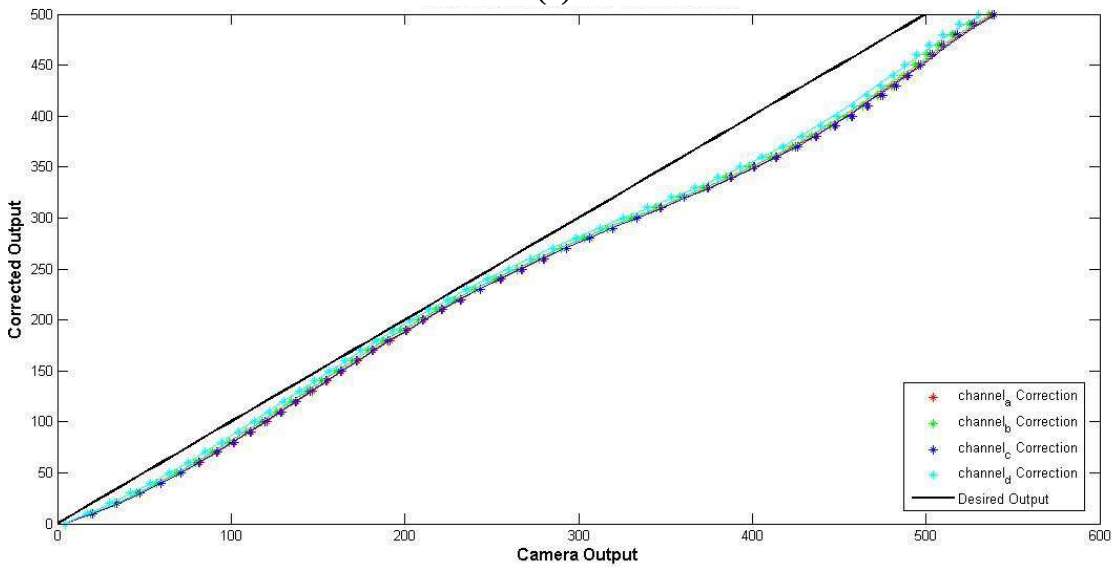

(b)

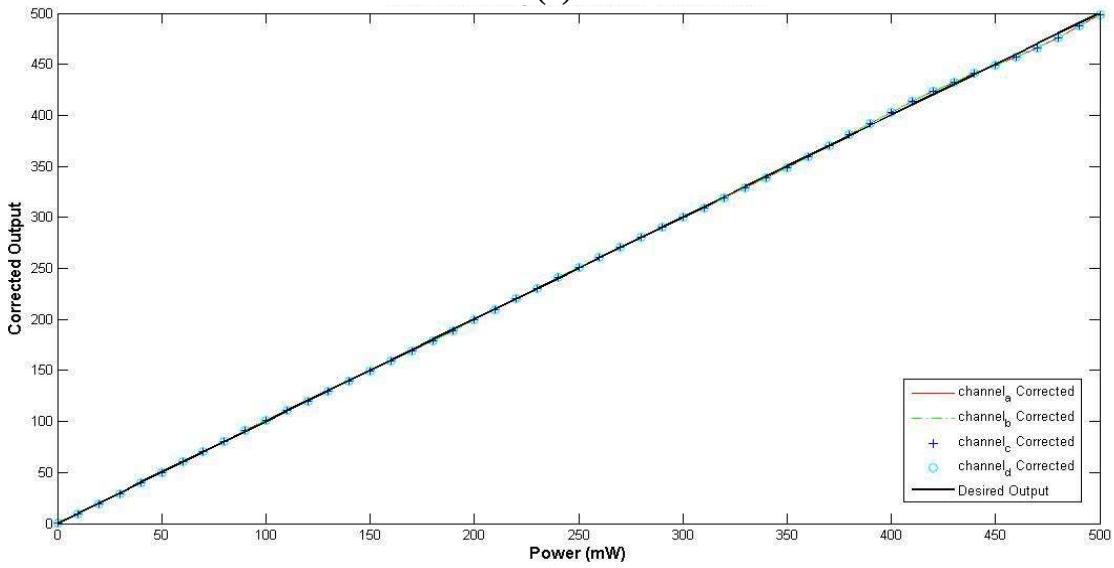

(c)

Fig. 4.7 (a) 7th Order polynomial fits of the four channel responses, (b) inverse 7th order polynomial fits and (c) corrected camera average intensity response.

Then we repeated the same analysis for the average camera intensity response obtained when a frequency $F_{Mod} = 1750\,Hz$ was locked-in and a sampling frequency $f_s = 3.5\,kHz$ was set, as previously shown in Figure 4.4.

However this type of correction, performed on the channel average intensity responses, was found to be unsuccessful when it was applied to the raw data acquired from every pixel. Indeed each pixel has a different intensity response and dynamic range, and this means that each pixel needs an independent correction that cannot be based on the camera average response.

Therefore we kept the choice of a 7th order polynomial fit, since on average it was the best approximation of the channel responses (Figure 4.8 (a)); then it was independently calculated for each pixel in order to retrieve an independent correction for each pixel. Figure 4.8 (b) shows the camera average intensity response after the correction was applied to raw data, pixel by pixel.

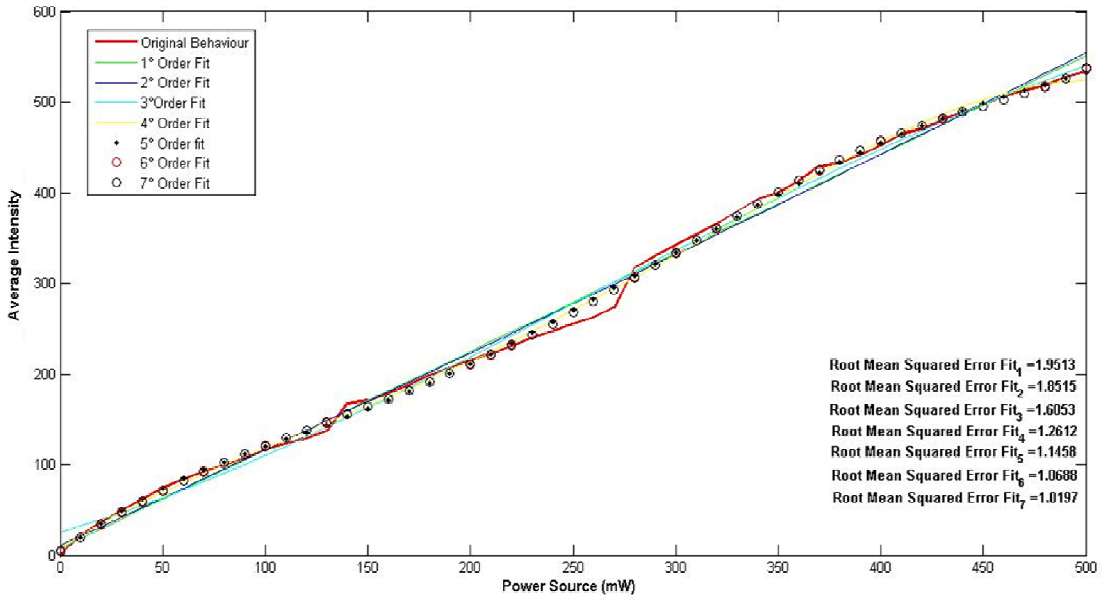

(a)

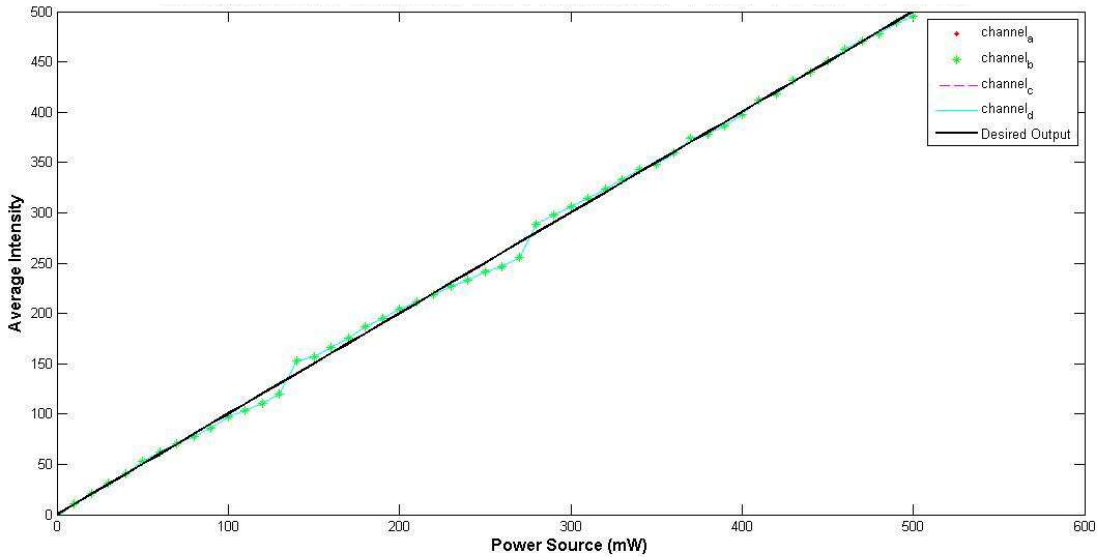

(b)

Fig. 4.8 (a) Single channel average intensity response plotted against linearly increasing of the laser beam power when $F_{Mod} = 1750$ Hz, $F_s = 7$ kHz and $N_{acq} = 12$. Different order of polynomial fits and relative RMSEs are shown. (b)Camera average intensity response after the correction is applied pixel by pixel.

Figures 4.9 (a) and (b) show the responses of two single pixels before the correction whereas Figure 4.9 (c) and (d) show their responses after the correction.

The correction did not eliminate the discontinuities in the camera average intensity response even if broad parts of the characteristic are now very close to the desired output. This clearly depends on the higher level of the approximation in fitting the discontinuities. The performance of the correction on the single pixel response is strongly dependent on how good the approximation introduced by the 7^{th} order fit is. Since the RMSE of the pixel (33,16) fit is lower than the RMSE of the pixel (33,1), the performance of the correction is higher in the first case rather than in the second one. The correction of pixel (33,16) response eliminates the difference in channel gains though some parts of the characteristic are still not linear; the correction of pixel (33,1) is unsuccessful both in the linearization and compensation of the different gains, that are still evident where the error introduced by the fit is locally higher.

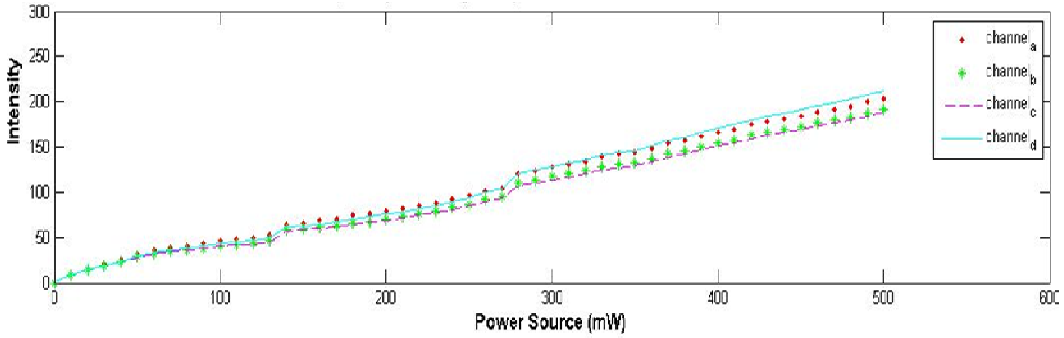

(a)

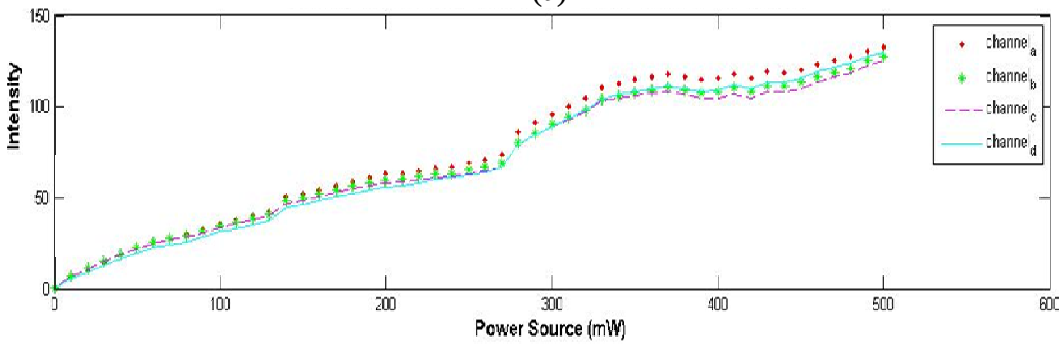

(b)

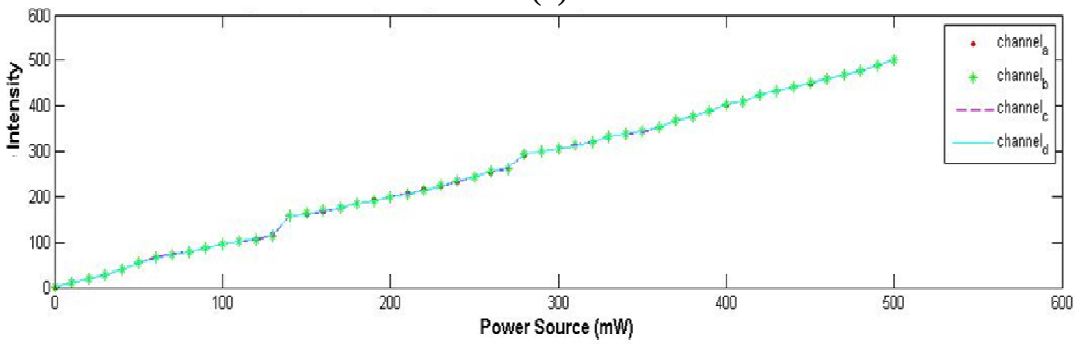

(c)

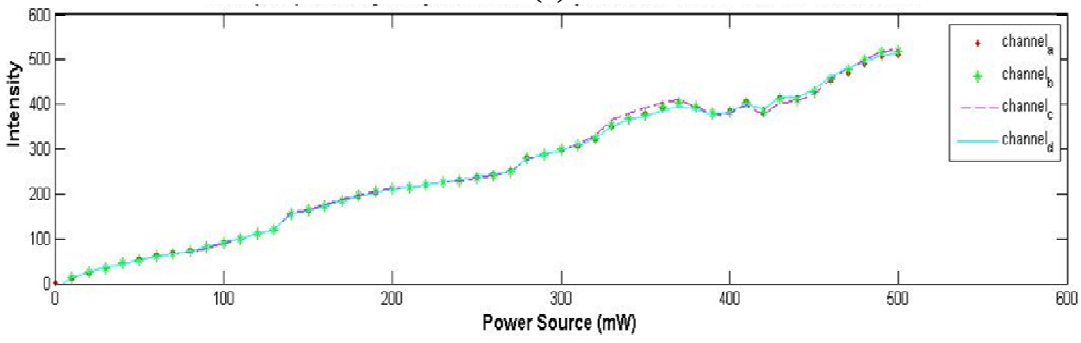

(d)

Fig. 4.9 (a) Pixel (33,16) and (b) Pixel (33,1) intensity responses before correction. (c) Pixel (33,16) and (d) Pixel (33,1) after correction.

A further single pixel analysis was conducted, so as to test how the correction worked locally. A static amount of light illuminated the array of pixels and the responses from only four adjacent pixels were taken in consideration; this choice validated the

assumption of uniform light illuminating all of the four pixels. Figure 4.10 shows the intensity responses of the four pixels acquired through 270 frames, with the camera locking-in a frequency $F_{Mod} = 1750\,Hz$ and sampling at a frequency $f_s = 7\,kHz$.

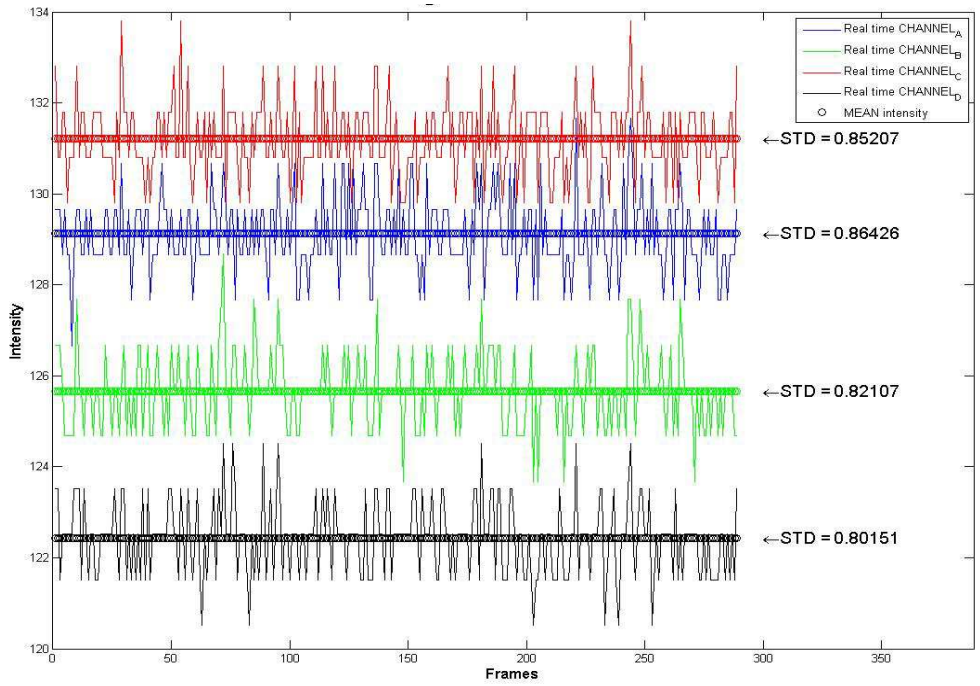

(a)

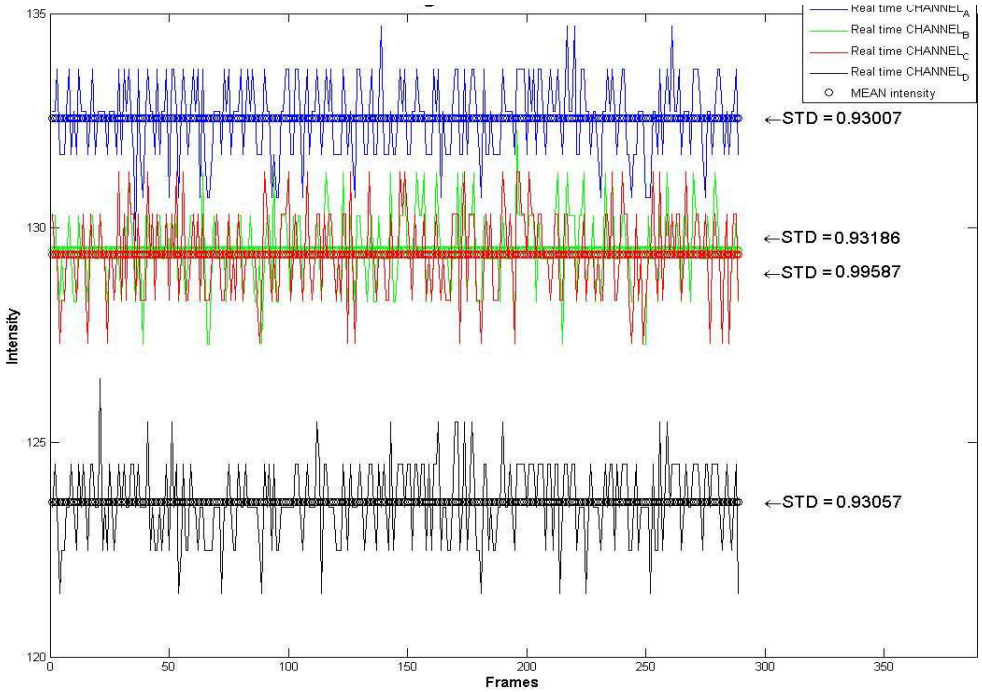

(b)

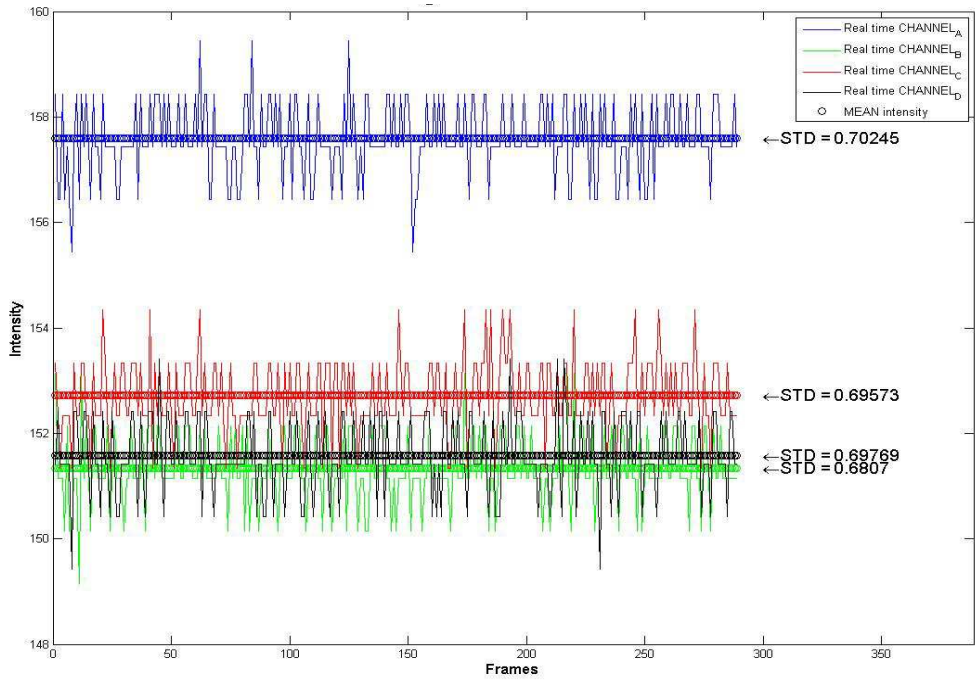

(c)

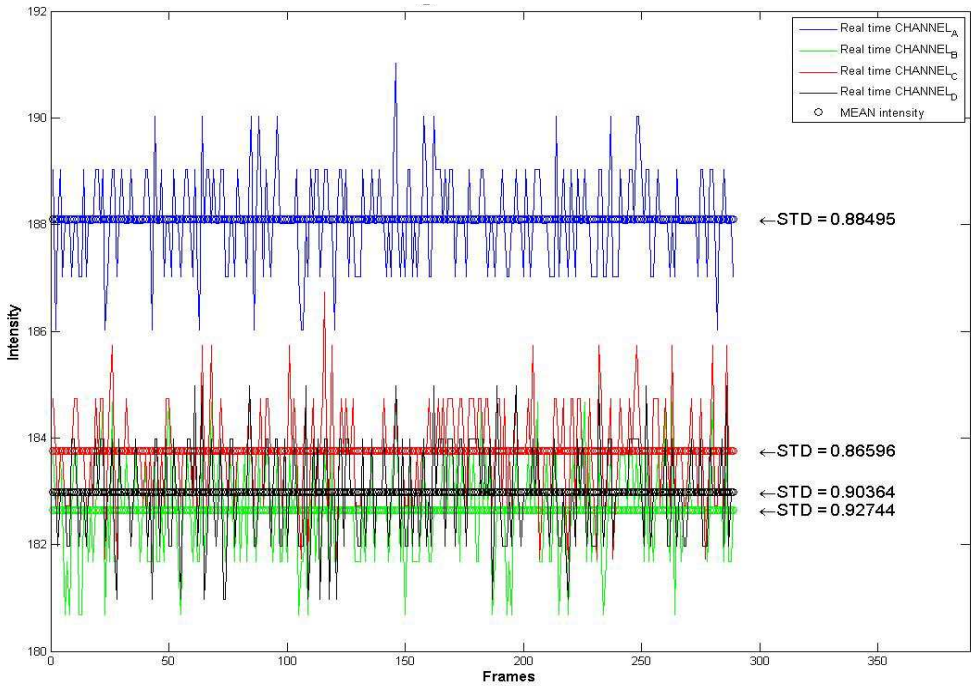

(d)

Fig. 4.10. Intensity responses of (a) pixel (29,33), (b) pixel (28,33), (c) pixel (27,22) and (d) pixel (30,29). The standard deviations and average values of the responses are also shown.

The intensities detected by the four pixels are different because of the different single pixel gain as already discussed. Every channel response shows the digital noise through the frames acquired, with a standard deviation that is lower than one intensity level and

therefore it can be considered negligible. The different channel gains yield to an inversion of the DC levels of light detected by each pixel; the correction we applied would ideally compensate this shift. Figure 4.11 shows the intensity responses after the correction was applied to each pixel.

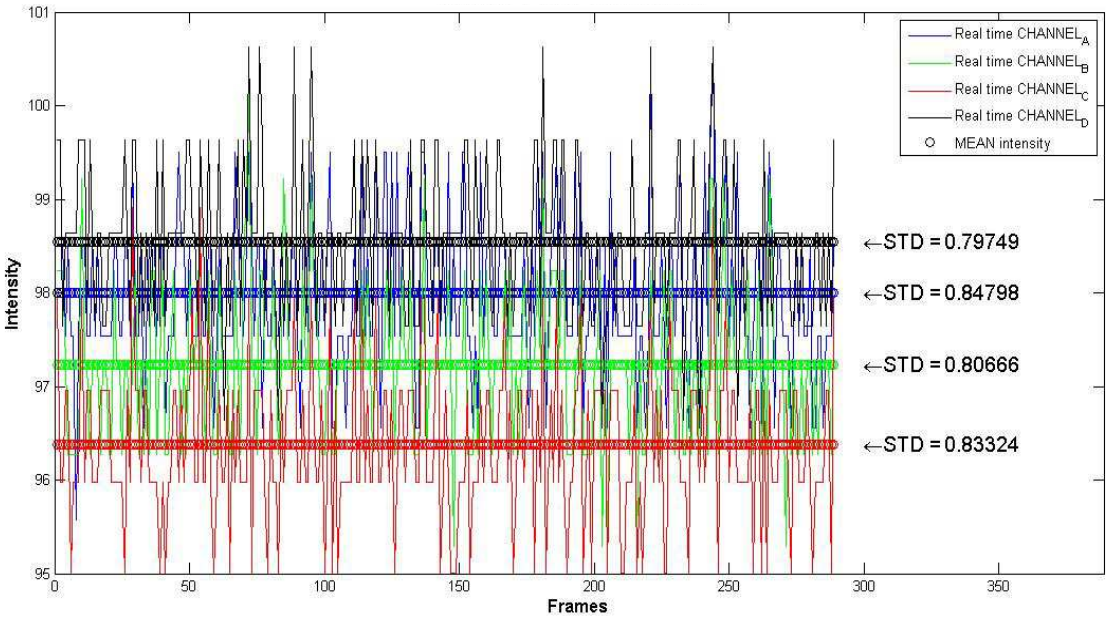

(a)

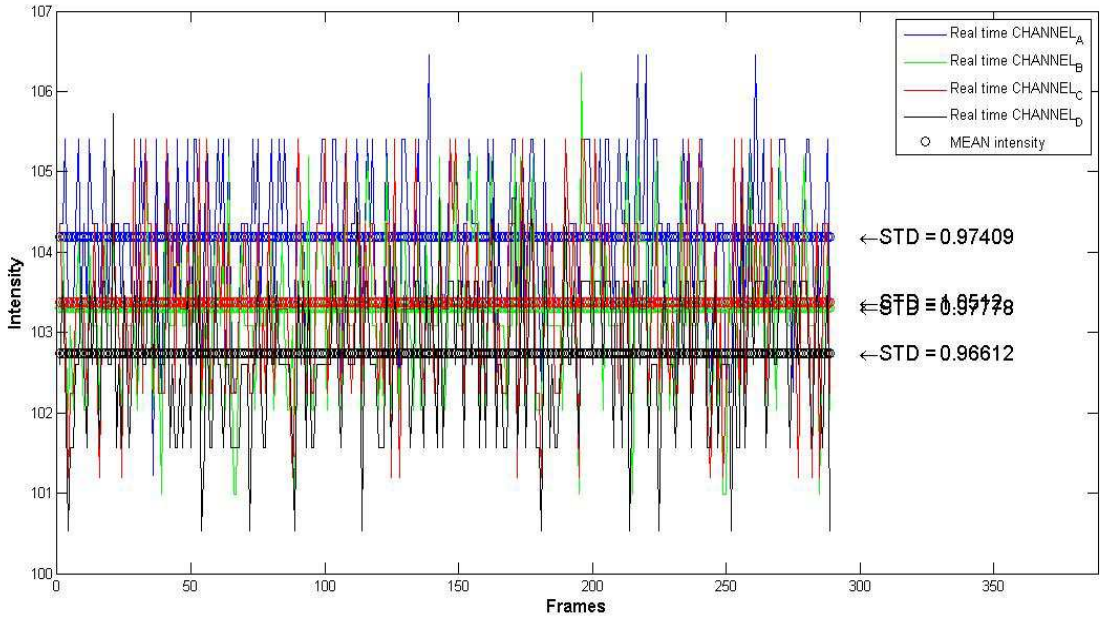

(b)

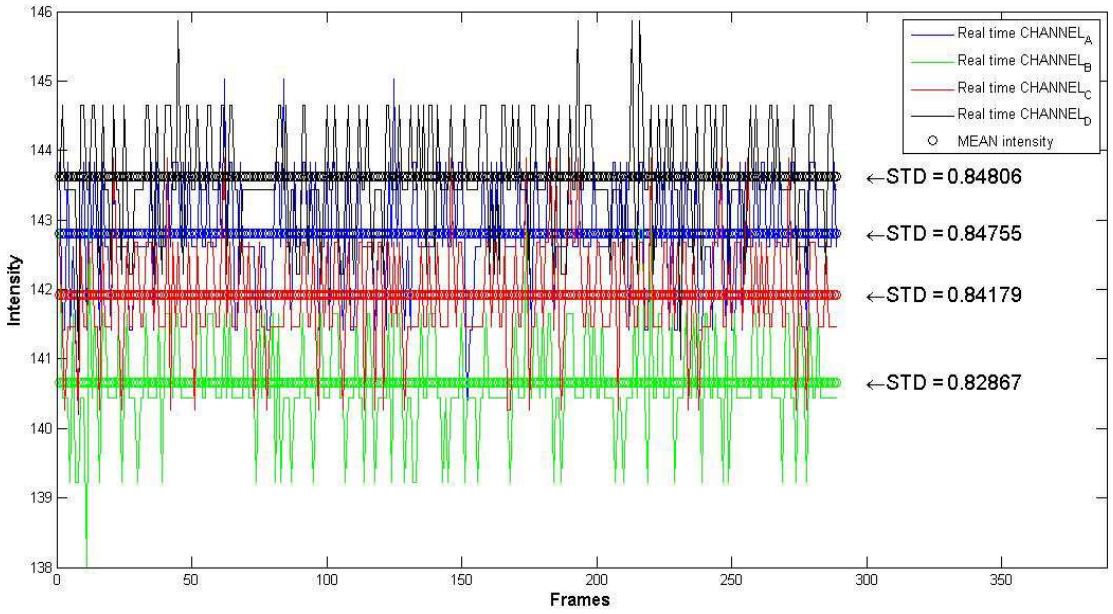

(c)

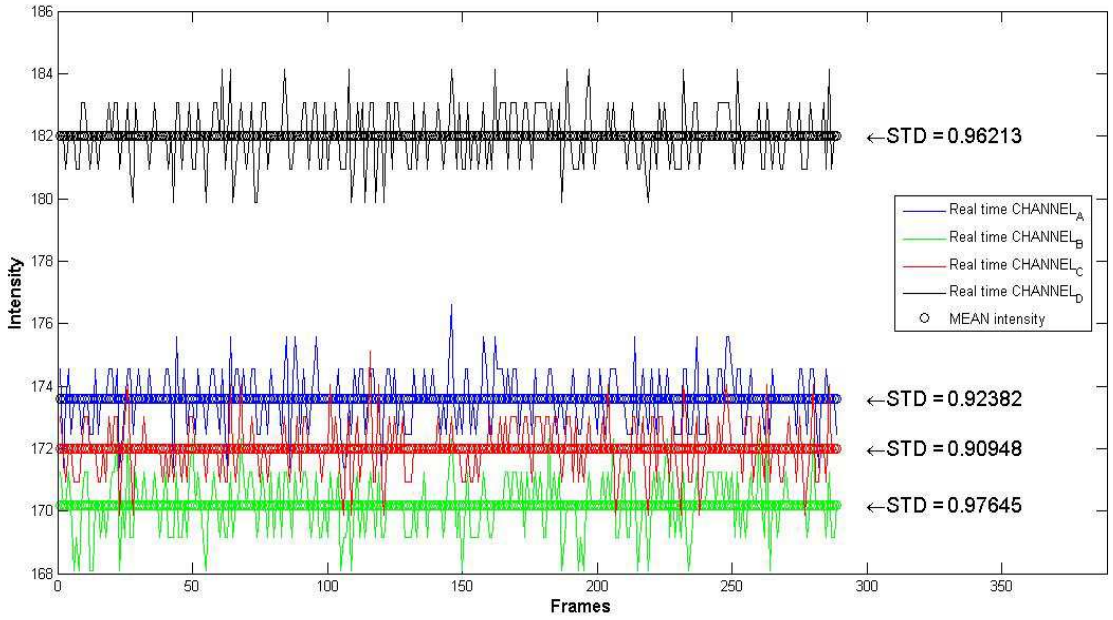

(d)

Fig. 4.11. Corrected intensity responses of (a) pixel (29,33), (b) pixel (28,33), (c) pixel (27,22) and (d) pixel (30,29). The standard deviations and average values of the responses are also shown.

The correction reduces the channels offset for pixels (29,33), (28,33) and (27,22), whereas its performance is very poor for pixel (30,29). The average intensity detected by pixel (30,29) corresponds to that part of the characteristic pixel response that shows a discontinuity (Figure 4.8). Here a high approximation of the polynomial fit reduces the quality of the correction we apply, thus leading to the results shown in Figure 4.11 (d) which cannot be considered satisfactory.

4.4 Discussion

A characterization of the CMOS camera response was performed. The average intensity response of all the pixels to a linear increase of the power illuminating the array was considered for different camera frame rates of interest. Results showed that the camera average intensity response depends strongly on the total amount of light available and the frame rate used. They also showed that a difference in the average response of the four available channels arises. This was attributed to a different gain of each channel with respect to equal amount of light when low intensities are detected, whereas it becomes a DC offset between the four channels when higher intensities illuminate the array. A further analysis of the response of each pixel was performed, enabling the conclusion that also pixels have a different gain with respect to equal amount of light.

A calibration of camera response was found necessary in order to compensate the different gain of each channel, whereas the different single pixel gain was not found problematic for our purposes. The calibration aimed to linearize and compensate the response of the four channels for a particular frame rate used. The method was based on a 7^{th} order polynomial fit of each single pixel response allowing us to determine the correction needed. This approach showed an improvement in compensating the gain of the channels; however their average intensity response was not completely linearized because of the error introduced by the high RMSE of the fit at those pixels having a very different response from the averaged one.

A further analysis of the performance of the correction on the single pixel response was conducted. Results showed that pixels have different responses and dynamic ranges, thus enabling the conclusion that the correction output strongly depends on how good the approximation introduced by the 7^{th} order fit is for each individual pixel. It was demonstrated that pixels having a lower RMSE show a more efficient correction that those having a higher RMSE.

The final conclusion was that this approach solves the issue of having different channel gains only at some pixels, whereas it is not satisfactory in the linearization of the characteristic response of the CMOS camera.

Chapter Five

Experimental work

5.1 Experimental setup

The experimental system, on which the work of this thesis is based, was initially developed using the experience of the high-speed system which was already at Heriot-Watt University, as reviewed in Section 2.4.1. A schematic of the experimental system is shown in Figure 5.1.

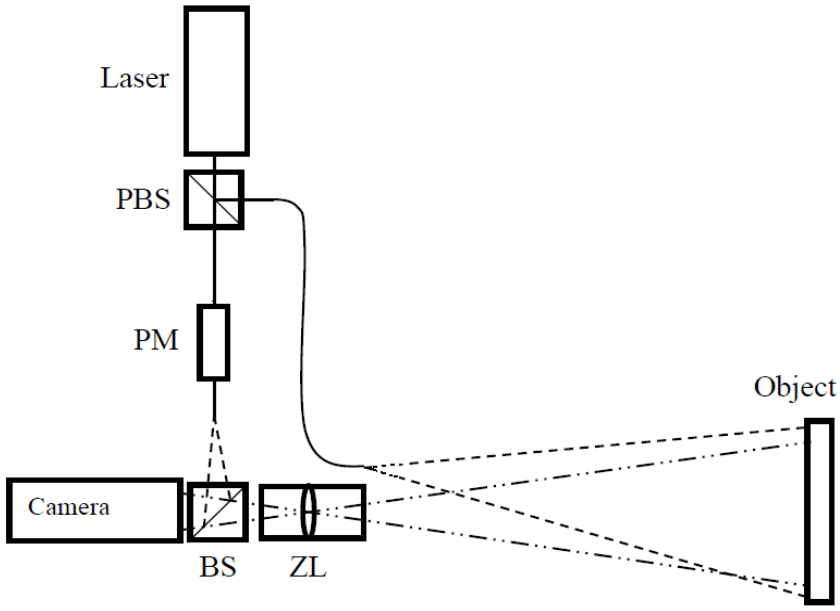

Fig. 5.1. Schematic of the experimental setup. PBS, polarizing beam splitter; PM, phase modulator; BS, beam splitter, and ZL zoom lens.

Some changes with respect to the previous system were incorporated:

- The new custom MLC CMOS camera.
- Removal of the Polarizer at the input of the phase modulator.

The output from a diode-pumped, frequency-doubled Nd:YVO laser (single frequency CW output at 532 nm at power levels up to 5 W) was divided by a polarizing beam-splitter (PBS) into orthogonally linearly polarized object and reference beams. Each beam was then launched into the fast axis of separate highly birefringent optical fibres. The output power of the laser was restricted to 500 mW in order to not damage the proximal fibre ends, particularly of the object beam fibre. The beam-splitter (PBS) and fibre launches could be rotated together as a unit about the axis of the laser beam in order to vary the intensity ratio between the object and reference beams; usually 70% of the laser's output was launched in the object beam fibre. Light from the object fibre illuminated the test object directly. The distal end of the object fibre was rotated by 90° about its optical axis to align its fast axis (and hence the linear polarization of the emerging light) with that of the reference fibre. The test object is a centrally pinned 14 cm diameter circular aluminium plate with retro-reflective coating, driven by a piezoelectric element attached to its rear face.

The object was imaged by a photographic zoom lens onto the 64x64 elements array of the CMOS camera. Light from the reference fibre was collimated, passed through an electro-optic phase modulator (PM), and then re-launched into a fibre to path match the object beam.

The phase modulator generates a phase step by utilizing the fact that the refractive index of the electro-optic material depends on the electric field applied to it. Up to 20 GHz modulation bandwidth was reported, so it is suitable for high-speed measurement. The TTL output of a SWG was used to generate the frequency F_{Mod} that the camera needs to be locked onto; once it is locked-in, the camera generates a sampling frequency f_s that is four times faster than F_{Mod}. The TTL signal was also sent to a frequency multiplier, whose output signal frequency matches the frequency f_s; this signal was then sent to a staircase waveform generator that generates a staircase voltage with N equal steps, each synchronized to the camera sampling frequency f_s. The staircase voltage was finally passed to the phase modulator amplifier to produce inter-samples phase steps in the reference beam.

A timing chart of the system synchronization is showed in Figure 5.2.

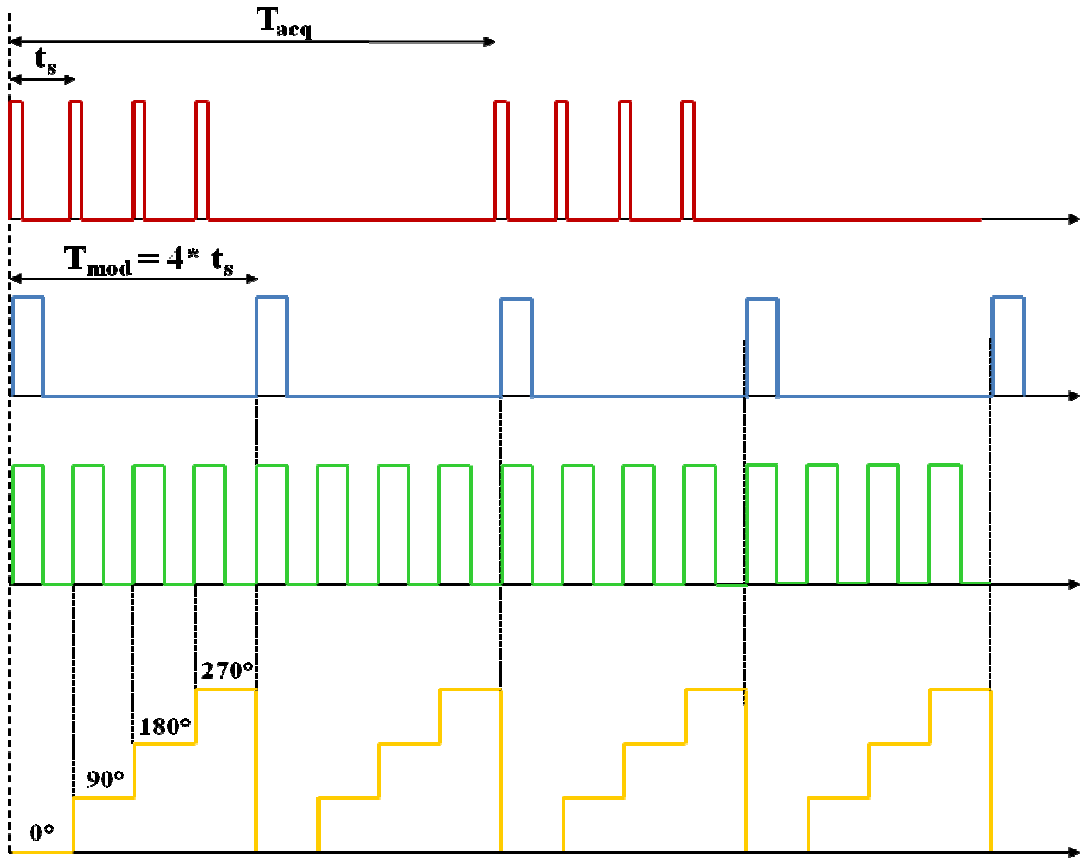

Fig. 5.2. Timing chart of the system synchronization. (a) Camera frame and acquisition period, (b) Modulation frequency $F_{mod}=f_s/4$ generated by the TTL output of the SWG and locked-in by the camera, (c) Trigger generated by the frequency multiplier and sent to staircase waveform generator and (d) staircase waveform generator output.

Initial experiments revealed that the intensity of the reference beam fluctuated considerably when different voltages were applied to the phase modulator as show in Figures 5.3 (a) and (b). The error bars show the standard deviations about the mean for each frame acquired. This issue was also reported in a previous work using the same equipment [35] and it was attributed to leakage of an orthogonally polarized component from the polarizing beam-splitter PBS, propagating in the slow axis of the reference fibre. This unwanted component was amplitude modulated when it passed through the phase modulator, thus generating a fluctuation of the intensity. It was also reported by the author that inserting a linear polarizer before the phase modulator, in order to remove the leaked component, had been successful in solving this issue. However this solution did not lead to any significant improvement in our setup and the fluctuation was estimated approximately the 12% of the DC intensity detected when no voltage was applied to the phase modulator.

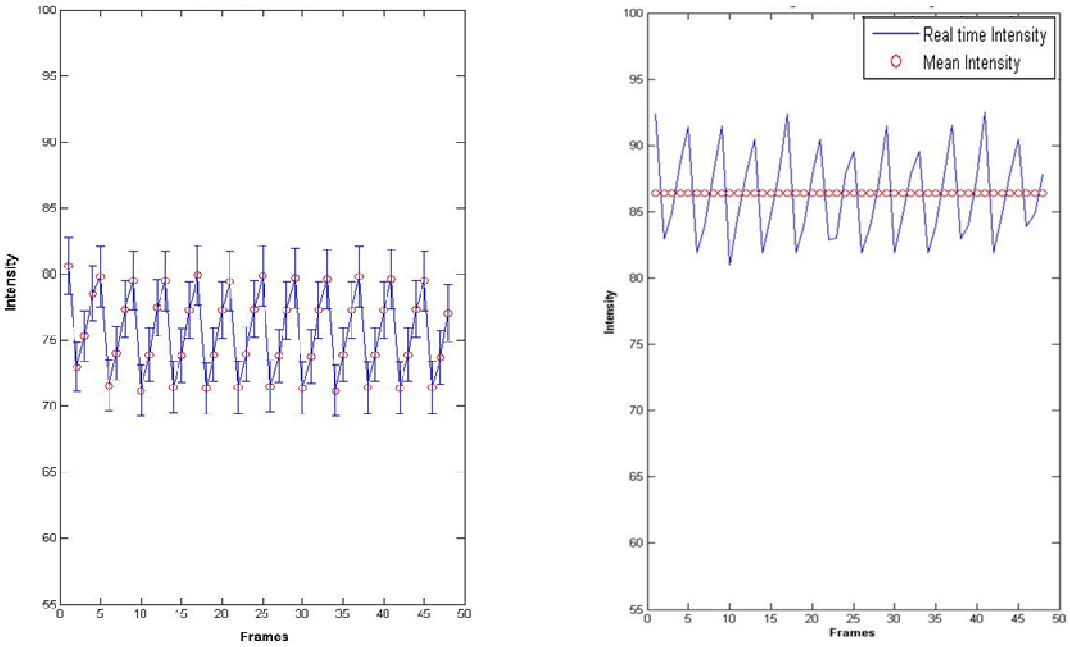

(a) (b)

Fig. 5.3 (a) Reference beam average intensity variation measured at the output of the phase modulator when different voltages are applied. (b) Reference beam intensity variation measured at one pixel only and DC light detected when no voltage is applied to the PM.

Further tests were conducted to determine the nature of this fluctuation:

- Independent measurements of the fluctuation by using the actual setup and a single pixel diode detector, whose output voltage is proportional to the light illuminating the pixel.
- A Mach-Zehnder interferometer was set to allow an easier adjustment and real time monitoring of the phase modulator alignment. Fibres were removed, a different laser and PBS were used and a half wave plate was inserted at the input of the phase modulator. The retarder plate allowed a very fine alignment of the linear polarization of the laser beam with the phase modulator optical axis, whereas changing the bulk optics eliminated the issue related to the propagation of an unwanted component into the phase modulator.

The first test confirmed the fluctuation of the reference beam and its amplitude. In the second experiment a static fringe pattern was projected on the single pixel detector when no voltage was applied. Then a sinusoidal voltage with a frequency of 1 Hz, was applied to the phase modulator, and the shift in the fringe pattern was observed, accordingly to the

phase modulation applied. Despite the good quality of the phase modulation applied, a fluctuation of the intensity still arose. The amplitude of this fluctuation was reduced in the range of [4%, 10%] of the DC intensity detected and it did not match the sinusoidal voltage driving the modulation. Indeed the temporal evolution of the oscillation was found to be strongly dependent on the time of usage of the device. This means that the initial characterization of this fluctuation as a residual amplitude modulation (RAM) cannot be confirmed. A RAM [82], due to either an unwanted orthogonally polarized component or simply an incorrect setup alignment, would be described by:

$$RAM(t) = [1 + m(t)] \cdot c(t) \qquad (5.1)$$

, where m(t) is the modulating signal and c(t) is the carrier, i.e. the DC light detected. This validates the statement that a RAM would have the same temporal evolution as the modulating signal, i.e. sinusoidal, for the particular case considered.

Instead the hypothesis of a Fabry - Perot effect generating the fluctuation, with the phase modulator working as an optical cavity, was found successful in explaining the nature of the oscillation. Multiple reflections were observed from the input of the phase modulator oscillating at the same frequency of the modulating signal, thus leading to the conclusion that the phase modulator input was not perfectly AR coated. Figure 5.4 shows how the Fabry – Perot effect can generate an interference signal at the output of the phase modulator.

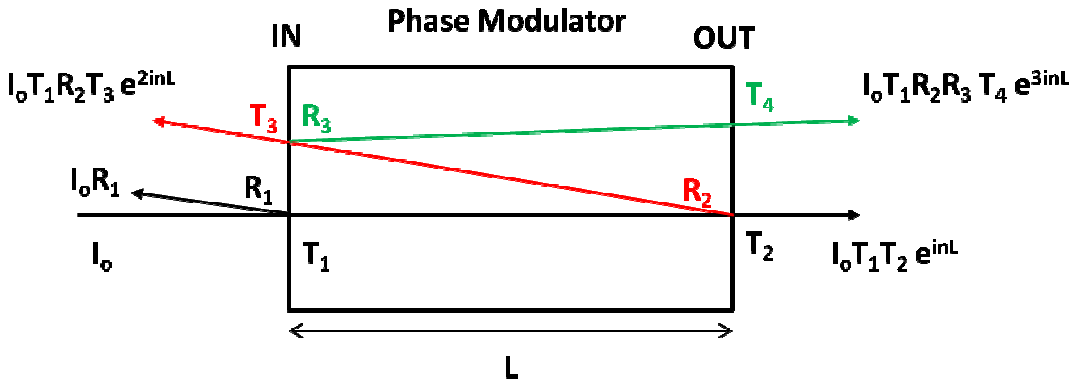

Fig. 5.4. I_o – Beam entering the phase modulator. T_1, T_2, T_3, T_4 – Transmission Points. Other points exist but they are considered negligible. R_1, R_2, R_3 – Reflection Points. Other points exist but they can be considered negligible.

The signal transmitted from T_2 represents the main part of the output signal, whereas the fluctuation observed is generated by the interference between the signal transmitted from T_2 and the signal transmitted from T_4.

The reduction of the fluctuation obtained by removing the fibres and the old unit, containing the PBS and fibre launches, jointly with the need to increase the quantity of light illuminating the CMOS camera (as mentioned in section 4.1), led to the new experimental setup shown in Figure 5.5.

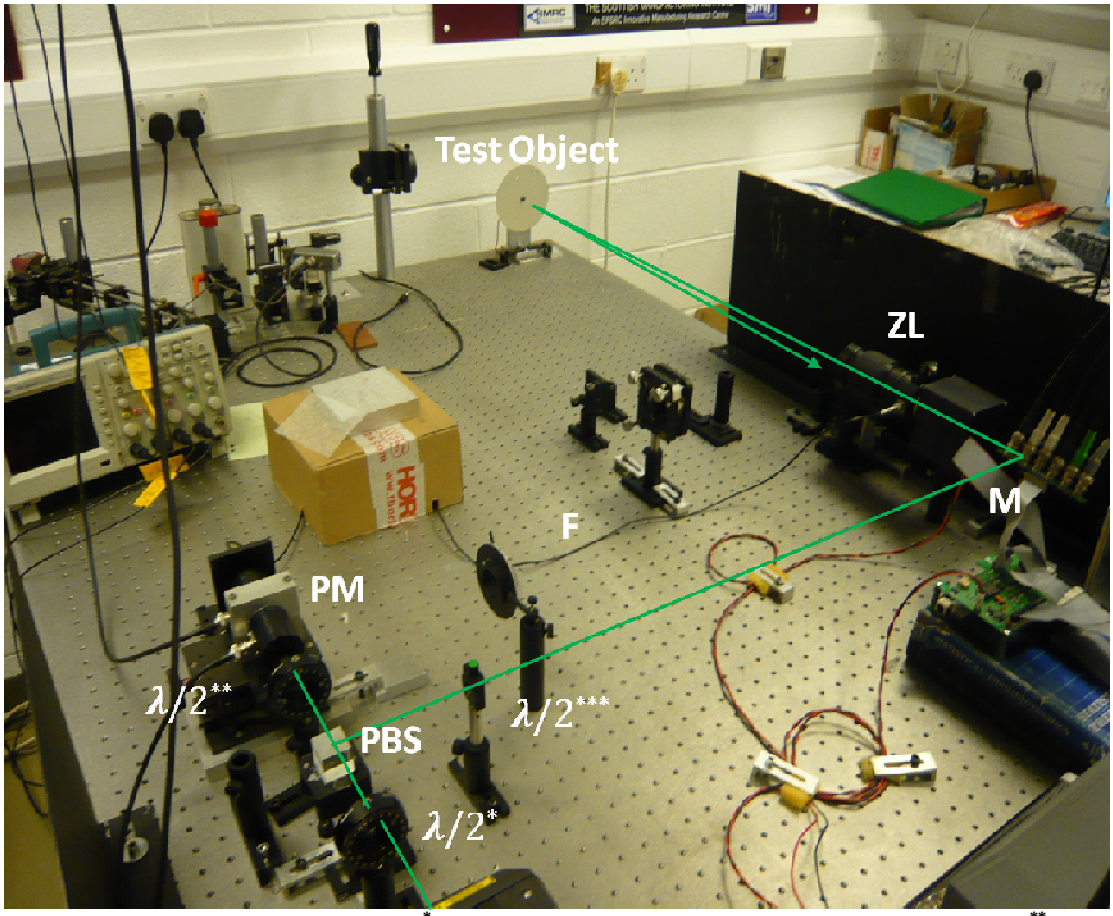

Fig. 5.5. New experimental setup. $\lambda/2^{*}$, Half wave plate; PBS, polarizing beam splitter; $\lambda/2^{**}$, Half wave plate; PM, phase modulator; $\lambda/2^{***}$, Half wave plate; F, reference beam fibre; ZL zoom lens; M, mirror.

We obtained the following improvements:

- $\lambda/2^{*}$ Half wave plate enables an easier and quicker change of the ratio between the reference and object beams.
- The new PBS doesn't have any leakage of unwanted components. This enables:

    - The possibility to have an almost perfectly linearly polarized beam at the input of the phase modulator.
    - A higher visibility of the interference signal. The Reference beam is now fully linearly polarized, i.e. the full power of the reference beam interferes with the object beam, without waste of power in useless components.
- $\lambda/2^{**}$ Half wave plate enables a finer alignment of the beam polarization with the optical axis of the PM.
- The total amount of light of both object and reference beams is boosted allowing the camera to detect more light.

The following sections refer to experimental works performed by using the above mentioned optical setup.

5.2 Time-averaged SPI

Time averaged subtraction fringe patterns were recorded for the test object vibrating harmonically at different natural frequencies. Due to the small array dimensions, first imaging the whole test target into a larger array was found necessary; then the MLC detector was focused on a smaller ROI. Figure 5.6 shows time-averaged fringe patterns recorded with a CCD camera working at 30 fps (AVT Marlin F-145B2, 1024x1024 pixels) for the 14 cm circular test target vibrating at different frequencies. A sequential subtraction analysis, with the reference frame constantly refreshed, was performed in order to eliminate environmental noise below the detector frame rate. The best ratio between the reference and the object beam was achieved by rotating the $\lambda/2^{*}$ half-wave plate, thus enabling the achievement of a good interference visibility accordingly to:

$$I(x,y) = I[1 + V\cos(\psi)J_o\left(\frac{2\pi w_o}{\lambda}\right)] \qquad (5.2)$$

$V = \frac{2\sqrt{I_o I_r}}{I}$ is the visibility of the interference and it achieves its maximum value, that is unity, only if the two combining beams have equal intensity and state of polarization at camera image plane.

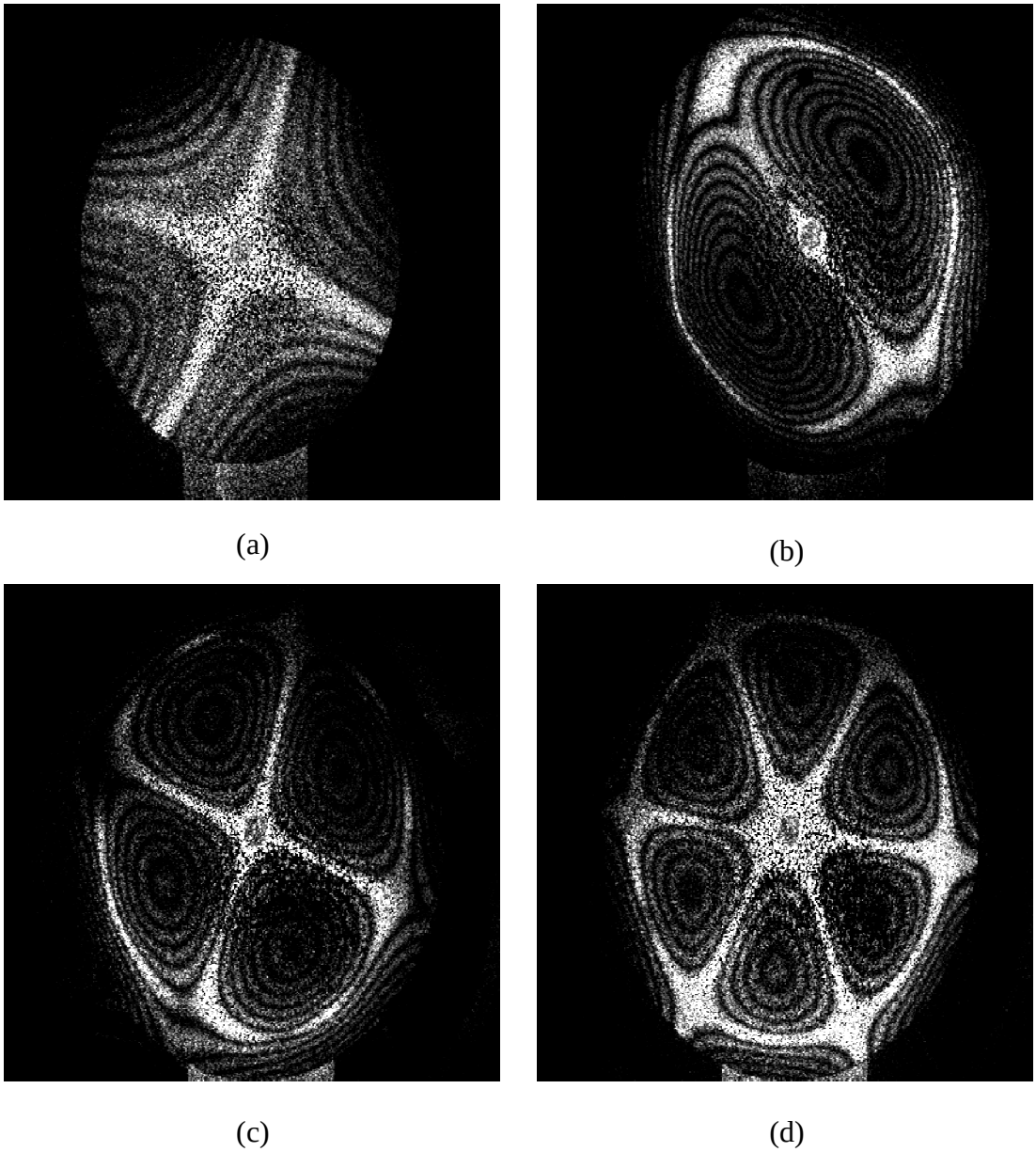

(a) (b)

(c) (d)

Fig. 5.6. Time averaged subtraction fringe patterns recorded at 25 fps for a test object vibrating at (a) 225 Hz, (b) 1100 Hz, (c) 1600 Hz, (d) 2400 Hz

The time averaged subtraction fringe pattern, which was obtained when the object harmonically vibrated at 225 Hz, was taken in consideration for reasons that will be explained in the next section.

The plate was rotated to obtain the fringe pattern shown in Figure 5.7 (a); then a smaller area, identified by the square, was hence imaged on the CMOS detector as shown in Figure 5.7 (b).

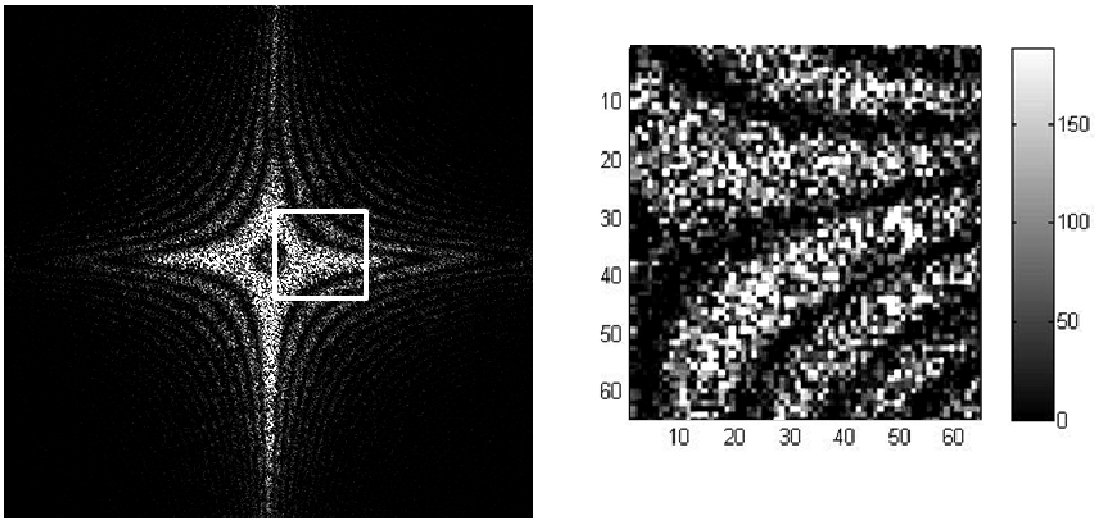

(a) (b)

Fig. 5.7 (a) Time averaged subtraction fringe patterns recorded at 25 fps with the Marlin camera for a test object vibrating at 225 Hz. The square denotes a smaller area imaged on the MLC camera (b).

The lower resolution of the fringes obtained with the MLC camera was attributed to the different size of the two camera pixels. A schematic of the MLC pixel design is shown in Figure 5.8. The pixel area is 30 μm x 30 μm with a fill factor of 35%, thus leading to a detecting pixel area of 10.5 μm x 10.5 μm. Instead the AVT Marlin camera pixels have an area of 10 μm x 10 μm with a filling factor close to the 80%.

The consequences of having bigger pixels and using a bigger lens aperture imaging the speckle pattern (f/2.8 was used rather than f/22 to increase the available light illuminating the array), were investigated.

Mathias Lehmann [83] investigated the influence of the imaging aperture to determine a measurement optimization in speckle interferometry. It was demonstrated that resolving the speckle grains in the image is far from necessary, as widely believed in the early years of speckle interferometry. Optimum modulation distribution could be obtained if a large number (but not exceeding the number of twenty) of speckles were integrated by camera pixels. Other authors [84] determined the optimum speckle size to be used in an electronic speckle pattern. They demonstrated that fringes were obtained with high contrast and low speckle noise, if the speckle size was selected by the optical system so as to be smaller

than the pixel size; additionally the in plane displacement of the test object had to be small.

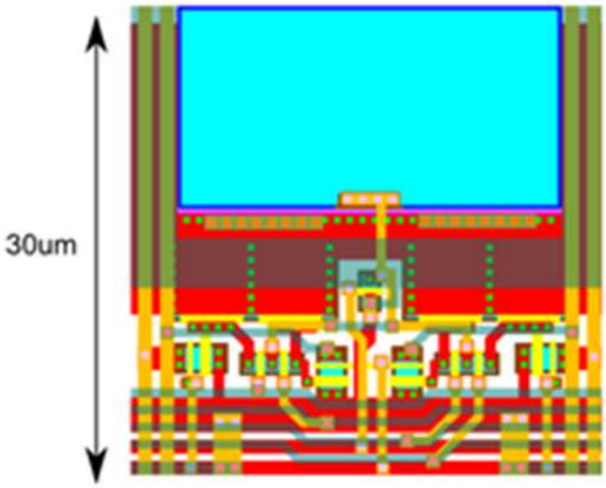

Fig. 5.8. Single pixel design of the MLC. The pixel area is 30 µm x 30 µm with a fill factor of 35%. The blue section represents the light sensitive region of the pixel. The electronics implementing the readout circuitry is also shown.

The subjective speckle size in our system was calculated according to:

$$\sigma = \frac{\lambda f}{D_a} = 1.5\ \mu m \tag{5.3}$$

, meaning that approximately 8 speckles are imaged in each pixel. This enabled the conclusion that the dimension of pixels and the aperture of the lens used in our system satisfied the requirements to obtain well resolved fringes and low speckle noise.

5.3 Vibration map of the test object by scanning a SPLV

The time averaged patterns shown in Figure 5.7 were used to identify ROIs, and then to interrogate them at a higher frame rate for time resolved measurements. A maximum frame rate corresponding to 7 kfps (further details will be explained in the next section) could not be exceeded, thus considerably restricting the maximum velocity of the vibration that could be measured reliably. Figure 5.7 (a) shows a resonance fringe pattern for a test object vibrating harmonically at 225 Hz and with an amplitude corresponding to a velocity of vibration equal to $V = 0.3\,V_{Nq}$. When lower amplitudes of vibration are considered, enabling velocities on the order of $V = 0.05\,V_{Nq}$, the dimensions of the zero order fringe become dominant over the whole fringe pattern not allowing to determine whether the test object is still harmonically vibrating or not.

For this reason an analysis of the vibration properties of the test object at low velocities, using an alternative method of measurement, was found necessary. Different velocities of vibration were applied to the test object and were measured by scanning a single point laser vibrometer (SPLV) across vertical sections of the object as shown in Figure 5.9 (b).

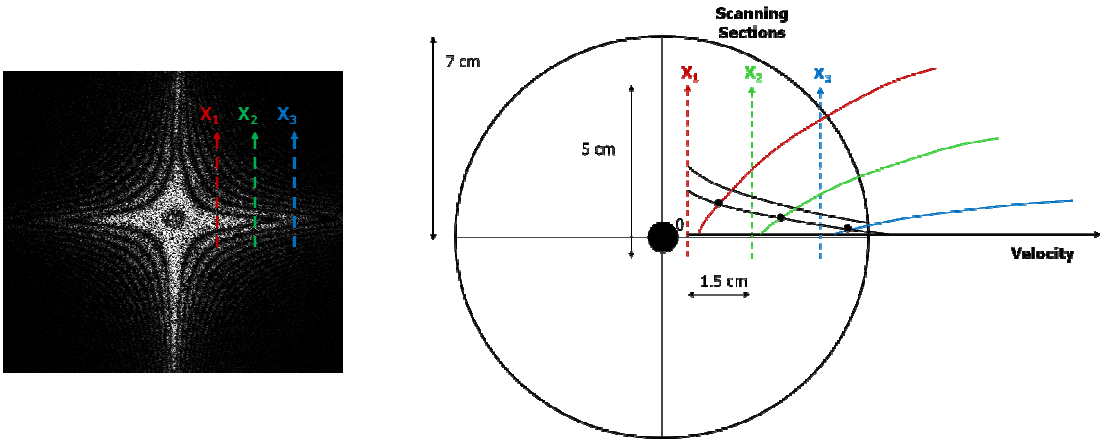

(a) (b)

Fig. 5.9 (a) Time averaged subtraction fringe patterns recorded at 25 fps with the Marlin camera for a test object vibrating at 225 Hz and V=0.3V_{Nq}. An example of the choice about the position of the scanning sections is also shown. (b) Schematic of the scanning procedure used. Examples of the expected velocity profiles and contours of equal displacement are shown.

Three cases were analyzed, corresponding to $V = 0.1\,V_{Nq}$, $V = 0.3\,V_{Nq}$ and $V = 0.5\,V_{Nq}$; the velocities are obtained by increasing the amplitude of the vibration while maintaining the same vibration frequency. Maps of the velocity profiles were retrieved in every case

of study and then compared. Figure 5.10 shows the velocity profile retrieved by scanning the single laser point vibrometer across section X_1.

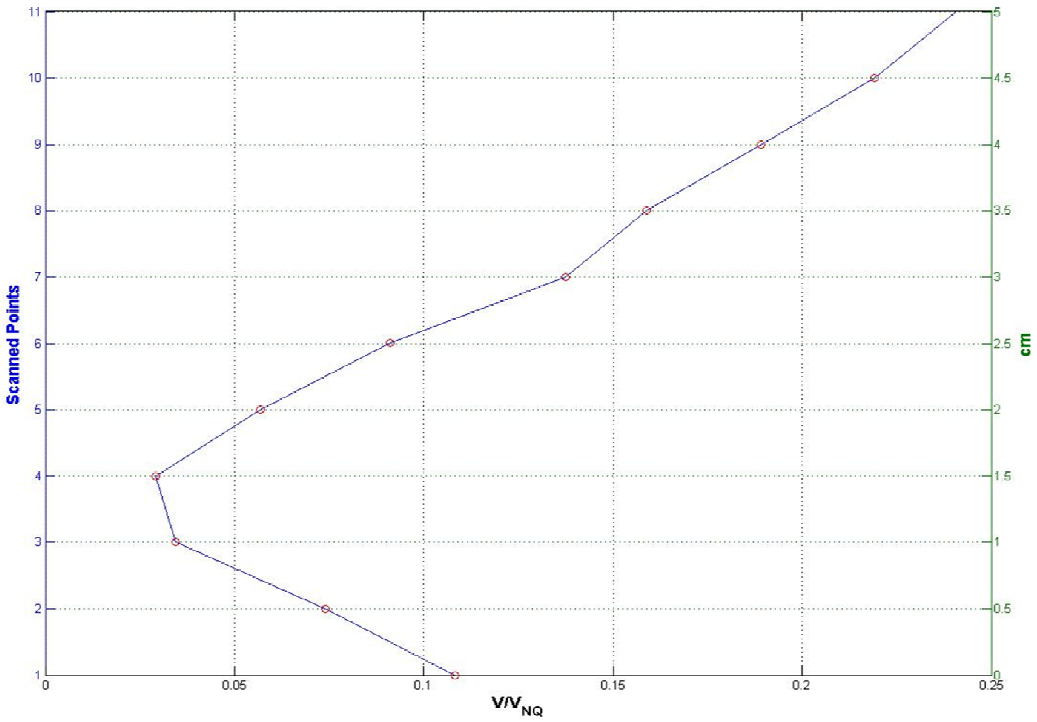

Fig. 5.10. Normalized velocity measured across the section X_1. The voltage output of the single point laser vibrometer at each point, was transformed in an equivalent velocity value accordingly to the data sheet of the instrument.

Eleven measurement points were taken across the section, with each point equally spaced by 0.5 cm. The first measurement point was chosen below the theoretical position of an axis dividing the first quadrant from the second one. The axis position was approximately between the third and the fourth measurement point. This choice enabled the display of the velocity profile in the second quadrant, thus validating its symmetry with respect to the nodal axis. A reference velocity $V = 0.1\, V_{Nq}$ was chosen at the first measurement point; the velocity decreases correctly close to the nodal axis and then it gradually increases in the external part of the test object.

Monitoring of the phase of the velocity measured versus the phase of the signal driving the PZT, was also performed. This was found necessary in order to determine if any unwanted drift, or complex change of the phase of velocity, arose across the scanned section. Figure 5.11 shows the velocity measured at one measurement point and the output signal of the SWG driving the PZT.

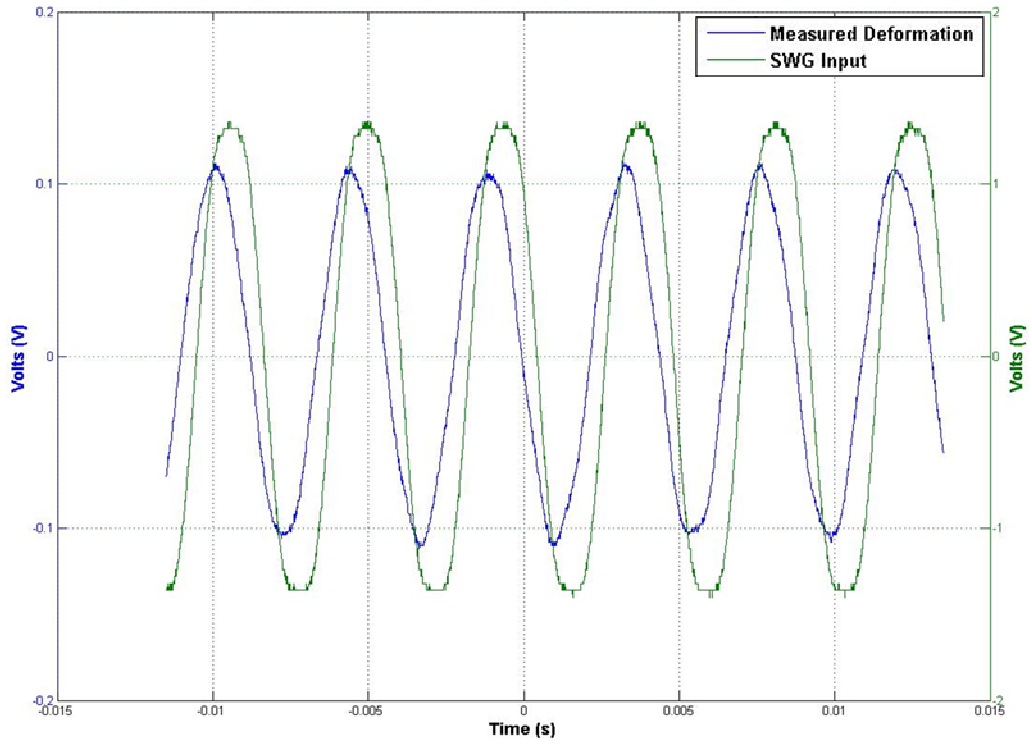

Fig. 5.11. Voltage output of the single point laser vibrometer at one measurement point and the driving signal generated by the SWG.

The phase of the two signals was calculated using the Takeda DFT [85]. Each of the two signals shown in Figure 5.11 can be described by:

$$g(t) = \mathrm{c(t)}\exp(\mathrm{i2\pi f_0 t}) + \mathrm{c^*(t)}\exp(-\mathrm{i2\pi f_0 t}) \tag{5.3}$$

with

$$c(t) = (a/2)\exp(i\phi(t)) \tag{5.4}$$

The signals were Fourier transformed by the use of a FFT algorithm giving:

$$G(f) = C(f - f_0) + C(f + f_0) \tag{5.5}$$

We made use of one of the two spectra, say $C(f + f_0)$, and we translated it by f_0 on the frequency axis toward the origin to obtain $C(f)$; again using the FFT algorithm, we

computed the inverse Fourier transform of $C(f)$ with respect to f and we obtained c (t). Then we calculated a complex logarithm of Equation 5.4:

$$\log [c(t)] = \log [(a/2)\exp (i\phi(t))] \quad (5.6)$$

, thus obtaining the phase of the signals modulo 2π. Figure 5.12 shows the wrapped phases of the signals in Figure 5.11.

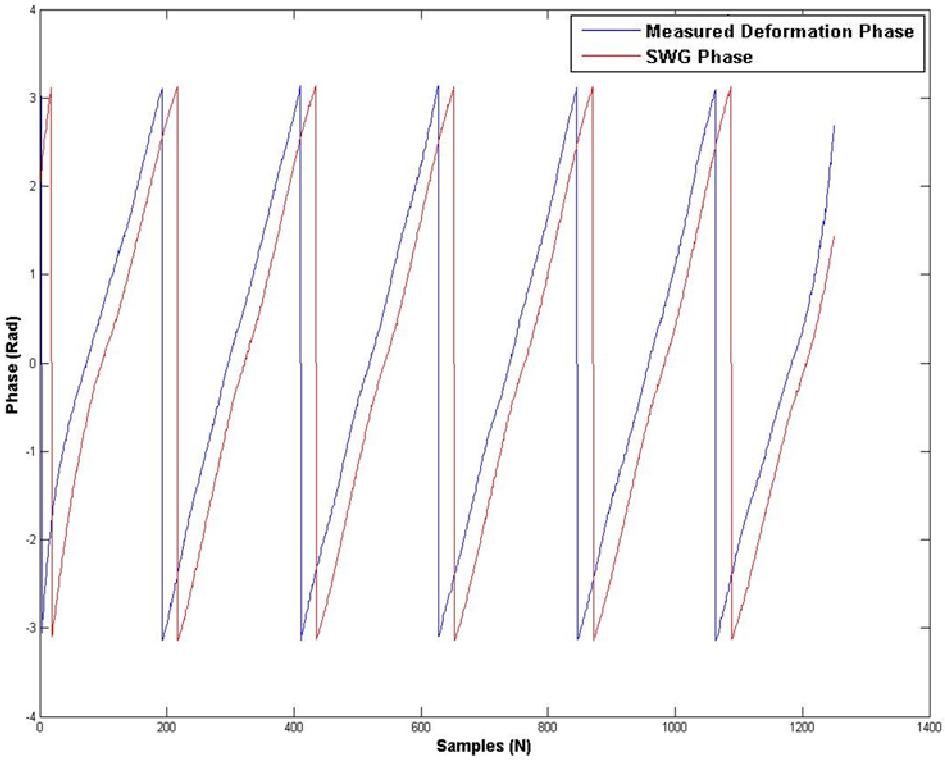

Fig. 5.12. Wrapped phases of the velocity of the vibration measured and signal generated by the SWG.

Finally the phases were unwrapped and their difference could be calculated leading to results shown in Figure 5.13. The difference is constant with a standard deviation of about 8°, which can be considered negligible. The computation of the phase difference was repeated for each of the measurement points across the section $X_{1,}$ thus leading to results shown in Figure 5.14. An average of the phase difference was calculated at each measurement point in order to display the phase change across the section $X_{1,}$ as shown in Figure 5.13.

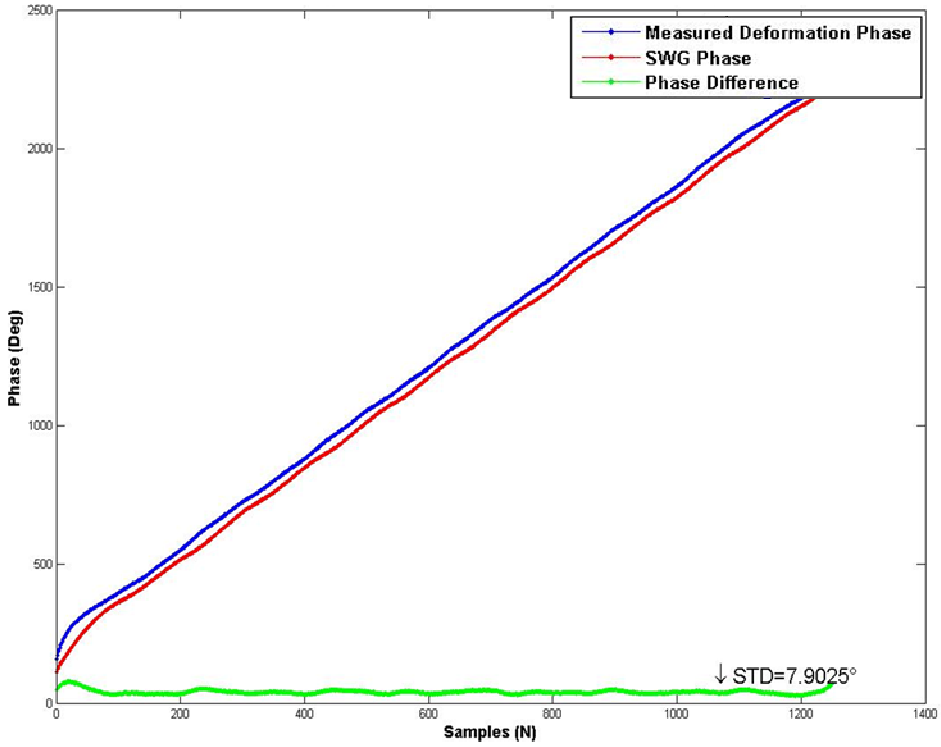

Fig. 5.13. Unwrapped phases of the velocity of the vibration measured and signal generated by the SWG. The difference of the two phases is also shown.

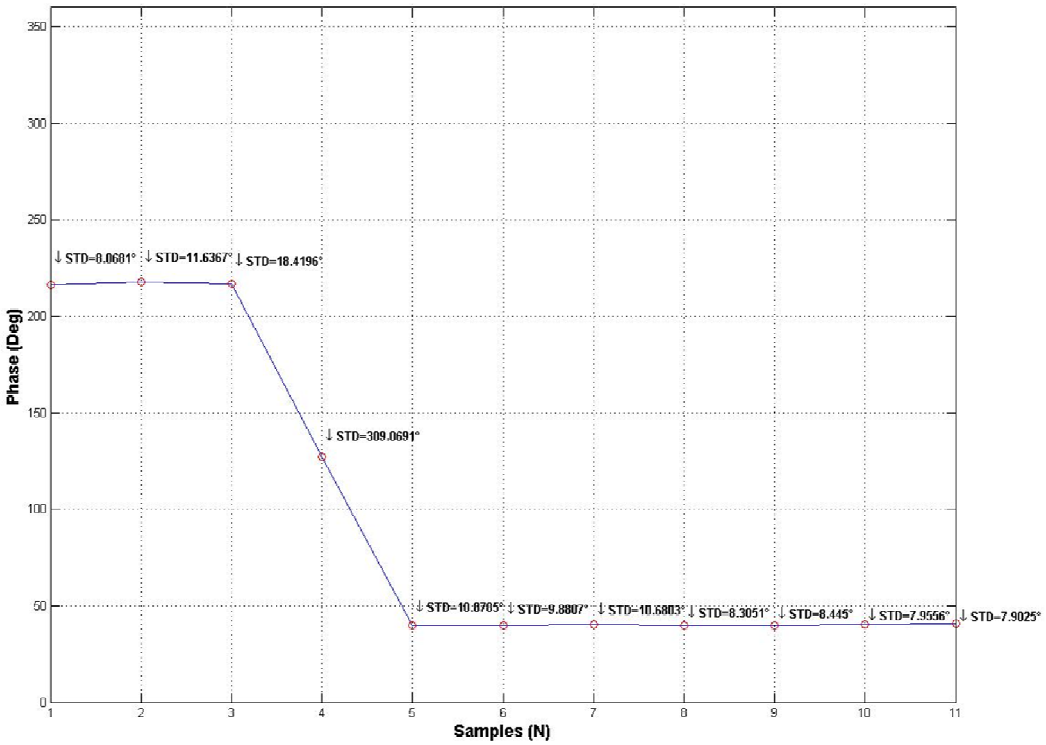

Fig. 5.14. Unwrapped average phase difference across section X_1 of the test object. The standard deviation of the phase difference at each measurement point is also shown.

The phase difference is constant at most of the measurement points, whereas it considerably changes between the third and the fifth points. This was expected because of the inversion in the phase of the velocity from the first quadrant to the second quadrant. This leads to a decrease of 180° in the phase difference.

Then the other sections X_2 and X_3 were scanned, by maintaining the same reference velocity used for scanning the section X_1; the velocity profiles measured are shown in Figure 5.15.

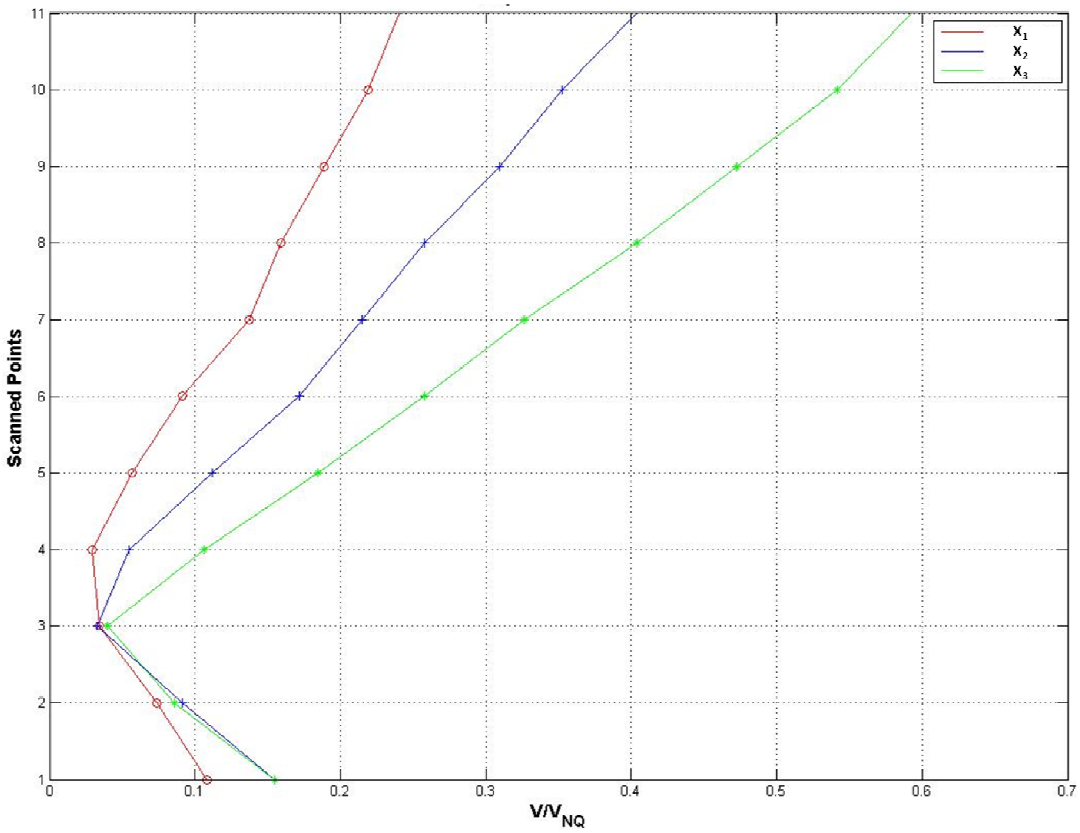

Fig. 5.15. Normalized velocities measured across the sections X_1, X_2, X_3. The voltage output of the single point laser vibrometer at each point, was transformed in an equivalent velocity value accordingly to the data sheet of the instrument.

The gradient of the velocity of the vibration gradually increases through the different sections considered, accordingly with a resonance fringe pattern as shown for example in Figure 5.9 (a). The difference between the phase of the retrieved velocity and the phase of the SWG driving signal was calculated also for section X_2 and X_3 and it is shown in Figure 5.16. The inversion in the phase of the velocity, due to the crossing of the nodal fringe becomes more unpredictable in section X_2 and X_3; this was attributed to the narrowing of the zero order fringe that arises by moving from section X_1 to section X_3.

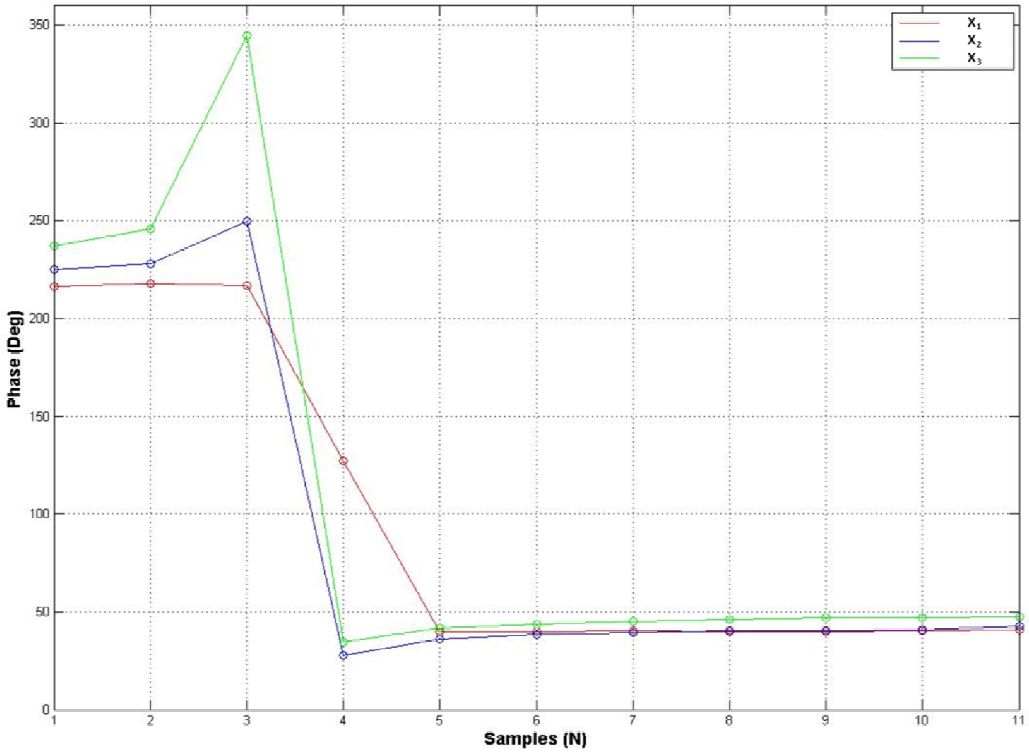

Fig. 5.16. Unwrapped average phase differences across sections X_1, X_2, X_3 of the test object.

The same study was repeated by increasing the reference velocity of the vibration at the first measurement point of section X_1, and then by scanning the single point laser vibrometer across the sections, as previously mentioned. Results agreed with the investigation so far produced and they are summarized in Figure 5.17.

Finally, Figure 5.18 (a) shows the velocity profiles measured across section X_2, when different reference velocities used. These results were used to set a velocity of vibration lower than 0.07 $V_{Nq,}$ in the area of the test object imaged by the MLC camera.

The results of this analysis revealed that the test object vibrates harmonically for velocities that are higher than approximately 0.03 V_{Nq}. When lower velocities are set, the velocity profile retrieved by the instrument is no longer harmonic. Figure 5.19 (a) shows the lowest harmonic velocity that could be measured, corresponding to 30μm/s (i.e. V=00.3 V_{Nq}), whereas Figure 5.20 (b) shows a measured velocity corresponding to 20 μm/s (i.e. V=00.2 V_{Nq}), which is no longer harmonic.

The noise-limited resolution of the single point laser vibrometer, is defined as the signal amplitude (rms) at which the signal to noise ratio is 0 dB with 1 Hz of spectral resolution.

So we can define R, i.e. the system resolution, as a spectral density in rms volts per root Hertz:

$$R = 0.2\frac{\frac{\mu m}{s}}{\sqrt{Hz}} = 3.16\frac{\mu m}{s} \tag{5.7}$$

Since the resolution of the instrument would enable measurement of such a low velocity of vibration, we can conclude that the vibration of the test object is no longer harmonic when $V<0.03\ V_{Nq}$.

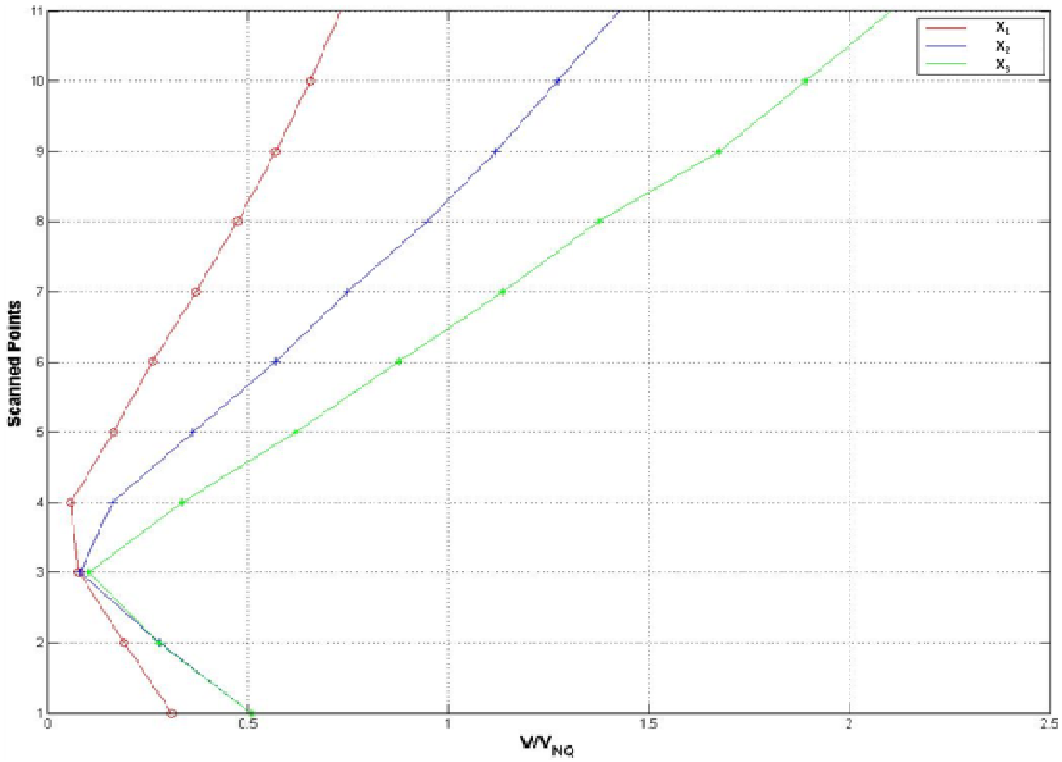

(a)

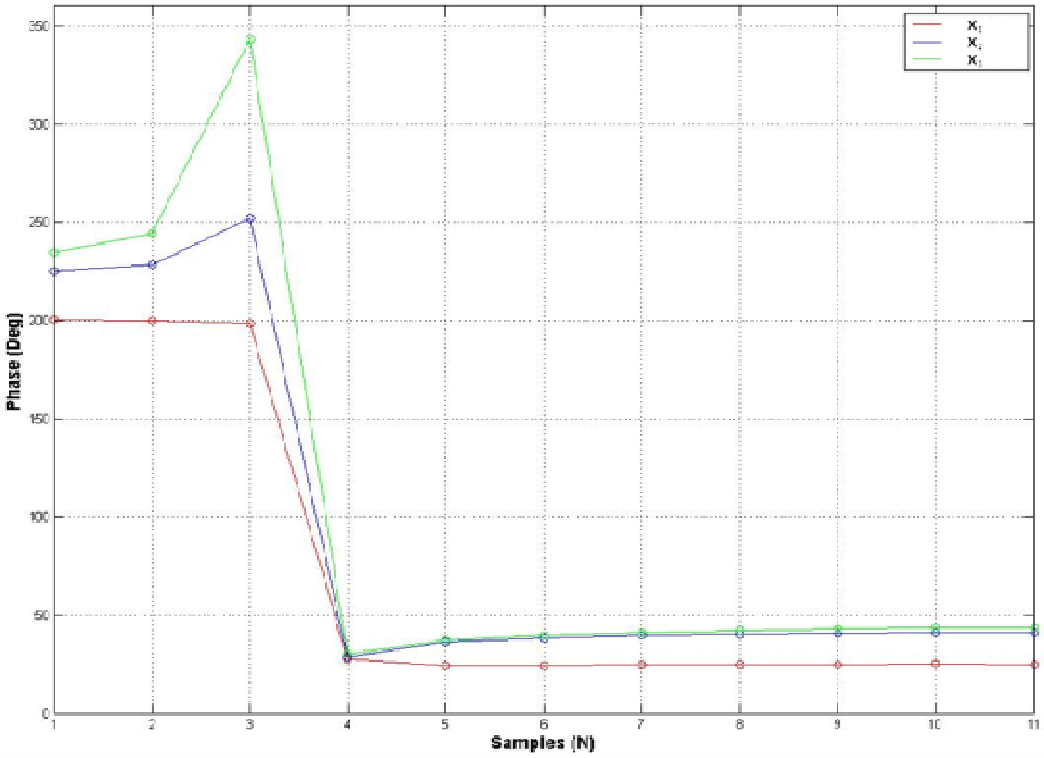

(b)

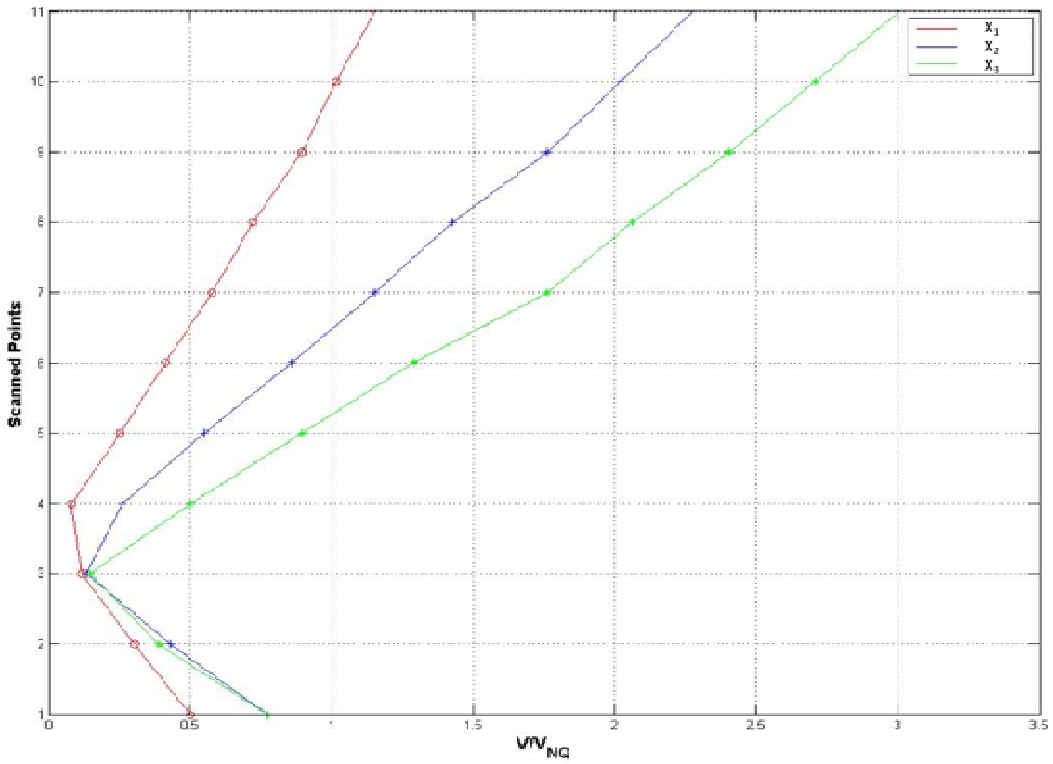

(c)

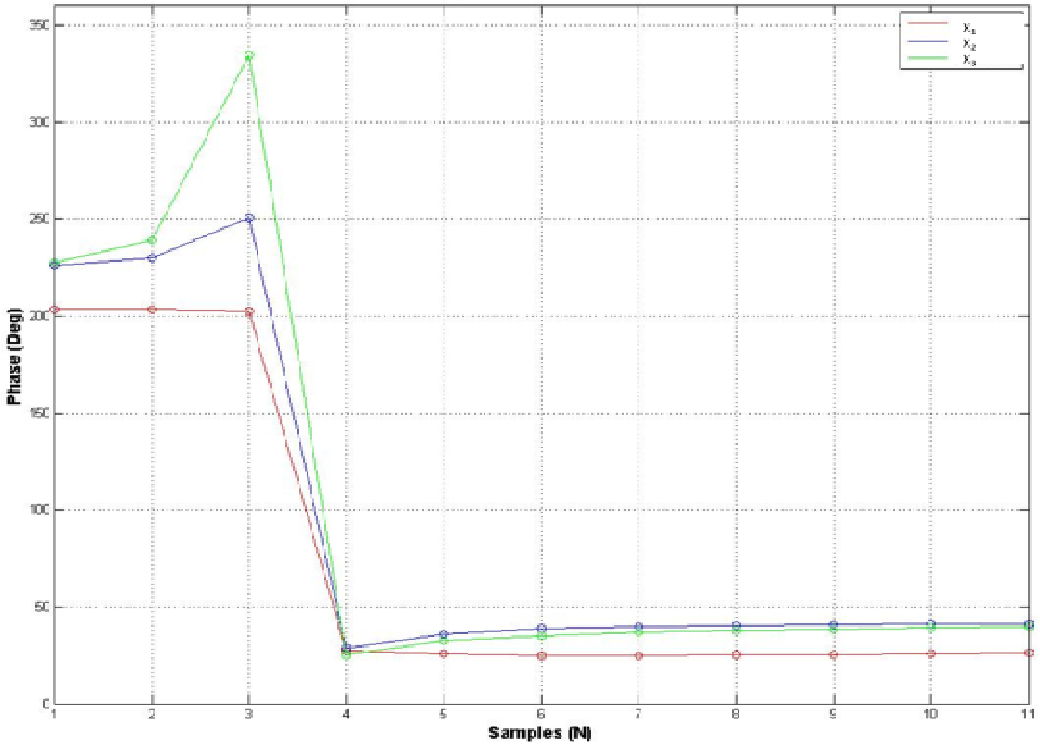

(d)

Fig. 5.17 (a) Normalized velocities measured and (b) unwrapped average phase differences across sections X_1, X_2, X_3 of the test object when a reference velocity of $V = 0.3\,V_{Nq}$ is used. The same results are respectively shown in (c) and (d) when a reference velocity of $V = 0.5\,V_{Nq}$ is used.

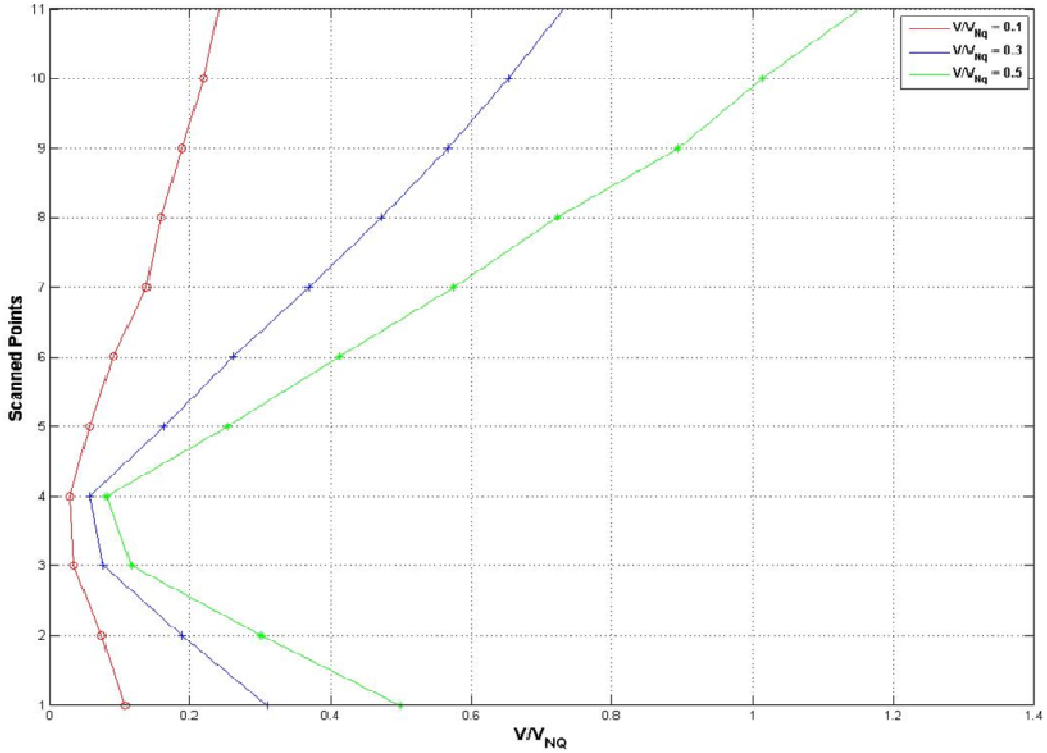

(a)

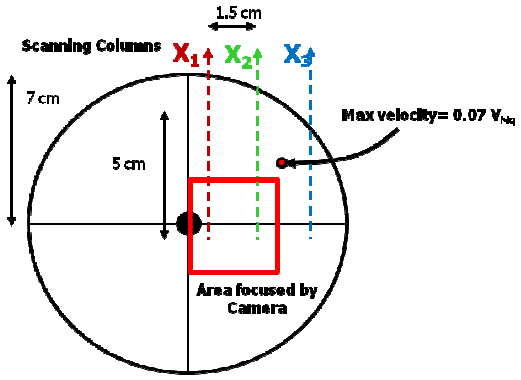

(b)

Fig. 5.18 (a) Normalized velocities measured across section X_2 when $V = 0.1\,V_{Nq}$, $V = 0.3\,V_{Nq}$ and $V = 0.5V_{Nq}$ are chosen as reference velocities. (b) Positioning of maximum velocity.

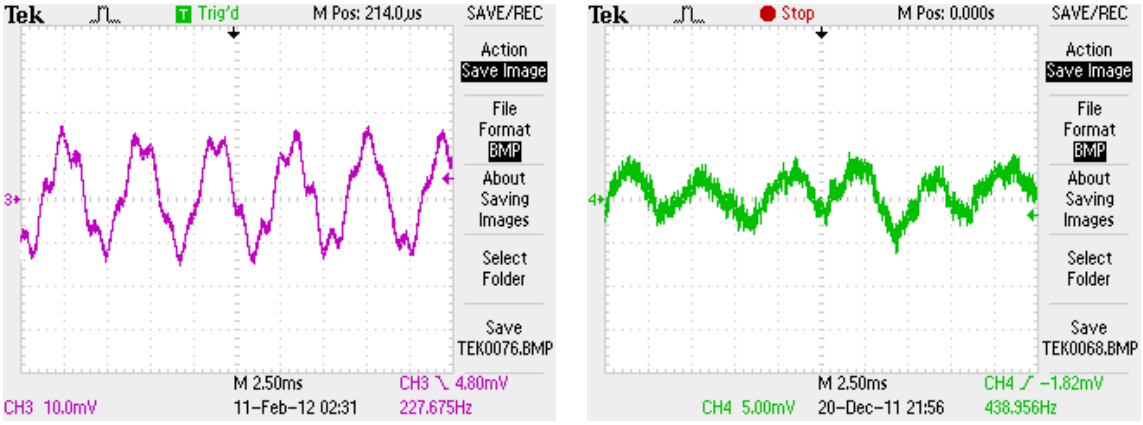

(a) (b)

Fig. 5.19 (a) Lowest harmonic velocity that could be measured and corresponding to 30 µm/s (i.e. V=00.3 V_{Nq}), and (b) measured velocity corresponding to 20 µm/s (i.e. V=00.2 V_{Nq}) that is no longer harmonic.

5.4 Inter-frame phase stepped system

5.4.1 Calibration of phase steps

A calibration of the phase steps applied was performed before measuring the object vibration. Due to delays introduced by the electronics of the SWG and the phase modulator amplifier, the applied phase step might not match exactly the time exposure between frames. In order to reduce this delay, the position of the phase steps was validated by aligning carefully the step transition with the reset time occurring between any two adjacent time exposures. Afterword the optimal position of the phase steps was validated by measuring the interference modulation amplitude introduced by the phase modulation, and calculated at each pixel using the equation[86]:

$$VI(x,y,t_n) = \frac{\{[(I_n - I_{n+1}) + (I_{n-1} - I_{n+2})]^2 + [(I_n + I_{n+1}) - (I_{n-1} + I_{n+2})]^2\}^{1/2}}{2\sqrt{2}} \tag{5.8}$$

Figure 5.20 shows the variation in measured mean modulation amplitude plotted against a variable delay between the camera synchronization signal and the SWG phase steps.

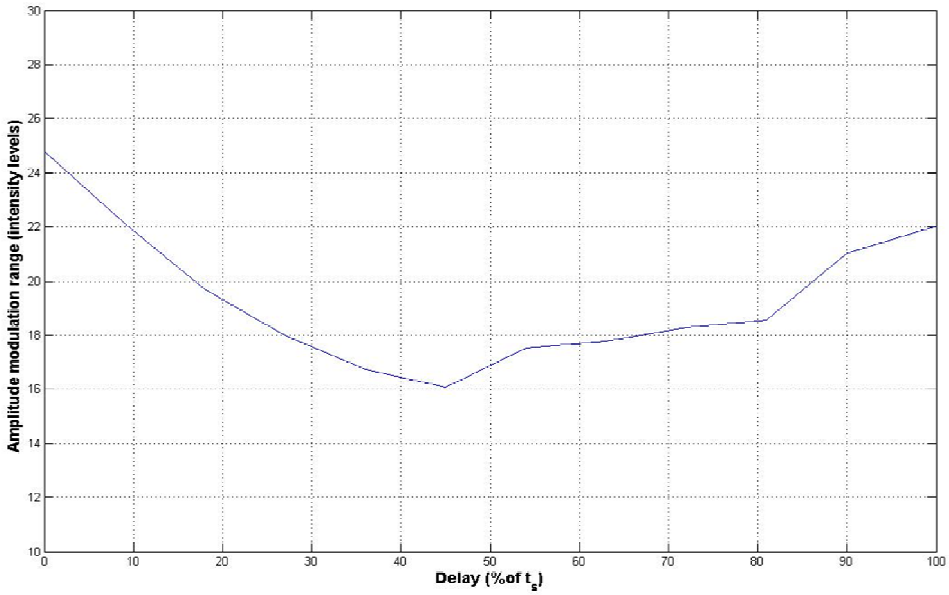

Fig. 5.20. Variation in mean modulation amplitude plotted against delay between frame signal and the applied π/2 phase steps for frames recorded at 7 kHz.

The delay is expressed as a fraction of the camera time exposure t_s. The modulation amplitude is a maximum when the phase steps match perfectly the period between exposures, and a minimum when the steps occur mid-exposure.

The staircase generator gain was adjusted to produce phase steps of $\pi/2$ rads in the reference beam by calculating the phase-step size at each pixel using the equation [32]:

$$\Phi_R(x,y,t_n) = 2\tan^{-1}\sqrt{\frac{3(I_n - I_{n+1}) - (I_{n-1} - I_{n+2})}{(I_n - I_{n+1}) + (I_{n-1} - I_{n+2})}} \tag{5.9}$$

Figure 5.21 (a) shows the variation in mean phase-step size (calculated over all array pixels) for a sequence of phase-stepped samples recorded with the test object stationary, with a sampling frequency $f_s = 3.5\ kHz$ and $F_{Mod} = 900\ Hz$. Over all frames in the sequence, a mean phase step of 89.12° was obtained. Figure 5.21 (b) shows mean phase step size distribution calculated over all frames. The phase difference calculated between successive frames is given by:

$$\Phi_0(x,y,t_n) - \Phi_R(x,y,t_n) - [\Phi_0(x,y,t_{n-1}) - \Phi_R(x,y,t_{n-1})] = \Delta\Phi_0(x,y,t_n) \tag{5.10}$$

where at a given pixel $\Delta\Phi_0(t_n) = \Phi_0(t_n) - \Phi_0(t_{n-1})$ represents the change in phase due to the surface deformation between frames, and $\Phi_R(t_n) - \Phi_R(t_{n-1}) = 0$ is the change in the reference beam phase between frames, i.e. zero as at every frame the Φ_R phase value is equally repeated due to the synchronization described in section 5.1. Figure 5.21 (c) shows the mean phase difference between successive frames (calculated over all pixels) for the same sequence of phase-stepped frames recorded with the test object stationary. Over the whole sequence, a mean phase difference of 0.08° was obtained. Figure 5.21 (d) shows mean phase difference distribution calculated over all frames.

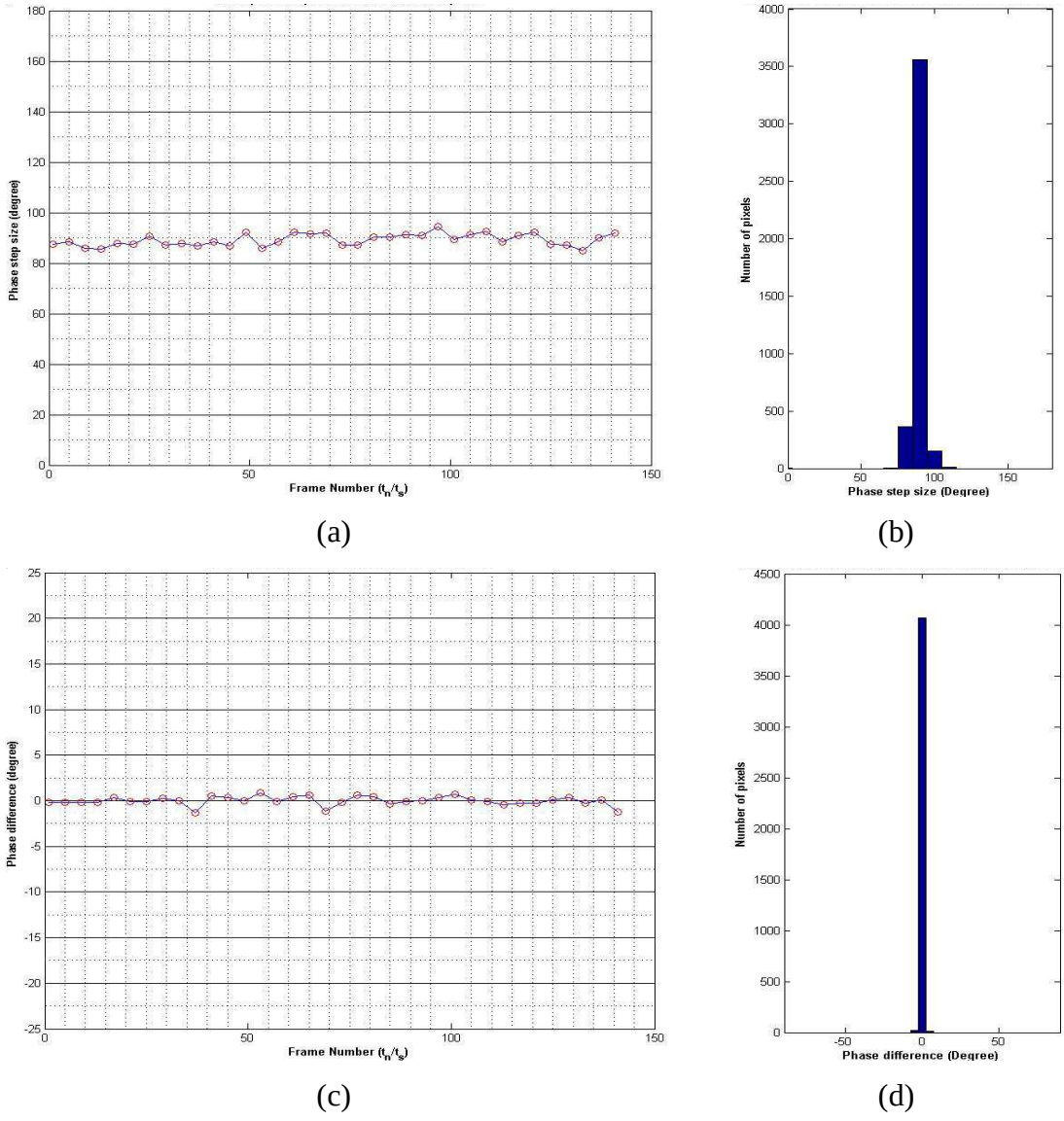

Figure 5.21 (a) Inter-frame phase-step size plotted against the frame number and (b) phase step size distribution for all frames recorded for a stationary object with a sampling rate of 3.5 kHz. (c) Inter-frame phase difference plotted against the frame number and (d) phase difference distribution, for the same image sequences as (a) and (b).

The same measurements were replicated with the only exception of increasing the sampling frequency to $f_s = 7\,kHz$ and $F_{Mod} = 1750\,Hz$. Figure 5.22 (a) shows the variation in mean phase-step size (calculated over all array pixels) for a sequence of phase-stepped samples recorded with the test object stationary. Figure 5.22 (b) shows mean phase step size distribution calculated over all frames. Figure 5.22 (c) shows the mean phase difference between successive frames (calculated over all pixels) for the same sequence of phase-stepped frames recorded with the test object stationary. Figure 5.22 (d) shows mean phase difference distribution calculated over all frames.

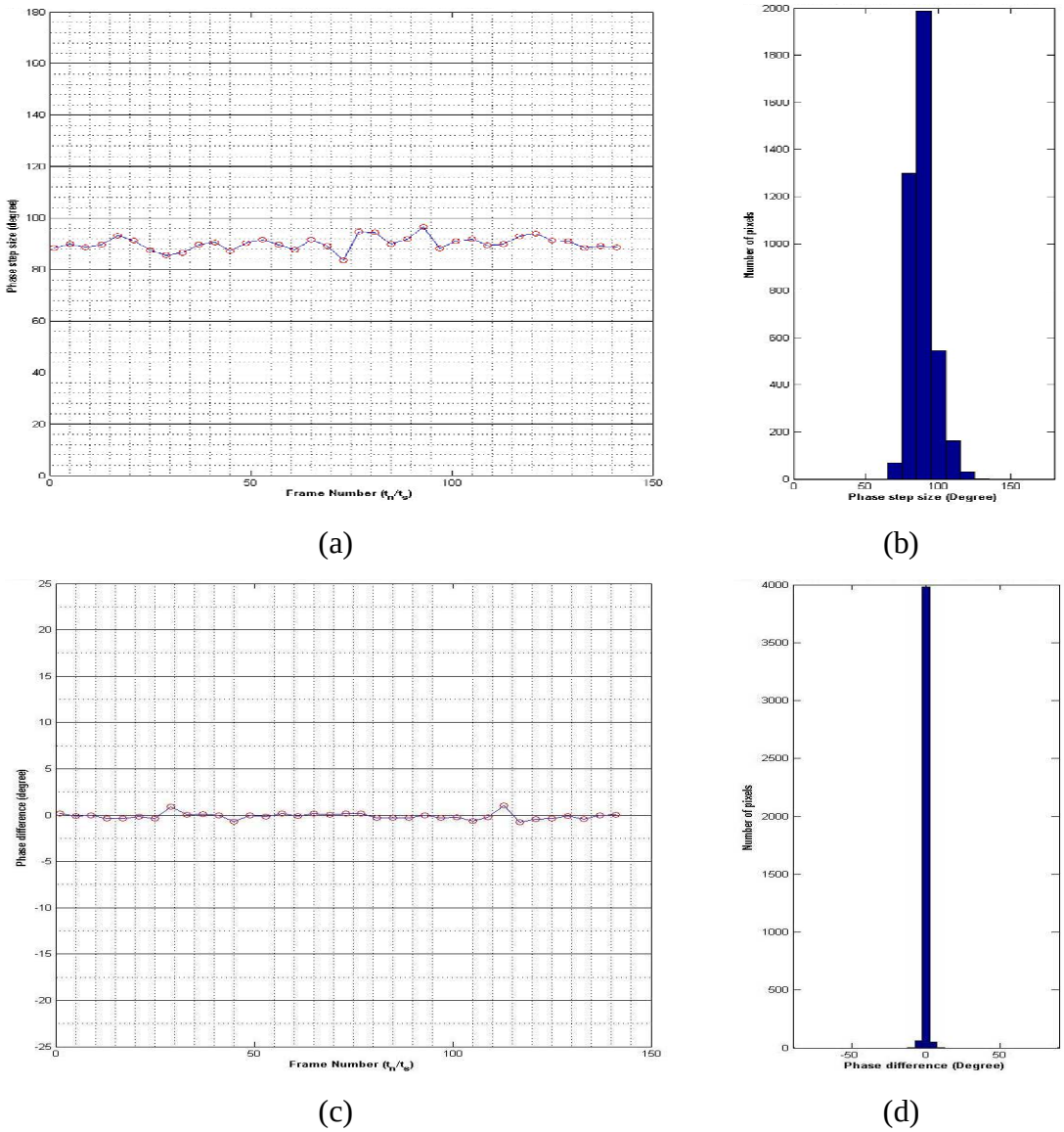

Figure 5.22 (a) Inter-frame phase-step size plotted against the frame number and (b) phase step size distribution for all frames recorded for a stationary object with a sampling rate of 7 kHz. (c) Inter-frame phase difference plotted against the frame number and (d) phase difference distribution, for the same image sequences as (a) and (b).

A comparison between Figure 5.21 (b) and Figure 5.22 (b) reveals that approximately 1500 pixels no longer have an average phase step size of 90°, whereas the other measurements show a good level of agreement. Moreover a low rate of repeatability was experienced in obtaining these results. Many studies, about the sources of error affecting the computation of the phase in phase-shifting interferometry, have been reported [87, 88, 89, 90, 91]. Here we don't aim to give a full characterization of these analyses, but we want determine approximately which factors might lead to an increase in the variance σ of the computed phase.

This can be approximated by:

$$\sigma_{phase} = k_1 \cdot \sigma_{Int.Noise} + k_2 \cdot \sigma_{Decorrelation} + k_3 \cdot \sigma_{Quantization} + k_4 \cdot \sigma_{Algorithm} \quad (5.11)$$

The most relevant contribution to σ_{phase} comes from the variance due to the intensity noise, thus enabling Equation 5.11 to be rearranged as:

$$\sigma_{phase} = \frac{\sigma_{Int.Noise}}{2 \cdot (MI_0)^2} \quad (5.12)$$

, where M is the modulation of fringes and I_0 is the background intensity.

For our system, a source of intensity noise affecting the phase computation is attributed to the unsatisfactory calibration of each pixel response, as discussed in Section 4. This leads to errors and hence instability in measurements performed at those pixels whose linearization and compensation is not successful.

The unwanted fluctuation of the reference beam, already discussed in Section 5.1, was also found to be responsible for introducing systematic errors in phase computation. The effect of having a fluctuation ranging in [4%, 10%] of the DC intensity of the reference beam, was modelled and the results are shown in Figure 5.23. An additional error introduced in phase computation (by using Equation 5.10) is plotted versus the velocity of the vibration. The model revealed that the fluctuation generates a phase change likely to a vibration undergoing on the test object. This means that the error introduced is lower when the object vibrates at higher velocities as the signal to noise ratio increases, and it is higher in a stationary situation.

On repeated tests, the results of the calibration revealed that for at least half of the pixels in the array an average phase step of 90° was applied; however a reliable distribution of the phase step size applied was not found due to the low repeatability of the measurements.

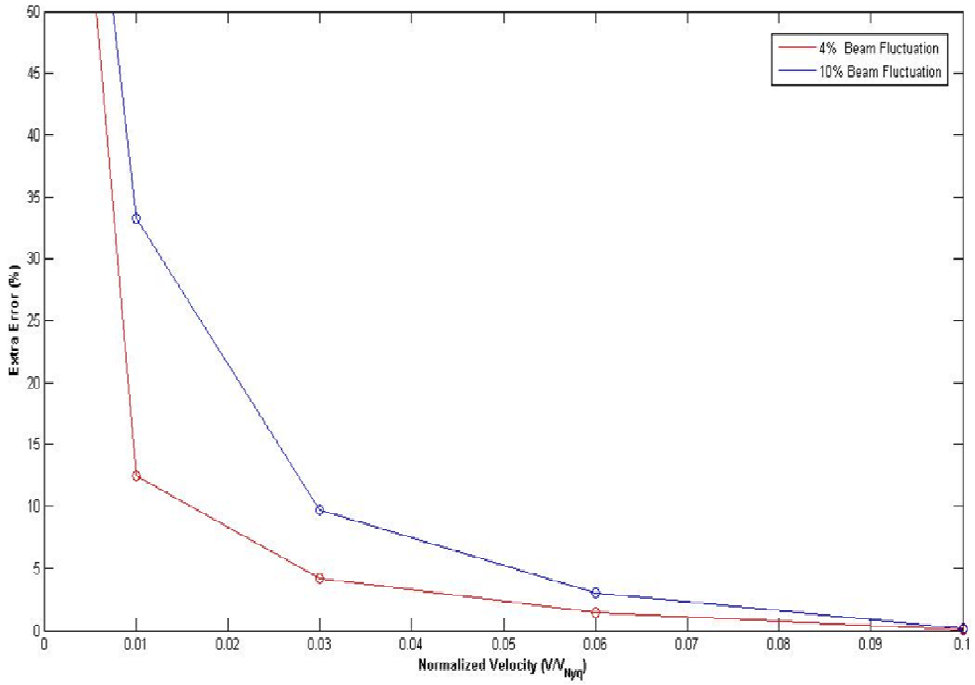

Fig. 5.23. Additional error introduced in velocity computation by the fluctuation of the reference beam. The minimum and the maximum amplitudes of the fluctuation are considered.

5.4.2 Vibration Measurement

A maximum sampling frequency $f_s = 7\ kHz$, with the camera locking – in $F_{Mod} = 1750\ Hz$, was not exceeded as discussed in the previous sections. This was imposed by:

- The optical setup is not able to provide enough light so as to characterize the full dynamic range of the camera at higher sampling frequencies.
- The camera readout strictly depends on the sampling frequency used and this causes a very low flexibility in the choice of N_{acq}.

The camera acquisition period is described by Equation 3.1, which is here reported for simplicity:

$$T_{acq} = T_{Mod} + readout = 4 * t_s + \frac{4 * X * Y}{F_c} + T_{ex} \qquad (5.13)$$

The readout takes the time necessary to acquire and sample all channels for all the pixels; when this time is not an integer multiple of T_{Mod}, an extra time T_{ex} is waited in order to match this requirement, thus extending the readout time. The actual sampling frequency $f_s = 7\ kHz$ enables a readout that is a multiple integer of T_{Mod}, thus eliminating T_{ex} and leading to $N_{acq} = 12$. If a small increase of the sampling frequency is considered, for example $f_s = 8\ kHz$, this would introduce the T_{ex} factor, thus increasing the readout and consequently N_{acq}. A sampling frequency $f_s = 40\ kHz$ would be used in order to match again the requirement that:

$$readout = N * T_{Mod} \tag{5.14}$$

However the amount of light, enables the characterization of the full dynamic range of the camera at a so high frame rate, is not available in our setup.
The limitations on the maximum frame rate and the lower value N_{acq} that can be used, automatically restrict the maximum velocity of vibration that can reliably be measured.
Rearranging Equation 3.10 leads to:

$$V \leq \frac{1}{N_{acq}^2 2\pi f t_s} \cdot V_{Nq} \tag{5.15}$$

The lower frequency of vibration enabling a time – averaged fringe resonance pattern, corresponds to 225 Hz. If a sampling frequency $f_s = 7\ kHz$ and $N_{acq} = 12$ are considered, the velocity limit is:

$$V \leq 0.03 \cdot V_{Nq} \tag{5.16}$$

On the base of these restrictions, the time – averaged pattern shown in Figure 5.7 was used to identify a ROI for time resolved measurements. Moreover a vibration amplitude, enabling a maximum velocity V=0.07 V_{Nq} in the area of the test object imaged on the MLC camera, was determined as shown in Figure 5.18 (b).
Simulations of the system characterized with these parameters were run and they are shown in Figure 5.24.

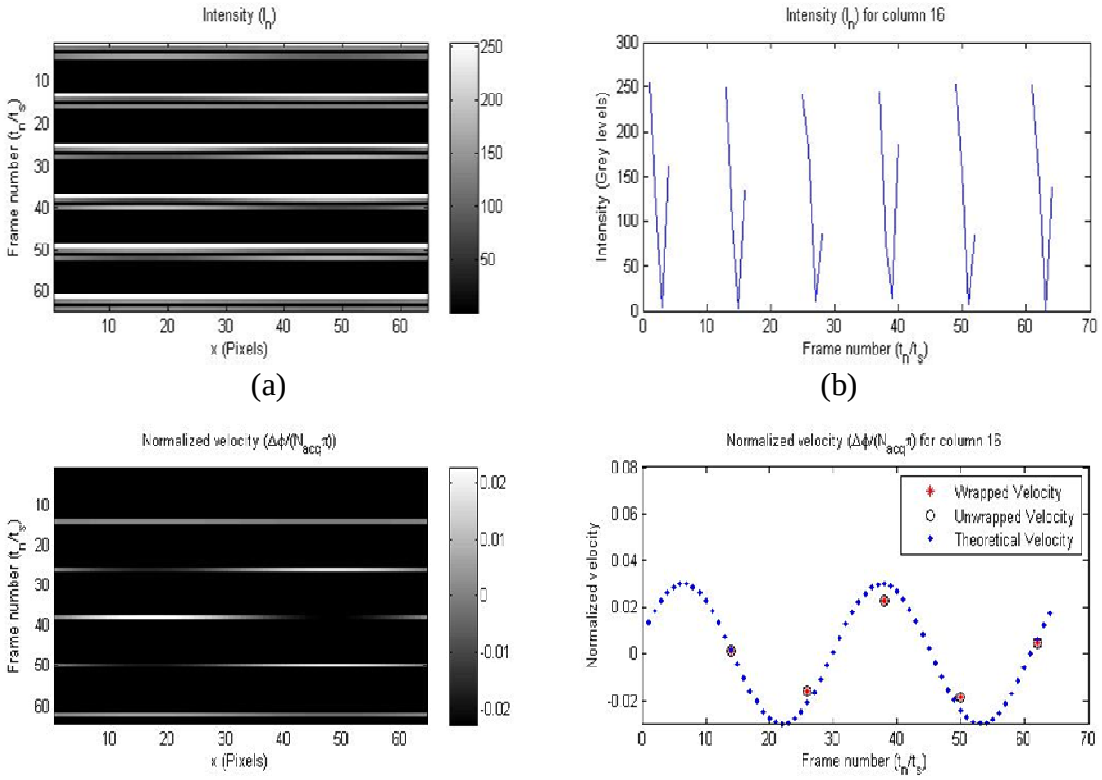

Fig. 5.24 (a) Simulation of a spatio-temporal speckle pattern showing the intensity variation for a horizontal ROI (64×1 pixels) recorded at 7 kHz and N_{acq}=12, for an object vibrating harmonically at 225 Hz and V=0.03V_{Nq} .(b) Intensity variation for column 16. (c) Normalized velocity $\Delta\Phi/(N_{acq}\pi)$ for the horizontal ROI and (d) Wrapped velocity, unwrapped velocity and theoretical velocity for column 16.

The velocity is correctly retrieved accordingly with Equation 5.15. Measurements of the normalized surface velocity undergoing in the test object were finally performed. Two pixels, enabling the computation of two different velocities, were chosen for the analysis of the results, as show in Figure 5.25.

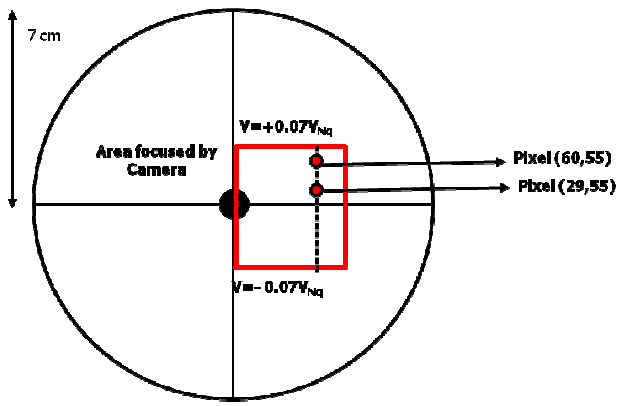

Fig. 5.25. Area focused by the camera. Column 55 of the pixels array is chosen as ROI in order to measure normalized surface velocities matching different cases of study.

Pixel (60,55) is close to the edge of the zero order fringe, where the normalized surface velocity was estimated to be V=0.07 $V_{Nq.}$ Pixel (29,55) is instead placed in the middle of the zero order fringe, where the normalized velocity was estimated to be lower and equal to V=0.01 V_{Nq}. Figure 5.26 shows a composite spatio-temporal phase-stepped speckle interferogram, where each row corresponds to a single frame of 64x1 pixels (array column 55) interrogated at 7 kHz and $N_{acq} = 12$. Composite spatio-temporal graphs of the wrapped phase and retrieved normalized velocity are also shown.

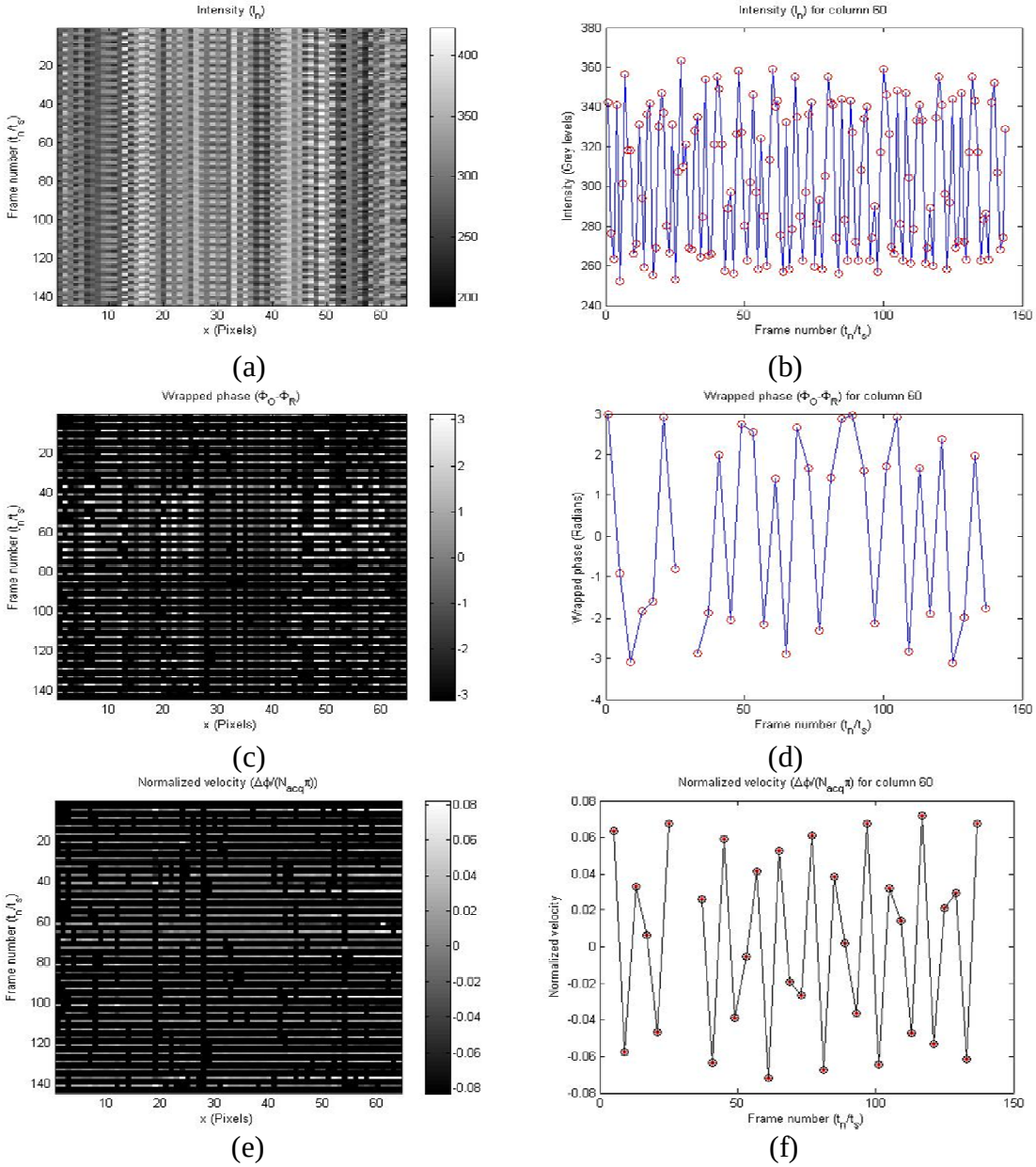

Fig. 5.26 (a) Simulation of a spatio-temporal speckle pattern showing the intensity variation for a horizontal ROI (64×1 pixels) recorded at 7 kHz and N_{acq}=12, for an object vibrating harmonically at 225 Hz. (b) Intensity variation for column 60. (c) Wrapped phase for the ROI and (d) wrapped phase for column 60. (e) Normalized velocity $\Delta\Phi/(N_{acq}\pi)$ for the horizontal ROI and (f) Unwrapped normalized velocity for column 60.

The number of frames considered enables approximately five periods of modulation to be shown. The maximum and minimum values of the normalized velocity, measured at pixel (55,60), match the expected value of $V=\pm 0.07V_{nq}$; the velocity profile is however very far from being periodic or harmonic. This is something expected as the velocity we tried to measure, is higher than the maximum velocity we could measure without unwrapping errors due to acceleration restrictions given by Equation 5.15. However the points characterized by lower vibration acceleration, i.e. the points where the maximum and minimum velocities of the vibration are achieved, could be correctly measured. All the other velocities retrieved are affected by expected unwrapping errors.

Figure 5.27 shows the intensity variation, wrapped phase and normalized surface velocity for column 29 of the composite graph shown in Figure 5.26. The maximum and minimum values of the normalized velocity, measured at pixel (55,29), match the estimated value of $V=\pm 0.01V_{nq}$. However the oscillation measured is not harmonic, though the velocity measured is within the limits imposed by Equation 5.16.

Indeed this result agreed with the analysis discussed in Section 5.4, where it was concluded that the test object vibrated harmonically only for velocities that were higher than approximately 0.03 V_{Nq}. Below this value, the vibration is no longer harmonic or it is lower than the vibrations caused by the environmental noise.

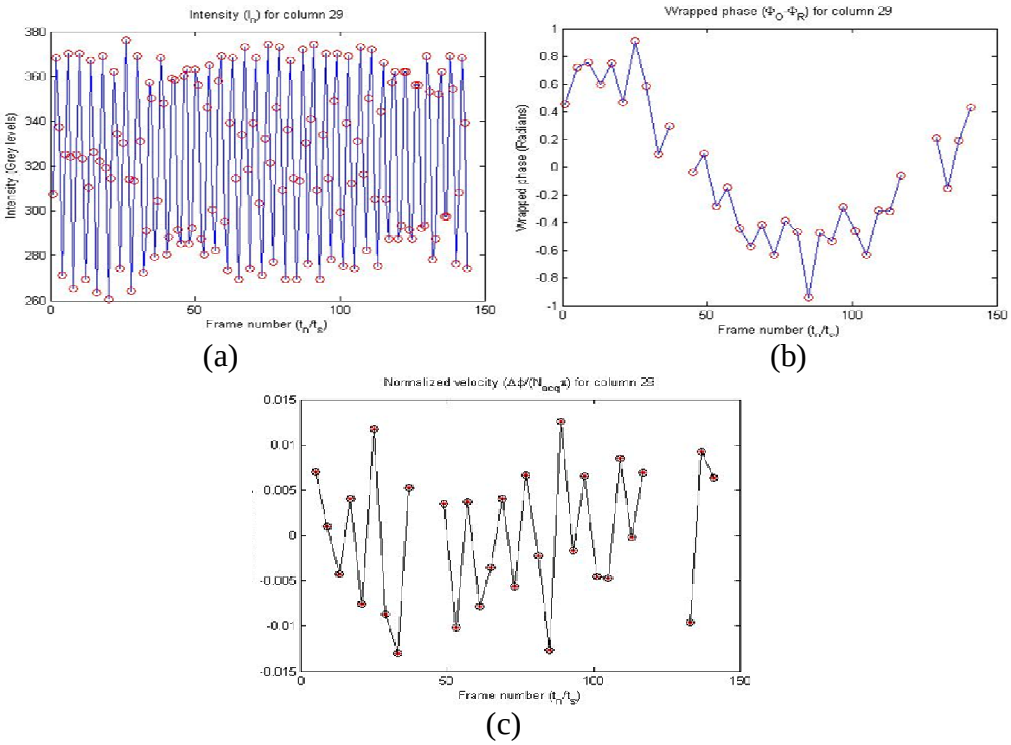

Fig. 5.27 (a) Intensity variation (b) Wrapped phase and (c) Normalized velocity $\Delta\Phi/(N_{acq}\pi)$ for column 29 of the composite graph of Figure 5.23 (a).

5.5 Discussion

An inter-frame phase stepped speckle pattern interferometry for time resolved measurement was developed. Initial experiments revealed an unwanted fluctuation of the reference beam when different voltages were applied to the phase modulator. This was attributed to a Fabry-Perot effect caused by a poor AR coating of the input/output of the phase modulator. Changes and improvements in the optical setup led to a reduction in the fluctuation in the range of [5%, 10%] of the DC reference beam intensity. The oscillation was found to be responsible for introducing additional systematic errors in the phase computation, when no vibration or low vibration were undergoing on the test object.

Time-averaged subtraction fringes, from which ROIs were identified for temporally resolved measurements, were successfully recorded. In order to validate the vibration properties of the object at low amplitudes of vibration, a single point laser vibrometer was accurately scanned across different sections of the test object. Results showed that the object did not vibrate harmonically when the amplitude of the vibration enabled a velocity $V<0.03\ V_{Nq}$.

A calibration of the size of the inter-frame phase steps applied was performed. Results showed that most of the pixels had an average phase step of 90° applied. The low repeatability of these measurements was attributed to the variance introduced by the intensity noise. An inefficient calibration of some pixels response and the systematic errors introduced by the reference beam oscillation in stationary conditions, were found to be the sources of this noise.

The highest frame rate of the camera was restricted to $f_s = 7\ kHz$ with $F_{Mod} = 1750\ Hz$. Higher frame rates would require an additional illumination, not available in our system, in order to characterize the full dynamic range of the camera. The limitations on the maximum frame rate and the lower value N_{acq} that can be used, automatically restricted the maximum velocity of vibration that could reliably be measured to $V<0.03\ V_{Nq}$. This requirement conflicted with the minimum velocity that corresponded to a harmonic vibration, i.e. $V>0.03\ V_{Nq}$. Measurement of surface velocities equal to $V=0.07\ V_{Nq}$ and $V=0.01\ V_{Nq}$ were tried. In both cases the maximum and minimum values of the velocity of the vibration were correctly retrieved. However unwrapping errors, caused by exceeding the limitations imposed by the acceleration, did not enable correct reconstruction of the velocity of the vibration when $V=0.07\ V_{Nq}$. Results obtained when

$V=0.01\ V_{Nq}$ cannot be evaluated reliably as no a priori knowledge of the nature of the vibration of the test object is possible.

Other attempts to measure the velocity in the range of $[0.01V_{Nq},\ 0.03\ V_{Nq}]$ were performed, but the lack of repeatability experienced did not enable any qualitative analysis of the results obtained. The variance in the computation of the phase, which is proportional to the undergoing vibration, was considered the main responsible for this lack of repeatability. The variance could depend on speckle decorrelation, intensity quantization noise, sensitivity of the algorithm used to this noise, and electronic noise. The noise introduced by the camera in light detection was found to be the most relevant factor affecting the vibration measurements. The approaches developed to compensate for the non linear response of the camera pixels, as well as the different gains of the channel responses, did not solve the issues in a satisfactory way all over the array.

Details about possible solutions and improvements of the actual experimental system are discussed in the next section.

Chapter Six

Conclusions and Future work

6.1 Conclusions

The MLC custom CMOS sensor was initially developed and optimized for parallel measurement of picosecond laser ultrasound. This kind of experiment is characterized by a large DC background with a very low contrast modulated component, typically from 10^{-4} to 10^{-6} of the DC level, caused by the picosecond acoustic pulse. For these reasons large capacitors, enabling a large dynamic range, were used in the designing the APS of this detector. This innovative design enables the required photon budget to be achieved, and hence noise performance, drastically increasing the well capacity from that of a standard diode alone. Furthermore an ADC with a bit depth of 12 bits, rather than the standard one of 8 bits, over the output range of the device was used to keep the quantization noise below the shot noise level.

It was reported[66] that the actual chip is not shot noise limited over an extend range of illumination conditions. In the particular case of low light conditions, the signal voltages are small and in these cases readout noise can dominate. The device is currently only shot noise limited when the wells are 50% full.

The calibration of the camera response that we developed is based on a full characterization over a range of illumination ranging from 0 mW to 500 mW. This means that half of the characterization, on which our approach was based is subject to an unlimited shot noise, which affects the quality of the compensation performed. The presence of noise justifies:

- The lack of repeatability in determining a unique camera response, that instead strongly depends on the frame rate used and the light available.
- The different response of the channels with respect to equal amount of light

We found that the different channel gain arises at low detected intensities, whereas it becomes a constant offset when higher intensities are detected (Figure 4.2). The different gain, yielding an inversion of the DC levels of light detected by each pixel (Figure 4.10), can be due to the noise affecting the device when low intensities are used.

The conclusion is that any correction aimed at the linearization and compensation of the channel responses at each pixel fails as long as the noise doesn't enable a deterministic and repeatable characterization of the camera response.

The first requirement to achieve this result is to use the device in experimental conditions where it is shot noise limited. This means that the illumination conditions must never drop down below a critical value, enabling the capacitors to be filled up with at least the 50% of their maximum capacity.

The experimental conditions reported by the authors fulfil this requirement as the modulated light that they successfully detect is on the order of 10^{-4} of the DC light. Furthermore the non linearity of the camera response doesn't affect their measurements, as the dynamic range that they use is very small with respect to the whole dynamic range of the camera. The inter-frame phase stepped system we are using is instead characterized by large intensity variations, and hence the need of linearity over an extended range for detected light.

6.2 Future work

Methods for calibration and correction of CMOS nonlinear responses were proposed[92, 93]; the approach consists of determining algorithms that transforms the camera response into the desired one. However these methods work when the camera response is deterministic, i.e. noise doesn't affect the characterization of the response, or when modelling the noise is possible thanks to a priori knowledge about the electronics of the device. Since we don't know which electronic factors generate the noise we cannot model it. A further approach could be to design an algorithm which is able to divide each single pixel response in smaller subsets, determine the best fit for each of them and calculate the appropriate correction for each subset of each pixel. However the long computational time required to cycle this algorithm over 4096 pixels, and the high complexity of

designing a routine which automatically determines how to define proper subsets in each pixel response, suggest a different approach.
Here we describe a solution based on significant changes in the optical setup and yielding a reduction of the noise affecting the camera detection of low intensities of light.

1) We can illuminate the array with an extra source of DC light. This would enable the achievement of the photon budget that is required to have a shot noise limitation. Figure 6.1 shows a fibre optic source that is suitable from Heriot – Watt University's renewable energy group. It is provided with a lamp input power of 100 W and a variable gain. The coupling of the output light with an optic fibre is available. The interference signal that characterizes our speckle pattern interferometer, would be added to this extra amount of DC light. This enables the possibility to only use the dynamic range of the camera that is noise limited. Possible interference between the DC light and green light of our laser were considered. Interference would be generated only if a constant relationship between the phases of the two beams exists; moreover the power of the white light at a wavelength equal to 532 nm is low as shown in figure 6.1 (b).

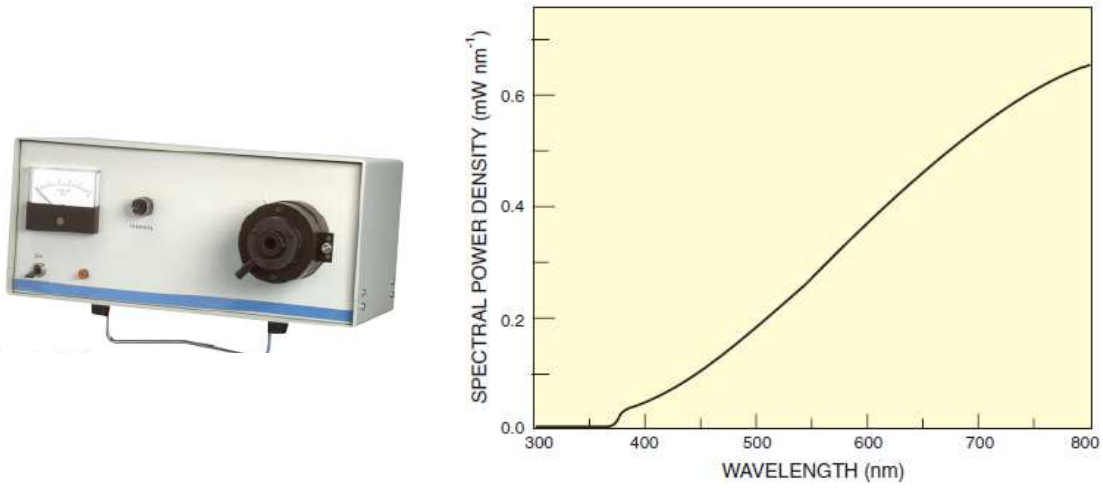

(a) (b)

Fig. 6.1 (a) 77501 Radiometric fibre optic source (b) Spectral irradiance of the device.

2) The exact amount of DC light corresponding to the 50% of the capacity of the wells needs to be calculated. We cannot assume that a linear relationship, between

the photons contained in the capacitors and the light detected, exists. The extra DC light needed can be found with a trial and error approach. We can illuminate the array with a source of sinusoidal amplitude modulated light; this would ideally enable an intensity variation of at least 100 intensity levels, so to as approximately match the mean intensity variation in our experimental measurements. If the light detected by the camera is noisy or distorted, it means that we are still using the part of the dynamic range of the camera that is affected by shot noise. We could repeat this procedure and increase the variable gain of the extra DC light, until the light detection is not affected by noise.

3) In the hypothesis that the extra DC light provided doesn't cover at least half of the dynamic range of the camera, an additional contribution might be obtained by the reference beam intensity. The new optical setup, described in section 5.1, enables an easy change of the ratio between the reference and the object beam. On the other hand this would reduce the amplitude modulation of the two interfering beams at the sensor image plane, hence we need to take into consideration that the extra contribution given by the reference beam is limited.

4) An analysis of the efficiency of the camera detection at different wavelengths was not reported in any paper written by the developers. The camera was used in an optical setup including a laser beam with a wavelength of 800nm, and a power of 400 mW coupled in a supercontinum Newport SCG-800 Photonic Crystal fibre. The power of the beam at the camera image plane was approximately of 120 mW. We might use these values as reference and start independent measurements of the detection efficiency by illuminating the camera array with beams of equal power but different wavelength. The green laser and the source of white light above mentioned would be used for this analysis.

5) Once the dynamic range of the camera, that is not affected by noise, is determined, we must find which pixels are saturated when the modulated light of interest is applied over the extra DC light. This analysis has to be performed pixel by pixel since the dynamic range of each pixel can strongly differ from the others. We can determine a reference response, and then calculate the correlation of each pixel response with the reference. We can fix a threshold of correlation in order to

eliminate those pixels which are saturated or having a response completely different from the desired one.

6) The calibration of the camera response can now be performed within the limits of the new dynamic range. Figure 4.4 shows that the camera response is approximately linear in the above mentioned range of interest. Furthermore the channel responses are characterized by DC offset rather than a different gain; this would enable an easier compensation. A 2D map showing the performance of the correction pixel by pixel might be developed in order to determine a smaller subset of pixels suitable for further measurements.

7) The previous steps would yield to have a set of pixels, with a linear response, uniform channel gains and not affected by electronic noise. The additional problem to be solved, is the restrictions imposed on the maximum velocity of vibration that we can measure with the actual system. The Nyquist limit imposes a maximum measurable velocity $V<0.03\ V_{Nq}$, whereas the vibration undergoing on the test object is harmonic only when $V>0.03\ V_{Nq}$. IN order to overcome this issue we can:

    a. Increase the sampling rate of the camera up to 40 kHz, thus enabling a smaller gap $N_{acq}=8$ to be set and dramatically increasing the measurable velocity up to $V<0.44\ V_{Nq}$. The extra amount of light might enable such a high frame rate to be used, however the authors never experimentally used the camera in these conditions. They used a maximum sampling frequency $f_s = 6.8\,kHz$ and $F_{Mod} = 1700\,Hz$.
    b. If the increase of the frame rate is not possible because of the high photons budget required, we can consider the possibility of reducing the dimensions of the test object, which currently has a diameter equal to 14 cm. A smaller diameter would enable the object to harmonically vibrate for frequencies lower than 225 Hz or for lower amplitude of vibrations; this would yield to an increase of the maximum velocity measurable. If we assume a frequency of vibration equal to 50 Hz, a sampling frequency $f_s = 6.8\,kHz$ and $N_{acq}=12$, the restriction imposed by the Nyquist limit becomes $V<0.15\ V_{Nq}$.

c. A further improvement would be using the camera as a linear detector rather than in full field mode. This choice would give us a larger flexibility in setting smaller values of N_{acq}, and hence increasing the range of measurable velocities.

References

[1] S. Equis. “Phase extraction of non-stationary signal produced in dynamic interferometer involving speckle waves”. PhD thesis N° 4514, Ecole Polytechnique Federale de Lausanne, 2009.

[2] L. Scalise and N. Paone. “Laser Doppler vibrometry based on self-mixing effect”. Optics and Lasers in Engineering, Vol. 38, pp. 173-184, 2002.

[3] L. Scalise, G. Stavrakakis, and A. Pouliezos. “Fault detection for quality control of household appliances by non-invasive laser Doppler technique and likelihood classifier”. Measurement, Vol. 25, pp. 237-247, 2000.

[4] R. A Martínez-Celorio, B. Barrientos, F. J. Sanchez-Marín, L. M. López, J. A. Rayas. “Out-of-plane displacement measurement by electronic speckle pattern interferometry in presence of large in-plane displacement”. Optics Comunications, Vol. 208, pp. 17-24, 2002.

[5] J. Y. Lee, M. P. Lu, K. Y. Lin, and S. H. Huang. “Measurement of in-plane displacement by wavelength-modulated heterodyne speckle interferometry”. Applied Optics, Vol. 51, pp. 1095-1100, 2012.

[6] D. Gabor. “A new microscopic principle”. Nature, Vol. 161, pp. 777-778, 1948.

[7] K. A. Stetson and R. L. Powell. “Interferometric hologram evaluation and real-time vibration analysis of diffuse objects”. Journal of the Optical Society of America, Vol. 55, pp. 1694-1695, 1965.

[8] J. A. Leendertz, J. N. Butters. “Speckle pattern and holographic techniques in engineering metrology”. Optical Laser Technology, Vol. 3, pp. 26-30,1971.

[9] U. Schnars and W. Juptner. “Direct recording of holograms by a CCD-target and numerical reconstruction”. Appied Optics, Vol. 33, pp. 179-181, 1994.

[10] J. D. Valera, D. Harvey, and J. D. C. Jones. “Fibre optic speckle pattern interformetry: path length stabilised automatic phase stepping”. IEE Conference Publication, Vol. 342, pp. 180-184, 1991.

[11] K. Creath and J. C. Wyant. Cap. 16 – Moire' and Fringe projection techniques. Optical Shop testing, Second Edition, Edited by Daniel Malacara. ISBN 0-471-52232-5 © 1992, John Wiley & Sons, inc.

[12] S. Zhang. “Recent progress on real time 3D shape measurement using digital fringe projection techniques“. Optics and Lasers in Engineering, Vol. 48, pp. 149-158, 2010.

[13] C. Quan, W. Chen. “Phase retrieval techniques in fringe – projection profilometry”. Optics and Lasers in Engineering, Vol. 48, pp. 235-243, 2010.

[14] A. J. Moore, R. McBride, J. S. Barton, and J. D. C. Jones. “Closed loop phase stepping in a calibrated fiber-optic fringe projector for shape measurement. Applied Optics, Vol. 41, pp. 3348-3354, 2002.

[15] C. Joenathan, B. Pfister, and H. J. Tiziani. “Contouring by electronic speckle pattern interferometry employing dual beam illumination”. Applied Optics, Vol. 29, pp. 1905-1911, 1990.

[16] C. A. Bennet. “Principles of physical optics”. Published by Wiley, 2008.

[17] F. A. Jenkins and H. E. White. “Fundamentals of Optics”. New York, EUA: McGraw – Hill, 1976.

[18] E. Hecth and A. Zajac. “Optics”. Published by Addison Wesley, 1974.

[19] J. N. Butters, J. A. Leendertz. “Holographic and video techniques applied to engineering measurement”. Journal of Measurement and Control, Vol. l4, pp. 349-354, 1971.

[20] A. J. Moore, J. D. C. Jones, J. D. R. Valera. “Dynamic measurements in digital speckle interferometry and related techniques”. Ed. Rastogi P.K, Wiley, Chap. 4, pp. 225–288, 2001.

[21] O. J. Lokberg and K. Hogmoen. “Use of modulated reference wave in electronic speckle pattern interferometry”. Journal of Physics E: Scientific Instruments, Vol.9, pp. 847, 1976.

[22] O. J. Lokberg and K. Hogmoen. “Vibration phase mapping using electronic speckle pattern interferometry”. Applied Optics, Vol.15, pp. 2701, 1976.

[23] S. Nakadate, T. Yatagai, H. Saito. “Electronic speckle pattern interferometry using digital image processing techniques”. Applied Optics, Vol. 19, pp. 1879 1980.

[24] T. J. Cookson, J. N. Butters, H. C. Pollard. “Pulsed lasers in electronic speckle pattern interferometry”. Optics & Laser Technology, Vol. 10, pp. 119-124, 1978.

[25] A. J. Moore, C. Pérez-López. “Low-frequency harmonic vibration analysis with double-pulsed addition electronic speckle pattern interferometry”. Optical Engineering, Vol. 35, pp. 2641-2650, 1996.

[26] F. M. Santoyo, A. J. Moore, J. R. Tyrer, N. A. Ochoa. “Noise reduction in twin-pulsed addition electronic speckle pattern interferometry fringe patterns”. Optical Engineering, Vol. 33, pp. 1712-1716, 1994.

[27] A. Davila, D. Kerr, G. H. Kaufmann. “Digital processing of electronic speckle pattern interferometry addition fringes”. Applied Optics, Vol. 33, pp. 5964-5969, 1994.

[28] A. J. Moore, C. Perez-Lopez. “Fringe visibility enhancement and phase calculation in double pulsed addition ESPI”. Journal of Modern Optics, Vol. 43, pp. 1829-1844, 1996.

[29] R. Spooren. “Double pulsed subtraction TV holography”. Optical Engineering, Vol. 31, pp. 1000-1007 , 1992.

[30] A. Fernandez, A. J. Moore, C. Perez-Lopez, A. F. Doval, and J. Blanco-Garcia. “Study of transient deformations with pulsed TV holography: application to crack detection”. Applied Optics, Vol. 36, pp. 2058-2065, 1997.

[31] M. C. Shellabear, J. R. Tyrer. “Application of ESPI to three dimensional vibration measurement”. Optical & Laser Engineering, Vol. 15, pp. 43-56, 1991.

[32] A. J. Moore, D. P. Hand, J. S. Barton, and J. D. C. Jones. “Transient deformation measurement with electronic speckle pattern interferometry and a high speed camera”. Applied Optics, Vol. 38, pp. 1159-1162, 1999.

[33] J. M. Kilpatrick, A. J. Moore, J. S. Barton and J. D. C. Jones, M. Reeves and C. Buckberry. “Measurement of complex surface deformation by high-speed dynamic phase stepped digital speckle pattern interferometry”. Optics Letters, Vol. 25, pp. 1068-1070, 2000.

[34] J. E. Greivenkamp. “Sub-Nyquist interferometry”. Applied Optics, Vol. 26, pp. 5245–5258, 1987.

[35] T. Wu. “Extending the measurement range of high-speed speckle pattern interferometry”. PhD thesis, Heriot Watt University, 2009.

[36] T. Wu, J. D. C. Jones and A. J. Moore. “High speed phase stepped digital speckle pattern interferometry using a complementary metal oxide semiconductor camera”. Applied Optics, Vol. 45, pp. 5845-5855, 2006.

[37] C. Joenathan, B. Franze, P. Haible, H. J. Tiziani. “Speckle interferometry with temporal phase evaluation for measuring large-object deformation”. Applied Optics, Vol. 37, pp. 2608-2614, 1998.

[38] J. M. Huntley, G. H. Kaufmann, D. Kerr. “Phase shifted dynamic speckle pattern interferometry at 1 kHz”. Applied Optics, Vol. 38, pp. 6556-6563, 1999.

[39] X. Colonna De Lega and P. Jacquot.”Deformation measurement with object-induced dynamic phase shifting”. Applied Optics, Vol. 35, pp. 5115-5121, 1996.

[40] X. Colonna De Lega. “Processing of non-stationary interference patterns: adapted phase shifting algorithms and wavelet analysis. Application to dynamic deformation measurements by holography and speckle interferometry”. PhD thesis, Ecole Polytechnique Federale de Lausanne, 1997.

[41] A. Svanbro, J. M. Huntley and A. Davila. “Optimal re-referencing rate for in-plane dynamic speckle interferometry”. Applied Optics, Vol. 42, pp. 251-258, 2003.

[42] M. Lehmann. “Decorrelation-induced phase errors in phase-shifting speckle interferometry”. Applied Optics, Vol. 36, pp. 3657-3667, 1997.

[43] M. Lehmann. “Phase shifting interferometry with unresolved speckles: A theoretical investigation”. Optics Comunications, Vol. 128, pp. 325-340, 1996.

[44] P. D. Ruiz, J. M. Huntley, Y. Shen, C. R. Coggrave, and G. H. Kaufmann. “Effects of random vibration in high-speed phase-shifting speckle pattern interferometry”. Applied Optics, Vol. 41, pp. 3941-3949, 2002.

[45] J. M. Huntley, J. R. Buckland, and S. R. Turner. “Unwrapping noisy phase maps by use of a minimum-cost-matching algorithm”. Applied Optics, Vol. 34, pp. 5100-5108, 1995.

[46] J. M. Huntley. ”Three dimensional noise immune phase unwrapping algorithm”. Applied Optics, Vol. 40, pp. 3901–3908, 2001.

[47] A. J. P. Van Haasteren and H. J. Frankena. “Real time displacement measurement using a multicamera phase stepping speckle interferometer”. Applied Optics, Vol. 33, pp. 4137-4142, 1994.

[48] T. D. Upton and D. W. Watt. “Optical and electronic design of a calibrated multichannel electronic interferometer for quantitative flow visualization”. Applied Optics, Vol. 34, pp. 5602-5610, 1995.

[49] J. Millerd, N. Brock, J. Hayes, M. North-Morris, M. Novak and J. Wyant. “Analysis of a micropolarizer array-based simultaneous phase-shifting interferometer”. Applied Optics, Vol. 44, pp. 6861-6868, 2005.

[50] B. T. Kimbrough. “Pixelated mask spatial carrier phase shifting interferometry algorithms and associated errors”. Applied Optics, Vol. 45, pp. 4554-4562, 2006.

[51] J. Millerd, N. Brock, J. Hayes, M. North-Morris, M. Novak and J. Wyant. “Pixelated phase-mask dynamic interferometer”. Proc. SPIE, Vol. 5531, pp. 304-314, 2004.

[52] M. Servin, A. Davila, J. A. Quiroga. “Extended range temporal electronic speckle pattern interferometry”. Applied Optics, Vol. 41, pp. 4541–4547, 2002.

[53] T. Kreis. “Digital holographic interference-phase measurements using the Fourier transform method”. Journal of the Optical Society of America , Vol. 3, 1986.

[54] A. J. Moore and F. Mendoza-Santoyo. “Phase demodulation in the space domain without a fringe carrier”. Optics and Lasers in Engineering, Vol. 23, pp. 319-330, 1995.

[55] P. De Groot and L. Deck. “Three dimensional imaging by sub-Nyquist sampling of white light interferograms”. Optics Letters, Vol. 18, pp. 1462-1464, 1993.

[56] L. Huang, Q. Kemao, B. Pan, A. K. Asundi. “Comparison of Fourier transform, windowed Fourier transform, and wavelet transform methods for phase extraction from a single fringe pattern in fringe projection”. Optics and Lasers in Engineering, Vol. 48, pp. 141–148, 2010.

[57] P. D. Ruiz, J. Huntley, G. H. Kaufmann. “Adaptive phase shifting algorithm for temporal phase evaluation”. Journal of the Optical Society of America, Vol. 20, pp. pp. 325-332, 2003.

[58] Y. Fu, C. J. Tay, C. Quan, L. J. Chen. “Temporal wavelet analysis for deformation and velocity measurement in speckle interferometry”. Optical Engineering, Vol. 43, pp. 2780-2787, 2004.

[59] Y. Fu, C. J. Tay, C. Quan, and H. Miao. “Wavelet analysis of speckle patterns with a temporal carrier”. Applied Optics, Vol. 44, pp. 959-965, 2005.

[60] S. Equis. “Phase extraction of non-stationary signal produced in dynamic interferometer involving speckle waves”. PhD thesis N° 4514, Ecole Polytechnique Federale de Lausanne, 2009.

[61] S. Equis and P. Jacquot. “The empirical mode decomposition: a must have tool in speckle interferometry? ”. Optic Express, Vol. 17, pp. 6114623, 2009.

[62] S. Equis and P. Jacquot. “Phase extraction in Dynamic speckle interferometry with Empirical Mode Decomposition and Hilbert transform”. Strain, Vol. 46, pp. 550-558, 2010

[63] S. Bourquin, V. Monterosso, P. Seitz, R. P. Salathe'. "Video-rate optical low coherence reflectometry based on a linear smart detector array". Optics Letters, Vol. 25, pp. 102-104, 2000.

[64] S. Bourquin, P. Seitz, R. P. Salathe'. "Two-dimensional smart detector array for interferometric applications". Electronics Letters, Vol. 37, pp. 975-976, 2001.

[65] A. Kimachi, S. Ando, T. Kurihara, M. Takamoto. "A novel range finding system using correlation image sensor". The Transactions of the Institute of Electrical Engineers of Japan, Vol. 121-E, pp. 367-375, 2001.

[66] A. Kimachi, S. Ando. "Correlation image sensor: Two-dimensional Matched Detection of amplitude-Modulated Light". IEEE transactions on electron devices, Vol. 50, pp. 173-183, 2003.

[67] A. Kimachi, S. Ando, T. Imaizumi, A. Kato. "Spectral Matching Imager using correlation image sensor". The Transactions of the Institute of Electrical Engineers of Japan, Vol. 122-E, pp. 200-207, 2002.

[68] A. Kimachi. "Real-time heterodyne imaging interferometry: focal plane amplitude and phase demodulation using a three phase correlation image sensor". Applied Optics, Vol. 46, pp. 87-94, 2007.

[69] A. Kimachi and S. Ando. "Real-time Phase-Stamp range finder using correlation image sensor". IEEE Sensors Journal, Vol. 9, pp. 1784 – 1792, 2009.

[70] P. R. Dmochowski, B. R. Haye-Gill, M. Clark, J. A. Crowe, M. G. Somekh, and S.P. Morgan. "A lock-in pixel for a Cmos Modulated light camera". Solid-State Circuits, IEEE Journal, 2003.

[71] M. C. Pitter, J. Y. L. Goh, B. R. Hayes-Gill, M. Clark and S. P. Morgan. "Phase sensitive CMOS photo-circuit array for modulated thermoreflectance measurements". Electronics Letters, Vol. 39, pp. 1339 – 1340, 2003.

[72] M. C. Pitter, R. A. Light, B. R. Hayes-Gill, M. Clark. "Dual-Phase synchronous light detection with a 64x64 CMOS modulated light camera". Electronics Letters, Vol. 40, pp. 1404-1406, 2004.

[73] I. R. Hooper, J. R. Sambles, M. C. Pitter, M. G. Somekh. "Phase sensitive array detection with polarisation modulated differential sensing". Sensors and Actuators, Vol. 119, 651-655, 2006.

[74] N. S. Johnston, C. Stewart, R. A. Light, B. R. Hayes-Gill, M. G. Somekh, S. P. Morgan, J. R. Sambles and M. C. Pitter. "Quad-phase synchronous light detection

with 64x64 CMOS modulated light camera". Electronic letters, Vol. 45, pp. 1090-1091, 2009.

[75] R. A. Light. "Design and Implementation of an integrating modulated light camera". PhD thesis, Nottingham University, 2008.

[76] R. Smith, M. Somekh, S. Sharples, M. Pitter, R. Light, N. Johnston. "Parallel detection in picosecondultrasonic with both commercial and custom array detection". 1st International Symposium on laser ultrasonics: Science, Technology and Applications. Montreal, Canada, 2008.

[77] R. Smith, M. Somekh, S. Sharples, M. Pitter, I. Harrison and C. Rossignol. "Parallel detection of low modulation depth signals: application to picoseconds ultrasonics". Measurement Science and Technology, Vol. 19, pp. 1-8, 2008.

[78] R. Smith, M. Somekh, S. Sharples, M. Pitter, R. Light, N. Johnston. "Multichannel, time resolved picoseconds laser ultrasound imaging and spectroscopy with custom complementary metal-oxide-semiconductor detector". Review of Scientific Instruments, Vol. 81, 2010.

[79] R. Smith, M. Somekh, S. Sharples, M. Pitter, R. Light, N.Johnston. "Highly parallel CMOS lock – in optical sensor array for hyperspectral recording in scanned imaging systems". Proceedings SPIE, Vol. 7570, 2010.

[80] S. Morgan and B. Hayes-Gill. "Custom made camera for blood flow imaging". Proceedings SPIE, Vol. 7891, 2011.

[81] S. Morgan and B. Hayes-Gill, J. A. Crowe, D. He, C. Kongsavatsak. "Complementary metal oxide semiconductor imaging array with laser Doppler blood flow processing". Optical Engineering, Vol. 47, 2008.

[82] J. Sathian and E. Jaatinen. "Intensity dependent residual amplitude modulation in electro-optic phase modulators". Applied Optics, Vol. 51, pp. 3684-3691, 2012,

[83] M. Lehmann. "Measurement optimization in speckle interferometry: the influence of the imaging aperture". Proceedings SPIE Vol. 2782, pp. 408-419, 1996.

[84] T. Yoshimura, M. Zhou, K. Yamahai, Z. Liyan. "Optimum determination of speckle size to be used in electronic speckle pattern interferometry". Applied Optics, Vol.34, pp. 87-91, 1995.

[85] M. Taked, H. Ina, and S. Kobayashi. "Fourier- transform method of fringe-pattern analysis for computer based topography and interferometry". Journal of the Optical Society of America, Vol. 72, pp. 156-160, 1982.

[86] P. Carré. “Installation et utilisation du comparateur photoélectrique et interférential du Bureau International des Poids et Mesures”. Metrologia, Vol. 2, pp. 13-23, 1966.

[87] J. Schwider, R. Burow, K. E. Elssner, J. Grzanna, R. Spolaczyk, and K. Merkel. “Digital wave-front measuring interferometry: some systematic error sources”. Applied Optics, Vol. 22, pp. 3421-3432, 1983.

[88] C. P. Brophy. “Effect of intensity error correlation on the computed phase of phase-shifting interferometry”. Journal of the Optical Society of America, Vol. 7, pp. 537-541, 1990.

[89] K. Patorski and A. Styk. “Interferogram intensity modulation calculations using temporal phase shifting: error analysis”. Optical Engineering, Vol. 45, 2006.

[90] Y. Surrel. “Additive noise effect in digital phase detection”. Applied Optics, Vol. 36, pp. 271–276, 1997.

[91] J. M. Huntley. “Random phase measurement errors in Digital Speckle Pattern Interferometry”. Optics and Lasers in Engineering Vol. 26, pp. 131-150, 1997.

[92] Y. Shang, Y. Guan, W. Zhang, X. Liu, S. Zhang and Y. Zhang. “A high dynamic range complementary metal*oxide-semiconductor (CMOS) camera using multi-slope response and a image reconstruction algorithm”. Measuring Science and Technology, Vol. 20, 2009.

[93] D. Joseph and S. Collins. “Modelling, calibration, and correction of Nonlinear Illumination-dependent fixed pattern noise in logarithmic CMOS Image sensor”. IEEE transactions of instrumentation and measurement, Vol. 51, pp. 996 – 1001, 2002.